12-14-2015

Optimized Spectral Processing of Infrared Diffuse Reflection Spectra for the Detection of Blood on Fabric

Stephanie Ann DeJong
University of South Carolina - Columbia

Optimized Spectral Processing of Infrared Diffuse Reflection Spectra for the Detection of Blood on Fabric

by

Stephanie Ann DeJong

Bachelor of Arts
Trinity Christian College, 2011

Submitted in Partial Fulfillment of the Requirements

For the Degree of Doctor of Philosophy in

Chemistry

College of Arts and Sciences

University of South Carolina

2015

Accepted by:

Michael L. Myrick, Major Professor

S. Michael Angel, Committee Chair

Stephen L. Morgan, Committee Member

John W. Weidner, Committee Member

Lacy Ford, Senior Vice Provost and Dean of Graduate Studies

ACKNOWLEDGEMENTS

There are so many people who have helped shaped my life to this point and enabled me to be successful in my pursuit of this degree. First, I would like to thank my committee members Dr. Angel, Dr. Weidner, and Dr. Morgan, whose advice and guidance over the past few years has been greatly appreciated. I particularly thank Dr. Morgan, who continually encouraged me to carefully consider both my words and my data, because I should be ready to defend either at all times. I would also like to thank Dr. Lou Sytsma, my undergraduate research advisor, without whose encouragement I might not have decided to attend graduate school.

I am also much obliged to my fellow Myrick lab members: Dr. Joe Swanstrom, for introducing me to the lab and grad school; Elizabeth Abernathy, for always being willing to help; Shawna Tazik, who has been with me at every step along this journey; Brianna Cassidy and Zhenyu Lu, honorary Myrick lab members; and to Cameron Rekully, Ray Belliveau, and Stefan Faulkner for all their engaging conversations.

I could not have accomplished any of what I've done without the continuing love and support of my parents, Charles and Monique DeJong. They have always been my safety net, and have always been there to remind me that I don't need a safety net because I can succeed at whatever I set my mind to.

Finally, I would like to offer my gratitude to my advisor Dr. Michael Myrick. I may not have known I would be working with him when I arrived at U.S.C., but I now sincerely feel that my graduate experience would not have been nearly as fulfilling with any other advisor. There are few people I respect as much both personally and professionally. Dr. Myrick has seen me at some of my best and some of my worst moments, but his kindness rarely flagged; his response was almost always: “Let’s get coffee.” So thank you for all the coffee, tea, support, and advice. My life has been forever changed by your influence.

ABSTRACT

The detection of bodily fluids such as blood on interfering backgrounds is important to the forensic community. Luminol, which participates in a chemiluminescent reaction with the heme groups of blood, is one of the most commonly used presumptive tests. Luminol has a few drawbacks, including the requirement of use in a dark environment and potential to degrade the amount of recoverable DNA in blood stains. A potential complementary method is infrared (IR) spectroscopy. These two methods are compared in this work.

Infrared diffuse reflection (DR) spectroscopy works well to measure the IR spectrum of samples that are highly absorbing or scattering, such as fabric. In the IR DR spectrum of blood on fabric, the contribution of analyte signal to the total signal is weak, and many of the characteristic amide absorbance bands of blood proteins overlap with the spectral features of fabrics. Derivative transformations are commonly applied to resolve overlapping spectral peaks. These transformations are typically implemented as Savitzky-Golay (SG) derivatives. The performance of optimized higher-order gap derivatives (GDs) and SG derivatives are compared here as preprocessing methods for partial least-squares regression (PLSR), a multivariate calibration technique. Optimized GD processing is found to behave similarly to a matched filter to highlight spectral features of the analyte relative to an interfering background.

Derivatives can result in complicated spectra and regression vectors (RV)

from the PLSR calibration. To enable better interpretation of the RVs, it is useful to examine the RVs in the original spectral space, which is more familiar to spectroscopists. To that end, we offer a method of calculating higher-order GDs that allows the resulting GD and RVs to be exactly integrated to spectral space.

Infrared detection limits (DLs) for blood on four fabric types (acrylic, cotton, nylon, and polyester) were estimated using optimized GD processing and PLSR. The best IR DLs for blood on fabric were found in the mid-IR spectral region. The DLs for acrylic, cotton, and polyester fabrics were blood diluted by factors of 2300, 610, and 900, respectively. Due to the similarity between the IR spectra of blood solids and nylon, no satisfactory IR DLs were determined for the calibration of blood on nylon. These DLs are on the order of the most commonly reported DLs (1000x dilute) for blood on fabric using the standard luminol method. An approach to further improve the DL by accounting for known sources of extraneous variance in the spectra is briefly presented.

TABLE OF CONTENTS

LIST OF TABLES

LIST OF FIGURES

CHAPTER 1

INTRODUCTION

1.1. INFRARED SPECTROSCOPY AND FORENSIC SCIENCE

Crime scenes are often disordered environments, making it difficult to identify samples that may be of forensic importance. Because biological evidence such as semen, sweat, and blood may be found on any number of surfaces at a variety of concentrations, it is important for investigators to have effective tools to determine which samples might warrant further testing. These tools must be selective enough to not waste resources on superfluous samples, sensitive enough to detect small or dilute stains, and harmless enough that neither the evidence nor the investigators will be adversely affected by their use.[1]

One of the most commonly used presumptive tests for the visualization of blood is luminol, which undergoes a chemiluminsecent reaction with the heme groups of blood.[2] This chemiluminescence is visible in the dark.[3] While luminol is highly sensitive, it has a few drawbacks. Luminol is limited to use in a dark environment,[4] gives false positives for a variety of interferents,[5] and has been shown to reduce the recoverable quantity of DNA over time.[6]

Alternative light sources (ALS) are a potential alternative to detection by luminol. The strongest factors In favor of ALS systems are ease-of-use and the fact that ALS systems do not make physical contact with the samples, unlike luminol, which is sprayed directly on the samples of interest. The ALS systems

currently available induce fluorescence of biological molecules or increase the contrast between the biological evidence and its background, typically operating in the ultraviolet and visible wavelength regions.[1]

Infrared (IR) spectroscopy has been suggested as another ALS system. Infrared imaging and spectroscopy have been demonstrated for the analysis of fabrics and bloodstains.[7-10] Recently, a digital camera was sensitized to the near-IR region to allow blood detection.[11] The Myrick lab has recently reported a thermal IR (8 – 14 μm) imaging system using reflectance imaging as a stand-off technique to visualize blood on a fabric.[12-14] This imaging system was based on diffuse reflection (DR) IR spectroscopy, which has also been used to examine fabric composition, dye state, and treatments.[15-22] Near-IR reflectance spectroscopy has been used to investigate blood stains. [23-24]

In the forensic community, a common figure of merit for comparing detection methods is the detection limit (DL), often reported in units of dilution factor. The work presented in this dissertation seeks to establish a DL for blood on fabric using IR DR spectroscopy. This analysis will allow comparison of spectroscopic DLs to DLs using the more common luminol test. Further, investigation of how DLs are influenced by both fabric substrates and spectral windows can inform further instrument development, and the use of a conventional benchtop FT-IR spectrometer will enable fundamental spectroscopic understanding of what the IR imaging system is visualizing.

1.2. DIFFUSE REFLECTION INFRARED SPECTROSCOPY

Infrared spectroscopy is a molecular spectroscopy technique used to investigate the vibrational modes of an analyte. In an IR spectrum, fundamental vibrations generally appear in the range of 400 – 4000 cm^{-1}, which is the mid-IR region.[25] At the higher frequencies of the near-IR, weaker combination and overtone absorbance bands appear. These are generally an order of magnitude or more weaker than the fundamental bands.[26] Our investigation of blood on fabric leads us to look for absorbance bands related to proteins. These bands are the Amide I (1650 cm^{-1}), Amide II (1550 cm^{-1}), Amide A (3300 cm^{-1}), and Amide B (3100 cm^{-1}).[27-29] Other bands less specific to proteins are also present in the mid-IR related to peptide group vibrations and C-H deformation bands. The Amide I band is characteristic of the hydrogen-bonded carbonyl stretch of the peptide backbone. Amide II is related to both C-N stretching and N-H bending. The broad Amide A feature corresponds to the N-H stretch of a secondary amide, while the much weaker Amide B is the second overtone of the Amide II bands strengthened by Fermi resonance with Amide A.[27-29] These distinctive features can be expected to form the basis of calibration for the presence of blood on fabrics.

Transmission measurements are the most common application of IR spectroscopy. However, transmission measurements are not feasible when the sample is highly absorbing or scattering. The measurement of blood on fabric is one such case. Reflectance measurements, specifically DR, provide a good alternative to transmission measurements in these situations. Diffuse reflection

spectroscopy measures the reflection from a sample collected at an angle not equal to the angle of incident radiation, meaning it excludes the signal of specular reflection. Fresnel diffuse reflection (FDR) and Kubelka-Munk, or volume, reflection comprise the signal of DR.[30-31] The volume reflection comes from light that has undergone multiple reflection and refraction events before being scattered out of the sample to the detector. Because of this, it carries chemical information about the particles in the sample, enabling quantitative analysis. When the sample is highly absorbing, any light that would carry this signature is totally attenuated before it can be scattered out of the sample. When that happens, FDR (the reflection off an irregular surface) contributes more significantly to the signal.[32] In our samples, this typically appears as an increase in reflection in areas of high fabric absorbance as the surface coating increases. This signal is not selective for the analyte concentration, so one would expect to see that calibrations are best in regions of the spectrum where FDR contributes minimally to the spectrum.

1.3. MULTIVARIATE CALIBRATION

Some features of IR DR spectra can cause difficulties in forming calibrations. Because FDR is more closely related to the real portion of the refractive index (rather than the imaginary portion related to absorbance), anomalous dispersion can occur in the vicinity of strong absorbance features that typically manifests as asymmetric peaks.[30,32] An even more dominant feature of DR spectra is the variability that arises primarily from scattering in the sample. This scattering manifests as additive and multiplicative effects in the spectra that

can impede further calibration. To prevent this from negatively influencing calibration performance, spectral preprocessing is key.

One method often employed to eliminate baseline effects related to scattering and other phenomena is derivative processing. Derivatives are well known to improve calibration performance by eliminating baseline features and increasing resolution of narrow or overlapping peaks.[33-37] By coupling derivative pretreatment with a correction for multiplicative effects such as the standard normal variate transformation,[38] most variable pathlength effects can be removed.

After the spectra have been properly processed to minimize extraneous variation, multivariate calibration techniques can be employed. These techniques estimate the concentration of the analyte based on the relationship between variables in the data block. Principal components analysis (PCA)[39] and partial least squares regression (PLSR) are two common multivariate calibration techniques.[40-41] Both approaches develop a regression vector (RV) that can be used to predict analyte concentration in an unknown sample after calibration with a known data set. This regression vector is a linear combination of the underlying vectors, either principal components (PCs) or latent variables (LVs). In PCA, the PCs maximize the explained variance in the spectral data set. In PLSR, the LVs maximize the explained covariance of the spectral data set and the concentration vector. In addition to providing predictions, these underlying vectors are useful for examining the more subtle features of the spectra.

The performance of calibration models can be assessed by a few different parameters. The four that will be used here are the root-mean-square error of calibration (RMSEC), root-mean-square error of prediction (RMSEP), the ratio of the standard deviation of the reference values to the RMSEP of the model (RPD),[42] and the DL.[43-44] The RMSEC is given by:

$$\text{Eq. 1.1. } \sqrt{\frac{\sum_{i=1}^{n}(\hat{y}_i - y_i)^2}{n}}$$

where *n* is the number of calibration samples, $\hat{y}$ is the calibration prediction, and *y* are the calibration reference values.[45] To calculate the RMSEP, the validation prediction and reference values are substituted in Eq. 1.1. The equations of the RPD and the DL will be presented in Ch. 3 and Ch. 4, respectively.

1.4. DISSERTATION OUTLINE

Chapters 2-3 of this dissertation explore the implementation and optimization of fourth-order gap derivatives (GDs) as an alternative to the more common Savitzky-Golay (SG) smoothing derivatives. GDs approximate the analytical derivative by calculating finite differences of spectra without curve fitting. GDs offer an advantage of tunability for spectral data as the distance (gap) over which this finite difference is calculated can be varied. Gap selection is a compromise between signal attenuation, noise amplification, and spectral resolution. A method and discussion of the importance of fourth derivative gap selections are presented as well as a comparison to SG preprocessing and lower-order GDs in the context of multivariate calibration. In most cases, we found that optimized GDs led to calibration models perform comparably to or

better than SG derivatives, and that optimized fourth-order GDs behaved similarly to matched filters.

Chapter 4 describes a modification to the GD algorithm to allow the higher-order GDs and the RVs and LVs associated with PLSR models to be integrated exactly. This exact integration allows better interpretation of how gap selection influences calibration performance, and a demonstration of this application is included.

Following the discussion of GD preprocessing, fourth-order GDs are used in conjunction with PLSR to calibrate for blood on fabrics. The DLs are estimated for IR DR spectroscopy using PLSR. While DLs often appear in terms of dilution factor in the forensic community, mass percentage, coverage (mass per unit area), or film thickness are often more relevant when comparing experimental methods. These alternate DL units are related to one another and presented here. The DLs for blood using IR spectroscopy are also compared to those reported using luminol or an alternative IR imaging system

Chapter 6 deviates a bit from the theme by presenting a method to investigate the heating at an electrode surface using an IR camera. This method involves looking at the back surface of a platinum working electrode to examine the heating and cooling cycles of the electrode in relation to the potential cycles during a cyclic voltammetry experiment. Examination of this type offers insight to the processes occurring at an electrode during redox reactions.

The final chapter looks forward to work that could expand on the results presented throughout the dissertation. First, a brief discussion of the possibility of

extending the concept of GDs as matched filters to the development of matched filters for spectral processing prior to multivariate calibration is presented. Following that, the possibility of modifying PLSR calibrations to improve DLs by minimizing variance of the predictions of blank samples is discussed. Initial results show the possibility of DLs improved by a factor of 2 while using fewer LVs in the final model.

REFERENCES

(1) W. C. Lee, B. E. Khoo. “Forensic Light Sources for Detection of Biological Evidences in Crime Scene Investigation: A Review”. Malaysian Journal of Forensic Sciences. 2010, 1: 17-27.

(2) J. L. Webb, J. I. Creamer, T. I. Quickenden. “A comparison of the presumptive luminol test for blood with four non-chemiluminescent forensic techniques”. Luminescence. 2006. 21(4): 214-220.

(3) T. I. Quickenden, C. P. Ennis, J. I. Creamer. “The forensic use of luminol chemiluminescence to detect traces of blood inside motor vehicles”. Luminescence. 2004, 19: 271-277.

(4) K. Virkler, I. K. Lednev. "Analysis of body fluids for forensic purposes: From laboratory testing to non-destructive rapid confirmatory identification at a crime scene". Forensic Sci. Int. 2009, 188(1): 1-17.

(5) T. I. Quickenden, J. I. Creamer. "A study of common interferences with the forensic luminol test for blood". Luminescence 2001, 16(4): 295-298.

(6) J. P. de Almeida, N. Glesse, C. Bonorino. "Effect of presumptive tests reagents on human blood confirmatory tests and DNA analysis using real time polymerase chain reaction". Forensic Sci. Int. 2011, 206(1): 58-61.

(7) G. van Dalen. "Protein on Cloths: Evaluation of Analytical Techniques". Appl. Spectrosc. 2000, 54(9): 1350-1356.

(8) A. Farrar, G. Porter, A. Renshaw. "Detection of Latent Bloodstains Beneath Painted Surfaces Using Reflected Infrared Photography". J. Forensic Sci. 2012, 57(5): 1190-1198.

(9) M. A. Raymond, R. L. Hall. "An Interesting Application of Infrared Reflection Photography to Blood Splash Pattern Interpretation". Forensic Sci. Int. 1986, 31(3): 189-194.

(10) M. Perkins. "The Application of Infrared Photography in Bloodstain Pattern Documentation of Clothing". J. Forensic Ident. 2005, 55(1): 1-9.

(11) A. C. Lin, H. Hsieh, L. Tsai, A. Linacre, J. C. Lee. "Forensic applications of infrared imaging for the detection and recording of latent evidence". J. Forensic Sci. 2007, 52(5): 1148-1150.

(12) H. Brooke, M. R. Baranowski, J. N. McCutcheon, S. L. Morgan, M. L. Myrick. "Multimode Imaging in the Thermal Infrared for Chemical Contrast Enhancement. Part 1: Methodology". Anal. Chem. 2010, 82(20): 8412-8420.

(13) H. Brooke, M. R. Baranowski, J. N. McCutcheon, S. L. Morgan, M. L. Myrick. "Multimode Imaging in the Thermal Infrared for Chemical Contrast Enhancement. Part 2: Simulation Driven Design". Anal. Chem. 2010, 82(20): 8421-8426.

(14) H. Brooke, M. R. Baranowski, J. N. McCutcheon, S. L. Morgan, M. L. Myrick. "Multimode Imaging in the Thermal Infrared for Chemical Contrast Enhancement. Part 3: Visualizing Blood on Fabrics". Anal. Chem. 2010, 82(20): 8427-8431.

(15) M. R. Pearl, H. Brooke, J. N. McCutcheon, S. L. Morgan, M. L. Myrick. "Coating Effects on Mid-Infrared Reflection Spectra of Fabrics". Appl. Spectrosc. 2011, 65(8): 876-884.

(16) N. M. Morris. "A Comparison of Sampling Techniques for the Characterization of Cotton Textiles by Infrared-Spectroscopy". Text. Chem. Color. 1991, 23(4): 19-22.

(17) S. Ghosh, M. D. Cannon, R. B. Roy. "Quantitative-Analysis of Durable Press Resin on Cotton Fabrics Using near-Infrared Reflectance Spectroscopy". Text. Res. J. 1990, 60(3): 167-172.

(18) C. Gilbert, S. Kokot. "Discrimination of Cellulosic Fabrics by Diffuse-Reflectance Infrared Fourier-Transform Spectroscopy and Chemometrics". Vib Spectrosc. 1995, 9(2): 161-167.

(19) C. Gilbert, S. Kokot, U. Meyer. "Application of Drift Spectroscopy and Chemometrics for the Comparison of Cotton Fabrics". Appl. Spectrosc. 1993, 47(6): 741-748.

(20) S. Kokot, K. Crawford, L. Rintoul, U. Meyer. "A DRIFTS study of reactive dye states on cotton fabric". Vib. Spectrosc. 1997, 15(1): 103-111.

(21) H. M. Heise, R. Kuckuk, A. Bereck, D. Riegel. "Mid-infrared diffuse reflectance spectroscopy of textiles containing finishing auxiliaries". Vib. Spectrosc. 2004, 35(1): 213-218.

(22) H. M. Heise, R. Kuckuk, U. Damm, A. Bereck, D. Riegel. "Quantitative diffuse reflectance infrared spectroscopy of cotton fabrics treated with a cyclodextrin derivative finishing auxiliary". J. Mol. Struct. 2005, 744: 877-880.

(23) E. Botonjic-Sehic, C. W. Brown, M. Lamontagne. M. Tsaparikos. "Forensic Application of Near-Infrared Spectroscopy: Aging of Bloodstains". Spectroscopy 2009, 24(2): 42-48.

(24) G. Edelman, V. Manti, S. M. van Ruth, T. van Leeuwen, M. Aalders. "Identification and age estimation of blood stains on colored backgrounds by near infrared spectroscopy". Forensic Sci. Int. 2012, 220(1): 239-244.

(25) B C. Smith. Fundamental of Fourier Transform Infrared Spectroscopy. New York: CRC Press, 1996.

(26) J. M. Olinger, P. R. Griffiths. “Theory of Diffuse Reflectance in the NIR Region”. In: D. A. Burns, E. W. Ciurczak, editors. Handbook of Near-Infrared Analysis. New York: Marcel Dekker, Inc., 1992

(27) J. T. Kuenstner, Norris, K. H., V. F. Kalasinsky. "Spectrophotometry of Human Hemoglobin in the Midinfrared Region". Biospectroscopy. 1997, 3: 225-232.

(28) K. T. Hecht, D. L. Wood. "The near Infra-Red Spectrum of the Petide Group". Proc. R. Soc. A. 1956, 235(1201): 174-188.

(29) A. J. Sadler, J. G. Horsch, E. Q. Lawson, D. Harmatz, D. T. Brandau, C. R. Middaugh. "Near-Infrared Photoacoustic-Spectroscopy of Proteins". Anal. Biochem. 1984, 138(1): 44-51.

(30) P. J. Brimmer, P. R. Griffiths, N. J. Harrick. “Angular-Dependence of Diffuse Reflectance Infrared-Spectra .1. Ft-Ir Spectrogoniophotometer”. Appl. Spectrosc. 1986**,** 40(2): 258-265.

(31) M. L. Myrick, M. N. Simcock, M. Baranowski, H. Brooke, S. L. Morgan, J. N. McCutcheon. “The Kubelka-Munk Diffuse Reflectance Formula Revisited”. Appl. Spectrosc. Rev. 2011, 46(2): 140-165.

(32) M. L. Myrick, S. L. Morgan. “Infrared Specular Reflection Calculated for Polymer Films on Polymer Substrates: Models for the Spectra of Coated Plastics”. Spectroscopy. 2012, 40-56.

(33) W. L. Butler. "Fourth Derivative Spectra". Methods Enzymol. 1979. 56: 501-515.

(34) W. L. Butler, D. W. Hopkins. "Analysis of Fourth Derivative Spectra". Photochem. Photobiol. 1970. 12(6): 451-456.

(35) W. L. Butler, D. W. Hopkins. "Higher Derivative Analysis of Complex Absorption Spectra". Photochem. Photobiol. 1970. 12(6): 439-450.

(36) J. E. Cahill. "Derivative Spectroscopy - Understanding Its Application". Am. Lab. 1979. 11(11): 79-85.

(37) K. H. Norris, P. C. Williams. "Optimization of Mathematical Treatments of Raw Near-Infrared Signal in the Measurement of Protein in Hard Red Spring Wheat. 1. Influence of Particle-Size. Cereal Chem. 1984. 61(2): 158-165.

(38) R. J. Barnes, M. S. Dhanoa, S. J. Lister. "Standard Normal Variate Transformation and De-Trending of Near-Infrared Diffuse Reflectance Spectra". Appl. Spectrosc. 1989. 43(5): 772-777.

(39) M. Hubert. "Robust Calibration". In: P. J. Gemperline, editor. Practical Guide to Chemometrics. New York: Taylor & Francis, 2006. 2nd ed. Ch. 6, Pp. 167-215.

(40) M. Sjostrom, S. Wold, W. Lindberg, J. Persson, H. Martens. "A Multivariate Calibration Problem in Analytical chemistry Solved by Partial Least-Squares Models in Latent Variables". Anal. Chim. Acta. 1983, 150: 61-70.

(41) S. de Jong. "SIMPLS: an alternative approach to partial least squares regression". Chemom. Intell. Lab. Syst. 1993, 18: 251-263.

(42) P. C. Williams. "Implementation of Near-Infrared Technology". In: P. C. Williams, K. H. Norris, editors. Near-Infrared Technology in the Agricultural and Food Industries. St. Paul, USA: American Association of Cereal Chemists, 2001. 2nd ed. Ch. 8, Pp. 145-170.

(43) L. A. Currie. "Nomenclature in Evaluation of Analytical Methods Including Detection and Quantification Capabilities". Pure Appl. Chem. 1995, 67(10): 1699-1723.

(44) R. Boqué, F. X. Rius. "Multivariate dection limits estimators". Chemom. Intell. Lab. Syst. 1996, 32: 11-23.

(45) H. Martens, T. Naes. Multivariate Calibration. New York: Wiley, 1989.

CHAPTER 2

INFLUENCE OF GAP SELECTION ON THE PERFORMANCE OF GAP DERIVATIVES

2.1. INTRODUCTION

Derivatives are a commonly applied preprocessing tool for multivariate calibration. Derivatives offer many benefits, including reducing the effect of baseline slope or offset, resolving overlapping peaks, and enhancing narrow features.[1-4] Derivatives also have some drawbacks impeding their implementation. Derivative spectra are more complicated than their zero-order analogues, featuring n + 1 peaks for each peak in the original spectrum (where n is the derivative order).[1] These extra peaks appear as side lobes that interfere with one another and with neighboring peaks, causing reduction of peak heights or development of artificial peaks. Further, compromises must be struck when optimizing parameters to balance resolution enhancement, signal distortion, noise amplification, and signal attenuation in the derivative spectrum.[5]

Two of the most commonly applied derivatives are Savitzky-Golay (SG) smoothing derivatives and segment-gap derivatives. This work will focus on the use of segment-gap derivatives which approximate the analytical derivative (AD) of the spectrum by computing a finite difference between intensity values averaged over segments separated by some gap. In the absence of noise, the difference approaches the true derivative as the gap approaches zero.[6] In some

cases, the segment is equal to one and no averaging occurs, resulting in a simple gap derivative (GD), sometimes referred to as a finite difference, Norris, or Butler-Hopkins derivative.[1-3,7-10] GD computation is often coupled with a smoothing routine, though that is not always necessary or desirable. Higher order derivatives are obtained by repeating the differentiation sequentially.

The greatest impetus for using SG derivatives rather than GDs is the smoothing effect of fitting a polynomial to the data first. However, GDs coupled with smoothing routines or using different gap sizes for iterative differentiation have been shown to yield results comparable to or better than SG.[8-10] Other work has shown that each GD performed with gap *g* is similar to a *g*-point sliding average smooth.[4,11] Further, early workers suggested that in systems with lower noise levels, smoothing would be less necessary and higher-order derivatives with greater resolution enhancement would be favored for use.[1-3,12-13] With the advent and widespread use of interferometry in the infrared, spectra now have noise levels consistently low enough to favor the use of higher-order derivatives without the need for separate smoothing routines.

The usefulness of GDs largely depends on the selection of an appropriate gap size for the calculation. Previous literature has explored the influence of gap size on spectral shape and intensity, generally focusing on maximizing peak resolution while minimizing noise influences and signal distortion. The general observations included decreasing signal-to-noise ratio (SNR) with increasing derivative order, increasing SNR with increasing gap size, and advantages related to using different gap sizes in derivative iterations. The rule of thumb has

thus far been a gap size approximately equal to the full-width at half-maximum (FWHM) of the peak of interest.[1-4,8-10,12,14] This work will present the calculation of GDs and demonstrate the influence of gap selection on the resulting derivative signal and noise.

2.2. GAP DERIVATIVE CALCULATION

The equation for computing the GD comes in a variety of forms in the literature, differing primarily on two points: how the gap (distance between points used in the calculation) is defined and whether to divide the difference in spectral intensity by the gap.[2,7,14] The fundamental concept of the derivative is the slope of the zero-order spectrum, the change in *y* divided by the change in *x*.[4] This basic definition leads to the equation of a first-order derivative:

$$\text{Eq. 2.1} \qquad f'(x) = \frac{f(x+g/2)-f(x-g/2)}{g}$$

where *g* is the defined gap size.[4] As discussed earlier, this operation can be repeated on the data *n* times to yield the *n*th-order derivative. This iteration will yield a convolution function with coefficients given by the *n*th row of Pascal's triangle.[1] The second-order derivative, when the same gap is chosen for each derivative step, is given by:

$$\text{Eq. 2.2} \qquad f''(x) = \frac{f(x+g)-2f(x)+f(x-g)}{g^2}$$

For each derivative calculated, a new gap can be selected. By using *n* different gaps (a unique gap for each iteration of the derivative calculation), a greater number of data points are included in the overall calculation, aiding in the suppression of noise and reducing the development of periodic oscillations of reinforced noise in the derivative.[1] The order in which these *n* different gaps are

used in the calculation does not influence the final derivative. The equation for a fourth-order derivative in the same form as the preceding equation is:

$$\text{Eq. 2.3} \qquad f''''(x) = \frac{f(x+2g)-4f(x+g)+6f(x)-4f(x-g)+f(x-2g)}{g^4}$$

2.3. INFLUENCE OF GAP SIZE ON DERIVATIVE SHAPE FOR A LORENTZIAN BANDSHAPE

A Lorentzian lineshape is described by Eq. 2.4,

$$\text{Eq. 2.4} \qquad y = \frac{1}{\pi}\frac{2\Gamma}{4(x-x_0)+\Gamma^2}$$

where x_0 is the center of the band and Γ is the FWHM of the lineshape. For our discussion below, we generalize the function by introducing the unitless variables $\hat{y} = y/y_{\max}$ and $\hat{x} = (x - x_0)/\Gamma$, reducing Eq. 2.4 to the form:

$$\text{Eq. 2.5} \qquad \hat{y} = \frac{1}{4\hat{x}^2+1}$$

(see Fig. 2.1a). Expressions for the ADs and GDs of $\hat{y}$ for orders 1, 2, and 4 are provided in Table 2.1, where the unitless gap $\hat{g} = g/\Gamma$ is introduced for the GDs to relate the implemented gap size in terms of a fraction of the FWHM of the Lorentzian. From Table 2.1, it is evident that the GD approaches the AD for each order as $\hat{g}$ approaches zero.

Figure 2.1b-d illustrate the influence of gap size and derivative order on the magnitude of the resulting derivative function for the curve in Fig. 2.1a. The first-, second-, and fourth-order GDs are shown with $\hat{g}$ = 0.1, 0.5, 1, and 2, along with the AD. As the derivative order increases, the maxima and minima of GDs deviate more from the corresponding ADs proportionally to the FWHM^n (Thus, the derivatives in Fig. 2.1 are scaled accordingly). In addition, as the gap size increases, the GD shape distorts from that of the AD. This distortion occurs to the

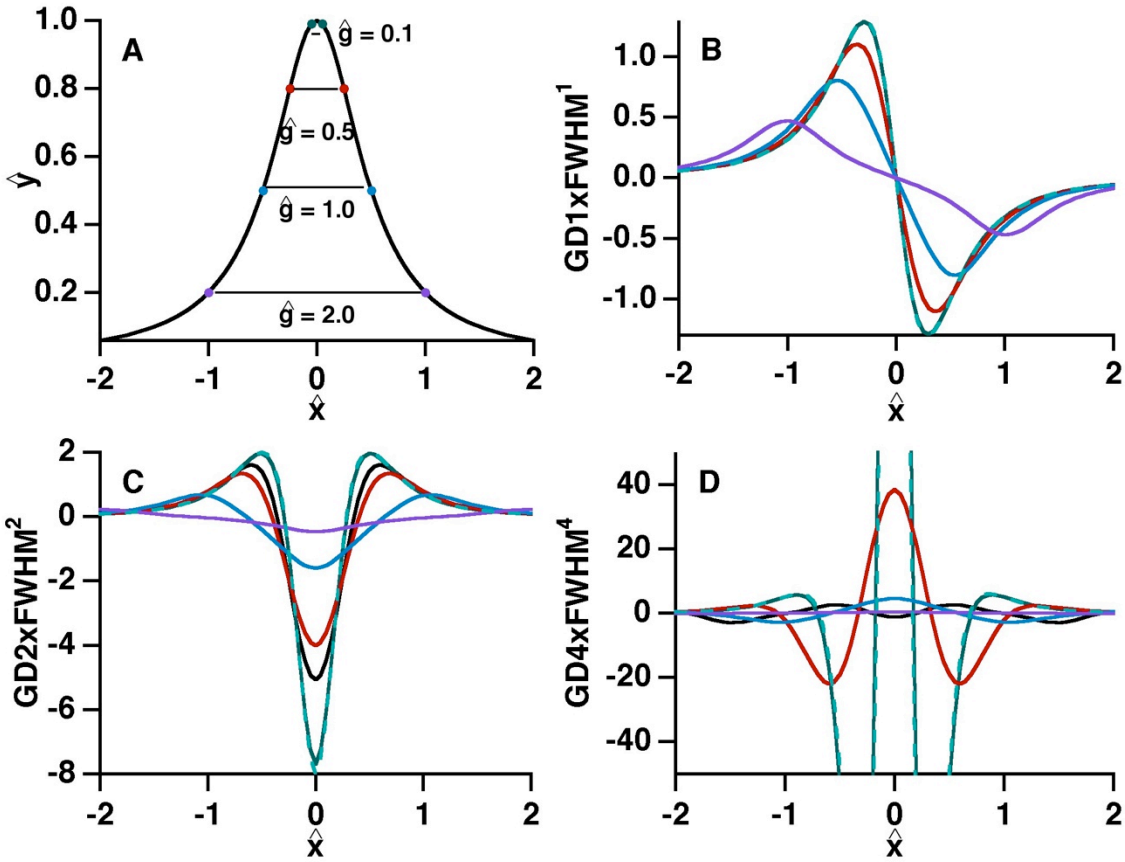

Fig. 2.1: Gap Derivatives. From a-d, the GD0, GD1, GD2, and GD4 of a Lorentzian curve (centered at 0) are shown. Each derivative plot shows the AD (dashed line), and GD with $\hat{g}$ = 0.1 (dark green), 0.5 (red), 1.0 (blue), and 2.0 (purple). On c-d, the black trace shows the GD calculated with multiple gaps (see text). The GD deviates from the true derivative proportionally to derivative order and gap size. Gap sizes are given in units of FWHM to show the influence of gap size relative to the FWHM of the peak. Each derivative is scaled by the FWHM^n. For n = 4, the scale has been adjusted to show the derivative calculated with larger gap sizes. The maximum of GD4 with $\hat{g}$ = 0.1is off-scale at approximately 318 units.

Table 2.1: Derivatives of $\hat{y}$ with respect to $\hat{x}$, simplified by the introduction of variable $a = 4\hat{x}^2 + 1$.

n	Analytical Derivative	Gap Derivative
0	$\frac{1}{a}$	
1	$\frac{-8x}{a^2}$	$\frac{-8x}{(g^2 + 4gx + a)(g^2 - 4gx + a)}$
2	$\frac{8(12x^2 - 1)}{a^3}$	$\frac{8(12x^2 - 4g^2 - 1)}{(4g^2 + 8gx + a)(a)(4g^2 - 8gx + a)}$
4	$\frac{384(80x^4 - 40x^2 + 1)}{a^5}$	$\frac{384(64g^4 - 240g^2x^2 + 80x^4 + 20g^2 - 40x^2 + 1)}{(16g^2 + 16gx + a)(4g^2 + 8gx + a)(a)(4g^2 - 8gx + a)(16g^2 - 16gx + a)}$

point that GD1 determined with $\hat{g}$ = 2 no longer appears as a derivative; rather, the trace resembles a positive image of the band shifted by -$\hat{g}$ connected to a negative image of the band shifted by +$\hat{g}$. Both of these images of the band have an intensity approximately one-half that of the original band. As $\hat{g}$ is increased beyond 1, the GD no longer offers a good approximation of the AD. Because of this, narrow gaps are preferred for the purpose of simulating a true AD for visual inspection.[2]

When different gap sizes are used for each iteration of the derivative calculation, the resulting GD deviates from both the AD and the above noted trends in the relationship between gap size, derivative order, and the GD shape (black traces in Fig. 2.1c-d). For example, the GD2 calculated with $\hat{g}_1$ = 0.1 and $\hat{g}_2$ = 0.5 has a maximum intensity intermediate between that obtained with either gap size $\hat{g}_1$ or gap size $\hat{g}_2$, alone (Fig. 2.1c). Similarly, GD4 calculated with four different gaps ($\hat{g}_1$ = 0.1, $\hat{g}_2$ = 0.5, $\hat{g}_3$ = 1, $\hat{g}_4$ = 2) does not simply resemble the derivative calculated with any single gap size (Fig. 2.1d); the center peak of that GD4 spectrum inverts relative to the center peak of the other GD4 spectra. Though this deviation from the expected derivative shape may complicate peak identification by visual inspection, it will be consistent among similar peaks and should not necessarily be expected to impede multivariate calibration.[4]

2.4. INFLUENCE OF GAP SIZE ON SNR FOR A LORENTZIAN BANDSHAPE

While narrow gaps are preferred for the simulation of a true AD, narrow gaps tend to decrease the SNR of the curve to an unacceptable level when noise is present. Figure 2.2a shows the same Lorentzian curve displayed in Fig. 2.1a,

with noise added to give a SNR = 10. The GD4 with $\hat{g}$ = 0.1, in which the Lorentzian derivative feature is completely obscured by noise, is shown in Fig. 2.2b. The GD4 calculated with $\hat{g}$ = 1 is shown in Fig. 2.2c. Here, the central peak has become visible above the noise once again, despite the much lower signal value of the GD. In this case, the wider gap is preferable to the narrow gap because the wide gap offers an advantage of effectively smoothing the noise as the derivative is calculated, preventing the noise from masking the signal.

The maximum signal magnitude of a GD is related to the original signal magnitude as shown in Fig. 2.3, drawn to log scale (solid traces in left column). Table 2.2 gives equations for the maximum signal magnitude of GD1, GD2, and GD4 as a function of the gap size $\hat{g}$. The magnitudes of all these derivatives fall as $\hat{g}^{-n}$ for large $\hat{g}$ where *n* is the derivative order. For GD1, the position of the maximum signal amplitude is not at the center of the Lorentzian band, resulting in a more complicated formula. For even-order derivatives, the maximum signal magnitude is located at $\hat{x} = 0$, the center of the Lorentzian band. All the signal magnitudes are greatest with $\hat{g} \geq 0$, with magnitudes of $\frac{3\sqrt{3}}{4}$, 8, and 384 for GD1, GD2, and GD4, respectively. All these signal magnitudes fall as a function of increasing $\hat{g}$ with a somewhat Lorentzian form. For GD2, this form is explicitly Lorentzian with $\Gamma_{\mathrm{GD2}} = 1$. The GD4 signal magnitude falls as the product of two Lorentzians, one with $\Gamma_{\mathrm{GD4a}} = 1$ and the other with $\Gamma_{\mathrm{GD4b}} = 0.5$.

Assuming the noise is equal at every wavelength channel in the original spectrum before differentiation, the noise in a GD is also affected by $\hat{g}$ and *n*

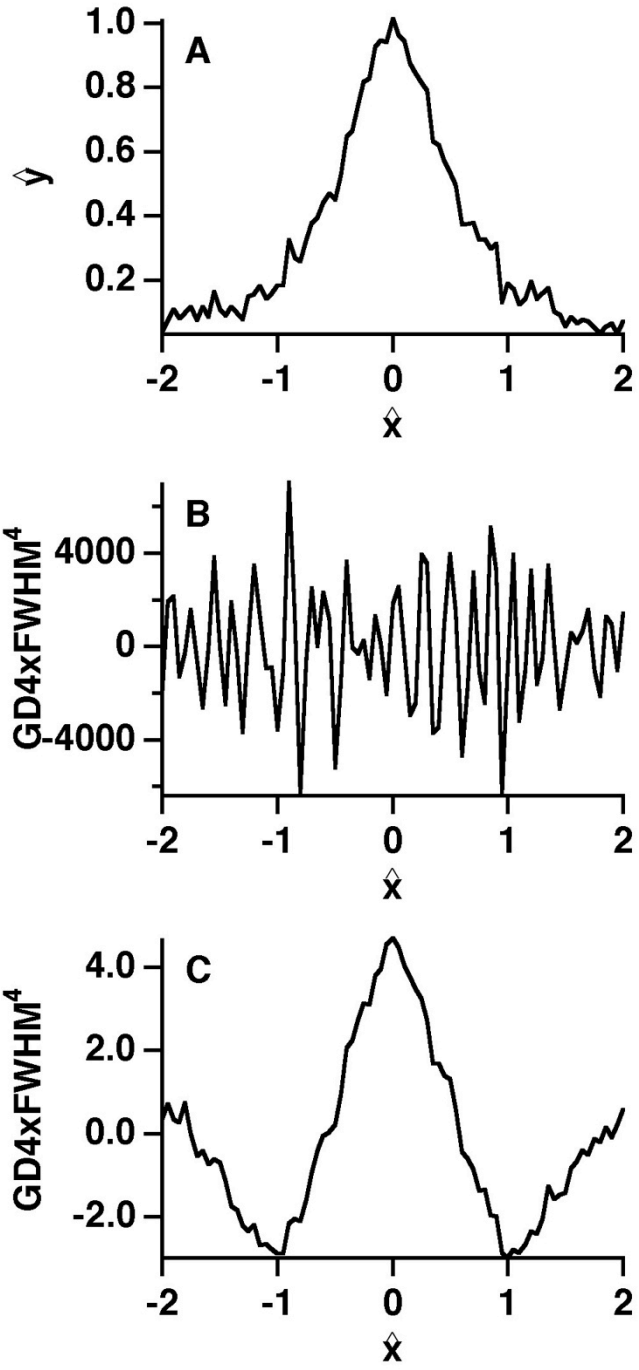

Fig. 2.2: GD4 of Lorentzian with SNR = 10. (a) The curve from Fig. 2.1a (center at 0, FWHM = 1) with white gaussian noise added. (b) GD4 of (a) with $\hat{g}$ = 0.1. The noise is enhanced relative to the signal and completely obscures the peak. (c) GD4 of (a) with $\hat{g}$ = 1.0. The signal is now clearly visible above the noise, though the amplitude is much lower.

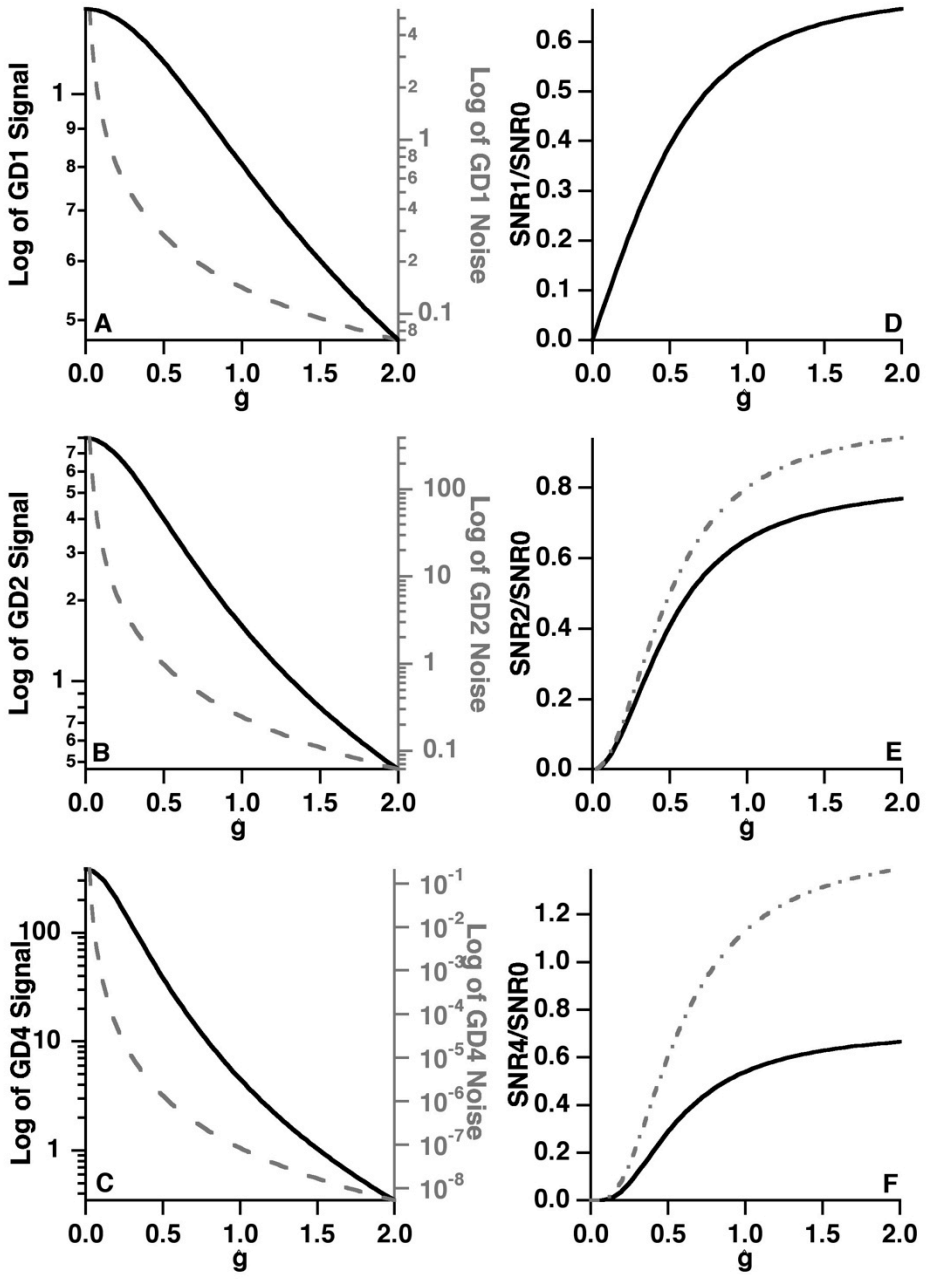

Fig. 2.3: SNR of GDs. Panels a/d, b/e, and c/f display information for GD1, GD2, and GD4, respectively, of the Lorentzian curve in Fig. 2.2a. The left column shows the change in signal (solid) and noise (dashed) of the GD as a function of $\hat{g}$. With increasing $\hat{g}$ at all *n*, the magnitude of both the signal and the noise decreases, though the noise decreases more rapidly. The right column displays relative SNR*n* (SNR of GD*n* divided by SNR of the original curve) as a function of $\hat{g}$. For all *n*, SNR*n*/SNR0 increases rapidly as $\hat{g}$ approaches 1, then begins to plateau. The dashed trace shows the relative SNR*n* when multiple $\hat{g}$ are used. This allows the SNR2 to approach the SNR0, and SNR4 exceeds SNR0 for $\hat{g}$ > 0.8.

Table 2.2: Maximum values of GDs.

Order	Gap Derivative Maximum
1	$\frac{3\sqrt{-3+3\hat{g}^2+6\sqrt{\hat{g}^4+\hat{g}^2+1}}}{-\hat{g}^2\left(-3+3\hat{g}^2+6\sqrt{\hat{g}^4+\hat{g}^2+1}\right)+\left(2\hat{g}^2+\sqrt{\hat{g}^4+\hat{g}^2+1}+1\right)^2}$
2	$\frac{-8}{(4\hat{g}^2+1)}$
4	$\frac{384}{(16\hat{g}^2+1)(4\hat{g}^2+1)}$

according to Eq. 2.6:

$$\text{Eq. 2.6} \qquad \sigma_{\mathrm{GD}n} = \sigma_0 \frac{\sqrt{\sum_{i=1}^{n+1} c_i^2}}{\hat{g}^n}$$

where c_i is the i^{th} binomial coefficient in the n^{th} row of Pascal's triangle and σ_0 is the standard deviation of the noise in a channel of the original spectrum. This equation is obtained by propagation of errors from a definition of the GD with a single gap in terms of the original spectral channels (Eq. 2.2). The noise in the GDs (Fig. 2.3, dashed traces in left column) falls as a function of $\hat{g}$ more quickly than the GD signal for small and intermediate $\hat{g}$. This suggests that the SNR of the derivative spectrum will improve with increasing gap size for small and intermediate $\hat{g}$ and plateau for larger values of $\hat{g}$. This is found to be the case, as shown in the right column of Fig. 2.3. For each derivative order, the SNR of the derivative spectrum increases rapidly as $\hat{g}$ approaches about 0.8. The SNR then tends toward a plateau as $\hat{g}$ ~ 2. However, regardless of the value of $\hat{g}$, the derivative spectra using a single value of $\hat{g}$ have lower SNR values than the original spectrum from which they were created. For instance, for $\hat{g}$ = 1, GD1, GD2, and GD4 have relative SNRs (SNR*n*/SNR0) of 0.57, 0.65, and 0.54, respectively, where SNR0 is the signal-to-noise ratio of the original spectrum and SNR*n* is the signal-to-noise ratio of the GD*n* spectrum. SNR*n* for all *n* is degraded compared to the original spectrum, with the least degradation found in the second-order derivative. The lack of a clear trend in these values is a result of comparing even and odd orders of differentiation.

Incorporating more points in a GD calculation can improve SNR*n* by reducing spectral noise without affecting the signal. To do this, GDs are

calculated with a different gap size $\hat{g}$ for each step of differentiation. The signal is not degraded further if the additional gap sizes incorporated do not diminish the signal significantly. The SNR of n^{th}-order GDs calculated with multiple gaps (SNRn_{mg}) with this constraint is approximated by:

$$\text{Eq. 2.7} \qquad \text{SNR}n_{\text{mg}} \approx \text{SNR}n\sqrt{\frac{\sum_{i=1}^{n+1} c_i^2}{2^n}}$$

where again the coefficients squared in the summation are from row *n* of Pascal's triangle. Since the sum of the elements of row *n* of Pascal's triangle always equals 2^n, and since no values found in the triangle are less than unity, the SNR*n* (*n*>1) of a higher-order GD when multiple values of $\hat{g}$ are used will always exceed the SNR of the same GD when a single $\hat{g}$ is used. Because only one gap is possible in GD1, it is not improved by using multiple gaps in this way, but could be improved by a gap-segment approach with a segment greater than one that is not discussed here.[6-7]

Relative SNRn_{mg} for GDs is shown in dashed traces in the right column of Fig. 2.3. The relative SNR2$_{\text{mg}}$ (with $\hat{g}_1$ and $\hat{g}_2$ both approximately 1) of GD2 is now improved by a factor of $\sqrt{6/4}$, to 0.80, and continues to increase with $\hat{g}$ although never exceeding unity. For GD4, the improvement is $\sqrt{70/16}$, resulting in a relative SNR4$_{\text{mg}}$ of 1.13 with all $\hat{g}$ values close to 1. In this case, SNR4$_{\text{mg}}$ exceeds that of SNR0, and continues to increase with $\hat{g}$ up to a maximum of about 1.4, well past the point that the result resembles a true derivative.

2.5. CONCLUSIONS

The selection of gap sizes used in the calculation of GDs at any order is a compromise between noise and signal. While small gap sizes might be preferred to approximate an analytical derivative, they have the disadvantage of decreasing the SNR of the derivative spectrum. Large gap sizes effectively smooth high-frequency noise in the derivative spectrum, but also tend to reduce the amplitude of narrow spectral features. The shape of spectral features that should be highlighted or resolved from spectral interferences will largely influence the optimal gap combination for GD spectral processing. The next chapter will demonstrate how this interplay influences gap selection for the calibration of infrared diffuse reflection spectra.

REFERENCES

(1) W. L. Butler. "Fourth Derivative Spectra". Methods Enzymol. 1979. 56: 501-515.

(2) W. L. Butler, D. W. Hopkins. "Analysis of Fourth Derivative Spectra". Photochem. Photobiol. 1970. 12(6): 451-456.

(3) W. L. Butler, D. W. Hopkins. "Higher Derivative Analysis of Complex Absorption Spectra". Photochem. Photobiol. 1970. 12(6): 439-450.

(4) J. E. Cahill. "Derivative Spectroscopy - Understanding Its Application". Am. Lab. 1979. 11(11): 79-85.

(5) R. I. Shrager. "Some Pitfalls in the Use of Derivative Spectra". Photochem. Photobiol. 1983. 38(5): 615-617.

(6) D. W. Hopkins. "What is a Norris derivative?". NIR news. 2001. 12(3): 3-5.

(7) K. H. Norris, P. C. Williams. "Optimization of Mathematical Treatments of Raw Near-Infrared Signal in the Measurement of Protein in Hard Red Spring Wheat. 1. Influence of Particle-Size. Cereal Chem. 1984. 61(2): 158-165.

(8) W. F. Maddams, W. L. Mead. "The Measurement of Derivative IR-Spectra. 1. Background Studies". Spectrochim. Acta, Part A. 1982. 38(4): 437-444.

(9) S. Hawkes, W. F. Maddams, W. L. Mead, M. J. Southon. "The Measurement of Derivative IR-Spectra. 2. Experimental Measurements". Spectrochim. Acta, Part A. 1982. 38(4): 445-457.

(10) W. F. Maddams, M. J. Southon. "The Measurement of Derivative IR-Spectra. 3. The Effect of Bandwidth and Band Shape on Resolution Enhancement by Derivative Spectroscopy". Spectrochim. Acta, Part A. 1982. 38(4): 459-466.

(11) T. C. O'Haver, T. Begley. "Signal-to-Noise Ratio in Higher-Order Derivative Spectrometry". Anal. Chem. 1981. 53(12): 1876-1878.

(12) G. Talsky, L. Mayring, H. Kreuzer. "High-Resolution, Higher-Order UV-Vis Derivative Spectrophotometry". Angew. Chem. Int. Edit. 1978. 17(11): 785-799.

(13) W. F. Maddams. "The Scope and Limitations of Curve Fitting". Appl. Spectrosc. 1980. 34(3): 245-267.

(14) K. H. Norris. "Applying Norris Derivatives. Understanding and correcting the factors which affect diffuse transmittance spectra". NIR news. 2001. 12(3): 6-9.

CHAPTER 3

OPTIMIZED GAP DERIVATIVES AS MATCHED FILTERS

3.1. INTRODUCTION

The theoretical work described in the previous chapter demonstrated how the selection of gap sizes in gap derivative (GD) preprocessing routines could greatly influence the resulting derivative quality. Of particular interest is the demonstration of how the noise in the derivative can be suppressed relative to the noise in the original signal by incorporating multiple gap sizes in the calculation of higher-order derivatives. As mentioned in Chapter 2, Savitzky-Golay (SG) derivatives are typically favored over GDs to approximate the analytical derivative (AD) because of the smoothing inherent in their calculation: SG derivatives are determined by taking the AD of a polynomial fit to a region (the window) of the spectrum. This smoothing effect suggests that calibrations performed with SG derivatives should always perform comparably to or better than GDs.[1-2] However, if appropriate gap sizes are used for the GD calculation, this may no longer be expected to hold true.

This chapter compares the performance of first-, second-, and fourth-order derivatives calculated by the SG and GD methods to enhance multivariate calibration performance. The parameters of both methods were optimized prior to comparison. The influence of gap size selection on calibration results is demonstrated here, particularly as a function of the band width of the peaks of

greatest influence on the calibration. The gap size combinations were optimized for GDs by partial least-squares regression (PLSR) for the purposes of relative quantification rather than the more traditional application to peak identification and resolution. Optimum GD functions, particularly fourth-order GD functions, are acting in part as matched filters for analyte spectral features.

3.2. METHOD

3.2.1. Sample Preparation Twenty-five sample squares (2” X 2”) each of triple-dyed, unfinished brown polyester, purple acrylic, and red cotton fabrics were cut from large swatches. These samples were sonicated for 60 min in deionized (DI) water and suspended to dry for about 24 h. Five squares of each fabric were dip-coated from each of the following solutions: (1) DI water, (2) 25x dilute rat blood in DI water, (3) 50x dilute rat blood in DI water, (4) 100x dilute rat blood in DI water, (5) 200x dilute rat blood in DI water. The treated fabrics were again suspended to dry before spectroscopic measurements. Five replicate sample sets were created for each fabric by grouping one sample square of each of the 5 solutions into a set.

3.2.2. Spectral Collection Infrared diffuse reflection spectra were collected on a Thermo-Nicolet Nexus 470 FT-IR spectrometer (Thermo Electron, Madison, WI) with a U-Cricket diffuse reflectance accessory (Harrick Scientific Products, Pleasantville, NY). A two-inch diameter gold diffuse reflection standard was used as a reference (Optronics Laboratories, Inc.). Twenty replicate spectra were collected from each of the 75 fabric squares by translating the fabric square over the sampling aperture of the accessory between each measurement. Fabric weave and orientation remained constant throughout data collection to minimize

that source of spectral variability. All the spectra of each sample set were collected in one day, with the spectra of replicate sample sets collected over five consecutive days. Parameters for spectral acquisition were: 600-7000 cm^{-1} spectral range (3320 spectral points), 64 scans, 4 cm^{-1} resolution, laser modulation frequency of 10 KHz, Happ-Genzel apodization, and Mertz phase correction. The spectrometer uses a liquid nitrogen cooled MCT detector and KBr beamsplitter and is operated by OMNIC® software (Thermo, Madison, WI).

3.2.3. Outlier Detection Data were saved as text files in OMNIC® and processed with MATLAB 7.13 (The MathWorks, Inc., Natick, MA). Prior to calibration, spectra were tested for outliers. Spectra were normalized by the standard normal variate transform[3] (SNV) and decomposed by principal component analysis. The spectra of each dilution were tested for outliers by Hotelling's T-squared test statistic.[4] Outliers were removed from further analysis. The sample sets were then tested against one another. Of the five sample sets, no sets were detected as outliers. However, due to a change in the accessory, the spectra of one sample set of each fabric appeared to be outliers upon visual inspection of the data and so were removed from further analysis. The remaining data were split into calibration and validation sets, with three sample sets retained for calibration (~60 spectra at each dilution for each fabric) and one sample set retained for validation (~20 spectra at each dilution) of the model. Figure 3.1a-c shows the mean spectra over the range of spectral collection, and Figure 3.2a-f shows the mean spectra of regions of protein absorbance of

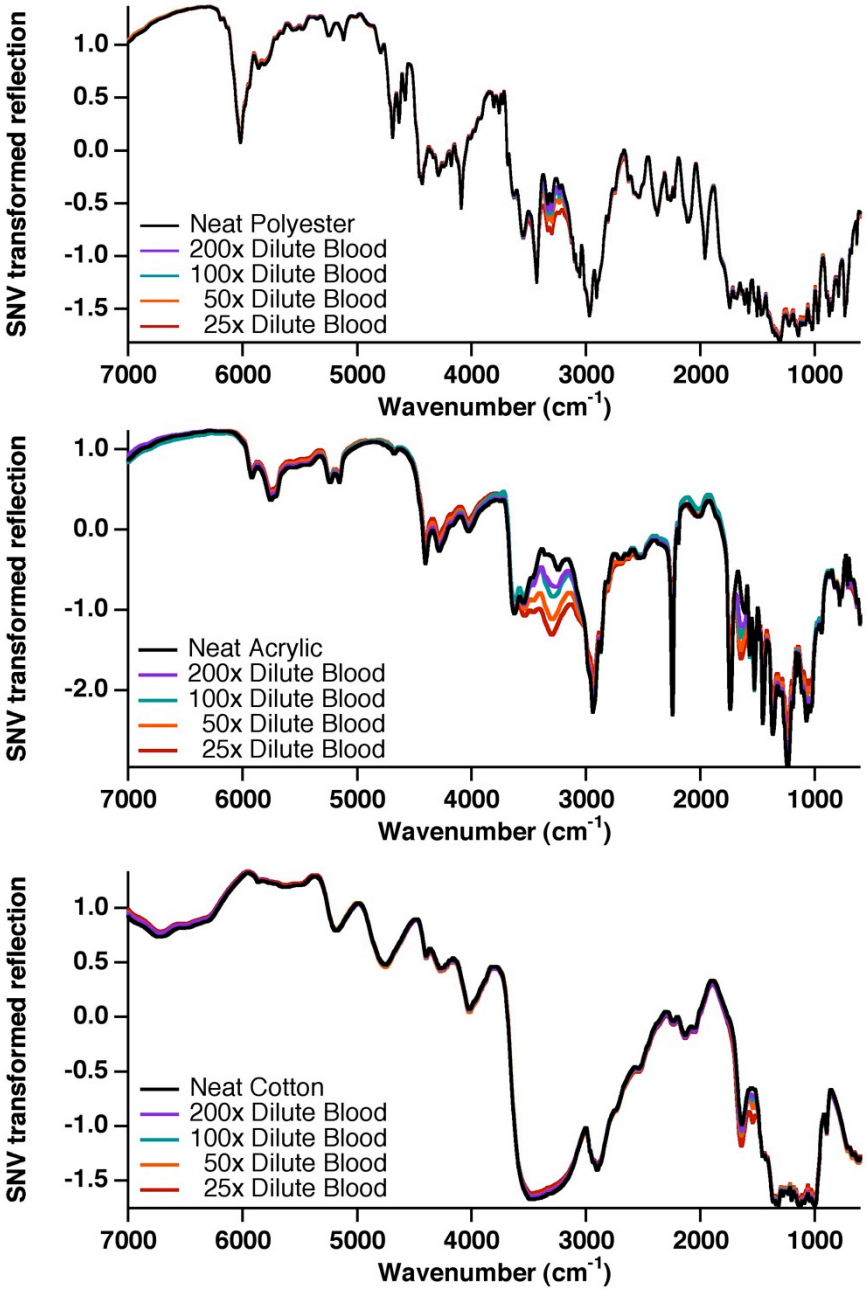

Fig. 3.1: Mean spectra of blood on (a) polyester, (b) acrylic, and (c) cotton fabrics.

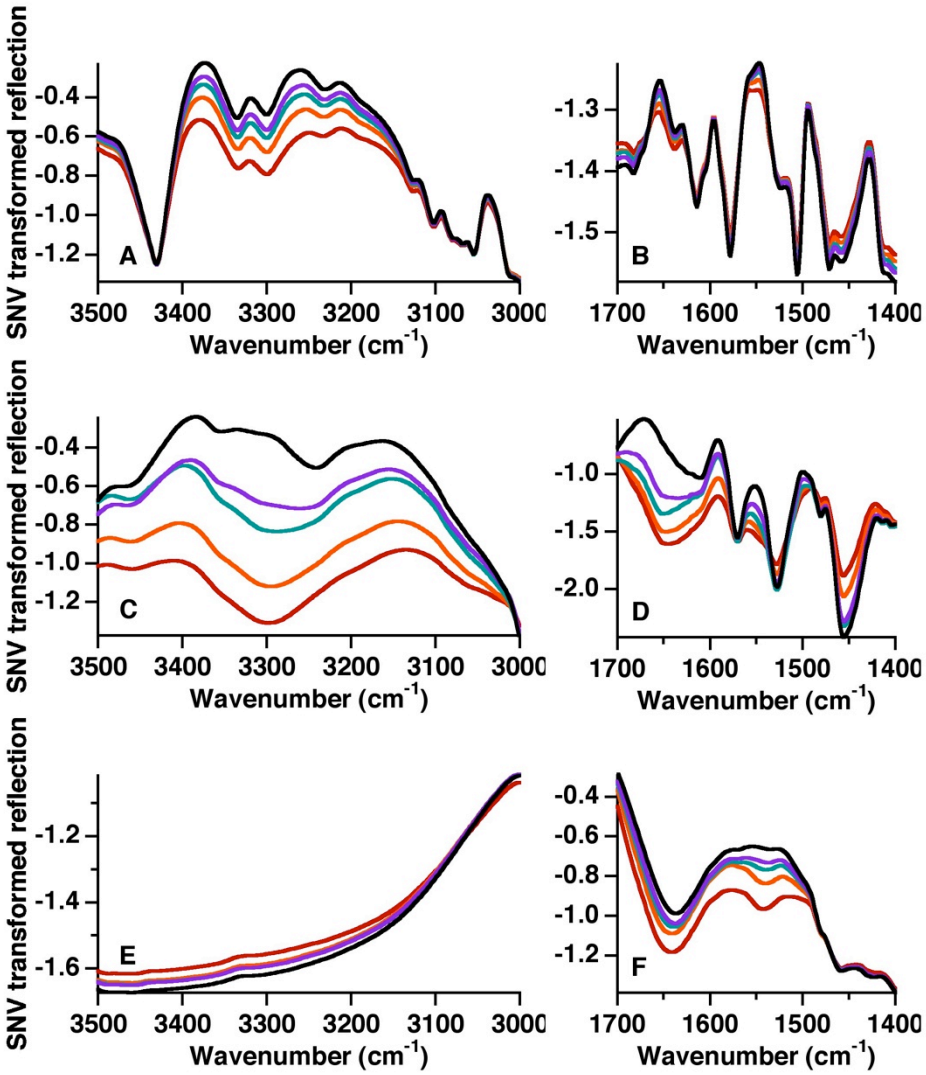

Fig. 3.2: Mean IR diffuse reflection spectra of blood on fabric. The left column shows the Amide A/B region of protein absorbance. The right column shows the Amide I/II region of protein absorbance. Black traces are neat fabric, and lightening color corresponds to 200, 100, 50, and 25x dilute blood on fabric. (a-b) Blood on polyester. (c-d) Blood on acrylic. (e-f) Blood on cotton.

samples that were retained for analysis. Figure 3.3a-c shows the difference between the mean spectra of 25x dilute blood on fabric and neat fabric.

3.2.3. Data Preprocessing We combine derivative preprocessing with SNV preprocessing. First-order derivative processing is often considered a means of removing a baseline offset from spectral data. SNV also removes baseline offset, as well as adjusts the span of the data and corrects multiplicative effects. Because SNV offers the additional benefit of reducing multiplicative effects, the two processing methods perform complementarily with one another. When first derivative processing is applied to spectral data prior to SNV, the effects of any baseline offsets are eliminated, and any curvature in the baseline is also converted into a new baseline offset.[5-6] Thus the combination of differentiation in the n^{th} degree followed by SNV is to remove a polynomial of order n+1 from the original spectral data, as well as to change the weights accorded to spectral features according to their relative shapes and to give a common breadth to the resulting profiles prior to modeling. When working with IR reflectance spectra, the data are often transformed to pseudo-absorbance data by applying a log(1/R) treatment prior to further processing in hopes of linearizing the relationship between spectra and concentration. We investigated whether this pretreatment used in conjunction with SNV and derivative processing would improve our results. While implementing this pretreatment did change the emphasis on certain features shown in Fig. 3.4 (and described later), the log transform did not improve calibration results as a whole because the combination of SNV and derivative treatments effectively removed multiplicative effects in the

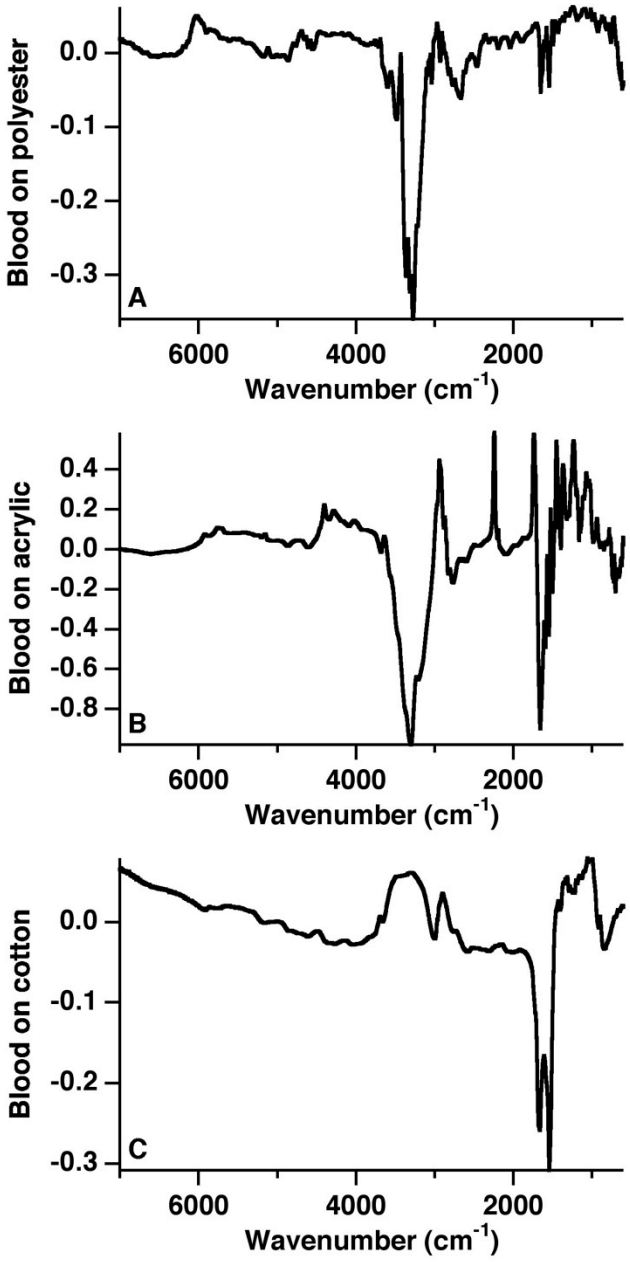

Fig. 3.3: Mean difference spectrum of blood on (a) polyester, (b) acrylic, and (c) cotton fabrics. These spectra show the difference between the mean spectrum of 25x dilute blood on the three fabrics and the mean spectrum of the neat fabric.

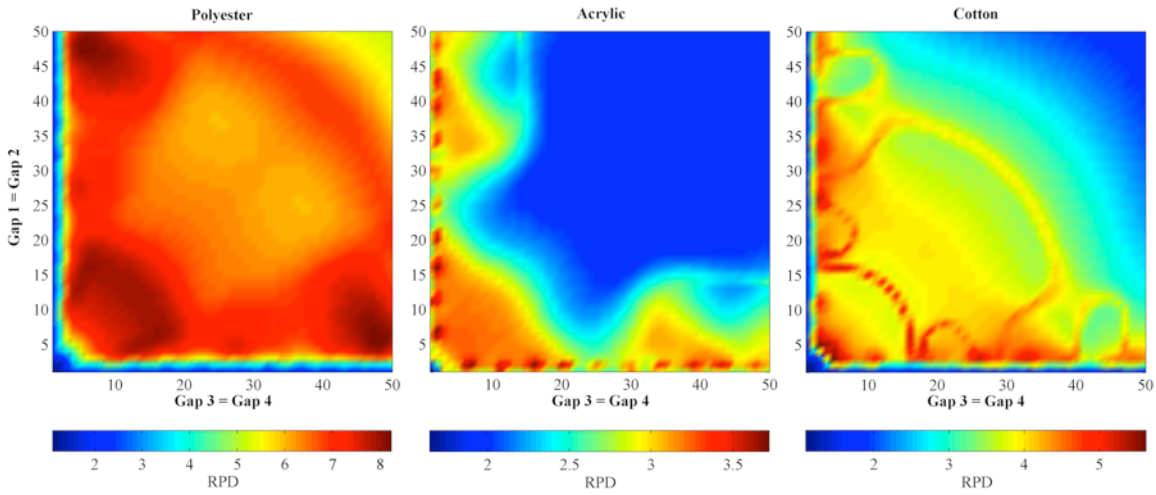

Fig. 3.4: RPDs as a function of 2 different gap sizes. These plots show the RPD of calibration models with GD4 preprocessing for blood on polyester, acrylic, and cotton fabrics as a function of two different gap sizes. The plots show symmetry along the diagonal reinforcing that the order in which gap sizes are used does not influence the GD. **Polyester:** The map shows generally broad features, suggesting a range of gap combinations is equally effective in calibration. **Acrylic:** This map also has broad features, but there is also a distinct beat feature along the axis when the combination of gaps includes a gap of 2. **Cotton:** This map is more interesting, with several distinct arcs and semi-circles with improved calibration performance.

spectra. Accordingly, this transform was not implemented. For SG preprocessing, zero-, first-, second-, and fourth-order derivatives (SG0, SG1, SG2, and SG4, respectively) were taken of quadratic and quartic polynomials. The window frame of the polynomial fit was varied from 5 to 101 (odd values).[7] For GD preprocessing, first-, second-, and fourth-order derivatives (GD1, GD2, and GD4, respectively) were calculated. The gaps for all GD1 calculations were varied from 2 to 50 (even integers). GD2s were calculated by two first derivative iterations with two distinct gaps (even integers from 2 to 50), or with one second derivative iteration with one gap (integers from 2 to 50). GD4s were calculated by four first derivative iterations four distinct gaps (even integers from 2 to 50), or two second-derivative iterations with two gaps (integers from 2 to 50).

In calculating GDs, data points at either end of the spectrum are lost. The number of points lost is equal to one-half the sum of the gaps used. To ensure that the comparison of preprocessing methods was not influenced by these missing points, each derivative spectrum was trimmed to the length of the shortest derivative.

3.2.4. Calibration After derivative preprocessing, data were transformed by SNV and mean-centered prior to PLSR performed using PLS toolbox 6.7.1 (Eigenvector Research Inc., Wenatchee, WA). All spectral points remaining after derivative processing were used in every calibration (793 – 6808 cm^{-1}). Previous results have shown that the mass of solids deposited during dip-coating of a solution is inversely related to the dilution factor of the solution when the deposition is well controlled.[8] Thus, instead of calibrating to the mass of blood

solids deposited, we calibrate the method to the inverse dilution factor of the dipping solution, knowing this is directly proportional to the mass of blood solids on the dried fabrics, although the proportionality constant is different for each fabric depending largely on the exposed surface area of the fibers from which the fabric is made. For a more consistent comparison, the same number of latent variables (LVs) was retained in all models. Two LVs were retained for each model, as two LVs was indicated as the most common optimum number of LVs to be retained by the root-mean-square error of prediction (RMSEP) and the root-mean-square error of cross validation (RMSECV) of the models.

The ratio of the standard deviation of the reference values to the RMSEP of the model (known as the RPD)[9] was calculated for each model as:

$$\text{Eq. 3.1} \qquad \mathrm{RPD} = \sigma_y / \mathrm{RMSEP}$$

The RPD provides a framework to interpret the RMSEP in terms of the model performance in predicting unseen data by assessing model performance against simply predicting the mean value of the validation set for each sample. A threshold RPD of three has been previously suggested as a minimum for adequate model performance and only models performing better than this threshold were retained.[9] Of the remaining models, the calibration model selected was that with the lowest RMSEP.

The model with the overall lowest RMSEP for each fabric was then compared to the model with the lowest RMSEP within each preprocessing group of that fabric. The preprocessing group is the set of all models of a given derivative order calculated by either the SG or GD methods. The errors in each

of these models were compared against the overall lowest RMSEP model to test for significance at 95% confidence, according to the method published by Fearn.[10]

3.3. COMPARISON OF DERIVATIVE PROCESSING METHODS IN INFRARED DIFFUSE REFLECTION SPECTROSCOPY

Derivative processing provides advantages – rejection of baseline offsets, slopes and curvatures, in addition to changing the relative importance of spectral bands – for pretreating diffuse reflection spectra prior to chemometric modeling. The SG and GD approaches to differentiating spectra are computationally distinct. The seemingly implicit noise suppression of SG derivatives make them attractive, particularly for visual inspection. However, as shown in Chapter 2, the reputation that GDs have for generating noisy derivatives is only deserved for small gaps that attempt to preserve the appearance of a true AD. If we allow GDs with larger gaps, noise is suppressed, and can even become lower than that of the original spectrum, without introducing any specific smoothing functions. The question remains whether the two approaches are comparable for modeling data using chemometric methods. In this section, we apply both methods to the measurement of the amount of blood solids on three different types of fabrics, using a brute force approach to comparing and evaluating SG and multiple-gap GD processing of spectroscopic data as an input for the calibration models.

The averaged spectra for the different fabrics shown in Fig. 3.1 and 3.2 illustrate how the different absorption bands of the fabrics affect the appearance of deposited blood solids in diffuse reflection, and these bands are also shown in the difference spectra of Fig. 3.3. The major absorption bands observed in blood

solids are attributable to blood proteins, primarily the Amide I and II bands (near 1650 and 1540 cm^{-1}, respectively), and the broader Amide A and B bands (near 3220-3300 and 3080 cm^{-1}, respectively), as well as some of the weaker protein bands. Both of these features are clearly visible in the spectrum of blood on acrylic, and the Amide A band is particularly prominent (Fig. 3.2c-d, Fig. 3.3b). In this case, Amide A appears with a FWHM of about 92 cm^{-1} (48 points). While the Amide I/II peaks are also visible in the spectra, the matrix spectrum of acrylic also exhibits many features similar in shape and intensity throughout the mid-infrared region. The Amide I band has an apparent FWHM of about 34 cm^{-1} (18 points) and the Amide II band appears about half as wide, with FWHM of 17 cm^{-1} (9 points). Hemoglobin is the dominant protein in blood, and a spectrum of hemoglobin can be found in a protein spectral database at University of Northern Colorado.[11] In the spectral database, the FWHM of hemoglobin's Amide I band is estimated at 34 cm^{-1}, and the Amide II has a comparable width. In our spectra, the Amide II appears narrower because of strong underlying absorption from the fabric. As a result of the strong acrylic absorbance in this region, there is a general increase in reflectance in the mid-infrared that may be attributed to the presence of a coating on the fabric, though it might not be particularly useful in developing calibrations.[8] The Amide A absorbance is also prominent in the spectrum of blood on polyester (Fig. 3.2a-b), though it is not as isolated as it appears in the spectrum of acrylic. Instead of a single, broad band, Fig. 3.3a shows a group of three overlapping peaks in the Amide A region. The central peak at 3318 cm^{-1} can be identified with an estimated FWHM of 13 cm^{-1} (7

points), much narrower than the Amide A band in acrylic. The FWHM of the feature combining the three smaller bands is about 206 cm^{-1} (107 points). While the Amide A is visible even when overlapped with polyester features, polyester strongly absorbs in the same region as the Amide I/II absorbance, rendering the Amide II band just visible upon close inspection and Amide I obscured. In contrast, the strong hydroxyl absorbance of cotton entirely masks the Amide A absorption (Fig. 3.2e-f). The strength of the absorbance in this region leads to an increase in surface reflection at that wavelength region due to the presence of a coating (Fig. 3.3c). The Amide II peak, though, falls in a region of relatively high cotton reflectance and so is clearly visible in this case. The Amide I band, however, is obscured as it is located along a steeply sloping region of the cotton spectrum. Despite this overlap, both the Amide I and Amide II peaks appear strongly in the difference spectrum, both with similar FWHM values of approximately 40 cm^{-1} (20 points), values close to those reported for the spectrum of hemoglobin.

Models were constructed using the procedure described above. The calibration parameters resulting in the lowest RMSEP (highest RPD) of each preprocessing method for blood-coated polyester, acrylic, and cotton fabrics are reported in Tables 3.1 - 3.3, while Fig. 3.5 graphically represents the performances of the best performing models for each derivative order by both SG and GD methods. A black asterisk in Fig. 3.5 indicates the models that do not significantly differ from the best (highest RPD) method. These tables and Fig. 3.5

Table 3.1: Parameters of best calibration for blood on polyester in each preprocessing group.

POLYESTER	DERIVATIVE ORDER	PARAMETERS		RMSEP	RPD
RAW	0			0.00567	2.52
SNV	0			0.00303	4.71
		POLYNOMIAL ORDER	WINDOW SIZE		
SAVITZKY-GOLAY	0	4	9	0.00303	4.71
	1	4	11	0.00179	7.98
	2	2	19	0.00188	7.60
	4	4	37	0.00204	7.00
		GAP SIZES			
GAP DERIVATIVE	1	4		0.00179	7.96
	2	9, 9		0.00189	7.55
		4, 50		0.00177	8.08
	4	6, 6, 48, 48		0.00173	8.24
		4, 6, 46, 50		0.00172	8.28

Table 3.2: Parameters of best calibration for blood on acrylic in each preprocessing group.

ACRYLIC	DERIVATIVE ORDER	PARAMETERS		RMSEP	RPD
RAW	0			0.00824	1.73
SNV	0			0.00637	2.23
		POLYNOMIAL ORDER	WINDOW SIZE		
SAVITZKY-GOLAY	0	2	101	0.00634	2.24
	1	4	5	0.00536	2.65
	2	2	5	0.00429	3.31
	4	4	11	0.00413	3.44
		GAP SIZES			
GAP DERIVATIVE	1	2		0.00550	2.59
	2	2, 2		0.00425	3.35
		2, 6		0.00464	3.06
	4	2, 2, 16, 16		0.00382	3.72
		2, 4, 6, 40		0.00409	3.48

Table 3.3: Parameters of best calibration for blood on cotton in each preprocessing group.

COTTON	DERIVATIVE ORDER	PARAMETERS		RMSEP	RPD
RAW	0			0.01205	1.19
SNV	0			0.01228	1.17
		POLYNOMIAL ORDER	WINDOW SIZE		
SAVITZKY-GOLAY	0	4	5	0.01228	1.17
	1	4	5	0.00390	3.67
	2	2	7	0.00319	4.48
	4	4	21	0.00329	4.35
		GAP SIZES			
GAP DERIVATIVE	1	2		0.00393	3.64
	2	3, 3		0.00313	4.58
		2, 4		0.00301	4.75
	4	3, 3, 5, 5		0.00255	5.61
		2, 4, 10, 32		0.00251	5.71

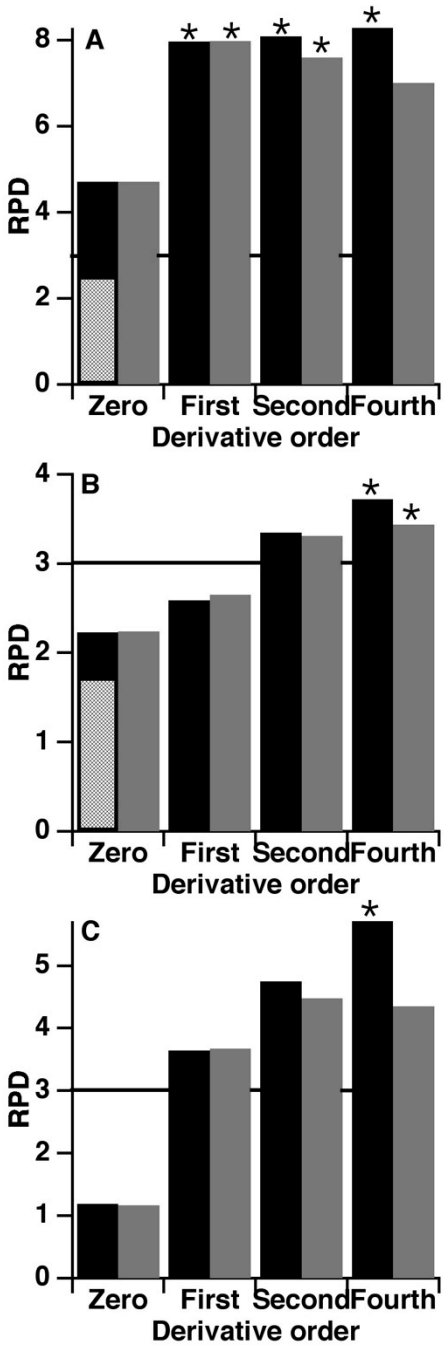

Fig. 3.5: Summary of PLSR Results. This displays the highest RPD of the PLSR models of each preprocessing group. The threshold for an acceptable model (RPD = 3) is marked with a black line. Models not statistically different from the highest RPD model are marked with a black asterisk. Solid black bars represent GDs, dark grey represents SG derivatives, and light grey represents no preprocessing. For all 3 fabrics, GD4 achieves the highest RPD. The three panels correspond to: (a) Polyester Fabric, (b) Acrylic Fabric, and (c) Cotton Fabric.

are discussed here in more detail. In these tables and the rest of the work, gap size will be given in points, where each point is separated by approx. 1.93 cm^{-1}.

3.3.1. Calibration without Derivatives The leftmost bars of Fig. 3.5 represent the result of treatments that do not include derivatives as the baseline case. For all fabrics, calibration based on raw spectra was poor, with no models exceeding a minimum RPD of 3. SNV pretreatment applied to reduce variability in the spectra improved the calibrations of acrylic and polyester, though no improvement was found for cotton. Models of blood solids on polyester improved enough to generate an acceptable calibration without any additional data pretreatment.

No one to our knowledge has described the original spectral data as having the equivalent of a GD0 pretreatment applied to it ahead of calibration, yet there is a connection between the coefficients of the *n*-1 layer of Pascal's triangle and the coefficients of all higher-order GD*n* pretreatments with a single gap. By this analogy, a GD0 pretreatment would use the coefficients of layer 1 of the triangle, i.e., a single coefficient of 1 for each point, and would be divided by unity. Continuing this analogy, a GD0 spectrum would be exactly the same as the original spectrum. The performance of a GD0 model in this case is thus identically the same as that of the models with only SNV pretreatment.

SG0 pretreatment (smoothing) before SNV should, in principal, be better for building models than GD0, since the latter has no effect and the former provides some noise rejection. However, for all three fabrics, SG smoothing of the data prior to SNV pretreatment did not further improve the calibrations

compared to SNV alone. This suggests that any benefit of SG processing in higher-order derivatives for these data results from the derivative step rather than the smoothing of the polynomial fit.

3.3.2. Calibration with First-order Derivatives SG1 and GD1 derivatives applied before SNV improve the calibration for all three fabrics compared to calibrations without derivatives so that models for blood solids on cotton also meet our minimum criterion for acceptable models, in addition to models for polyester which continue to be well above the acceptable limit. This is a striking improvement for the spectral data acquired from cotton samples, since models were essentially unpredictive without differentiation (RPD ~ 1, which is as bad as it gets). As mentioned above, the hydroxyl absorption in cotton almost fully masks the Amide A/B region in the spectra of blood solids, so the major bands observed on cotton are the relatively sharp and easily distinguished Amide I and II. At the same time, all bands of the cotton substrate are relatively broad. This makes it possible for even a first-order derivative approach to significantly enhance the prominence of the Amide I and II features observed for blood on cotton.

For all three fabrics, the GD1 and SG1 approaches achieve almost identical RPDs, and small gap sizes perform best for the GD1, with the calibration worsening as the gap size widens. This suggests that the salient analyte features in the spectral data are narrow enough to encourage the use of small gaps, with a gap of 2 points corresponding to about 4 cm^{-1} spectral width. The preceding theory of gap derivatives suggests that such a small gap would

probably not be selected if the SNR of the original data were not so high (~10^4) because in many cases the spectral bands are noticeably broader than this gap, and gaps smaller than the FWHM tend to diminish the SNR of the spectra. We note that g = 2 points is as close as we can get to the true first derivative with GD processing, so the selection of this minimal gap supports the idea that differentiation itself is the important part of the SG1 pretreatment, as opposed to the smoothing component of the filter.

3.3.3. Calibration with Second-order Derivatives Second derivatives show improved performance over first derivatives in nearly all cases. Likewise, GD preprocessing remains at least the equal of SG at the second derivative level, and exceeds it in some cases. RPDs improve by 30% for GD2 preprocessing of acrylic compared to GD1, so that acrylic finally gives acceptable models by our criterion. RPDs for blood on fabric GD2 models also increase by 30% for cotton and another 2% for polyester fabrics.

The trend is not as obvious for models using SG2: while models improve by 25% and 22% for acrylic and cotton substrate data respectively, RPDs fall by 5% for SG2 models of polyester compared to SG1 models.

The best GD2 models for acrylic and cotton data use small gaps; taken together with the SG2 results, this suggests that it is the additional differentiation itself that yields improved models for these two fabrics. In both cases, the Amide I and II features are easy to see in the raw spectra. Polyester, on the other hand, does not improve with the additional step of differentiation, possibly because the main analyte bands observed on polyester are only the much broader Amide A/B

absorptions. These absorption bands were already prominent in the GD0 and SG0 models, and were the reason that polyester diffuse reflection data yielded acceptable models without differentiation. From this standpoint, it is understandable that increasing levels of pure differentiation might not benefit the modeling process.

While SG2 models for polyester decreased in performance consistent with the preceding statement, models with GD2 preprocessing improved slightly. It seems unlikely this would happen if GD2 preprocessing were simply a noisier version of SG differentiation. Indeed, the best single gap GD2 model that we obtained also performed more poorly by 5% in RPD compared to the best GD1 model, exactly mirroring the behavior of SG2 preprocessing. However, when we evaluated the best models employing two different gaps, we found an improved performance when one gap was very small and the other very large. The best performance for GD2 models for polyester was found with gaps of 4 and 50 points – the latter corresponding to about 97 cm^{-1}. Polyester data are the only data in our study that show this behavior at the GD2 level, but it becomes the rule rather than the exception in higher derivatives for the other fabrics as discussed below. The sudden divergence of GD2 models for polyester from mimicking a true second derivative to something more complicated suggests that a new mechanism for modeling is being invoked. This will be discussed more extensively in the discussion of GD4 processing where increased flexibility in selection of gaps makes this new mechanism the dominant mode by which GD preprocessing improves model performance.

3.3.4. Calibration with Fourth-order Derivatives SG4 calibrations gave very mixed results compared to those using SG1 and SG2. SG4 models for polyester samples were poorer than those using SG2 preprocessing, which in turn were poorer than those using SG1 preprocessing. For this fabric, the Amide A and B bands are the main features engaged in calibration, and the strength and width of those bands account for the relatively high RPDs for polyester samples regardless of the pretreatment. Apparently no true derivative beyond the first is beneficial for modeling blood solids on polyester, and this likely results from the fact that the major variations in the spectra due to the presence of blood on polyester are already prominent in the original spectra and so do not require much enhancement.

Cotton samples showed model RPDs that continued to increase at the SG2 pretreatment level. However, SG4 preprocessing shows no advantages over SG2, and actually yields slightly poorer performance. Cotton spectra showed visible Amide I and Amide II bands, but the large Amide A band is obscured by strong cotton hydroxyl absorption. The Amide I and II are sharper than most of the surrounding cotton bands, and differentiating the spectra allows them to stand out more in models (equivalently, the variance in the spectra due to the Amide I and II analyte bands become more important overall as the level of differentiation increases up to the SG2 level). Going beyond the SG2 level is disadvantageous, even for cotton data with its sharper bands.

Acrylic fabrics provided the only examples in which SG4-based models outperformed SG2, with the RPD increasing by about 4%, compared to a 25%

increase in performance between SG1 and SG2 models. Acrylic fabrics, not coincidentally, yielded the poorest overall calibrations once derivative analysis was begun. Looking at the spectral data, we observe that there is an interfering behavior of the substrate spectra that contributes a great deal of the variance in the spectra, so any pretreatment that works to counter this effect and increase the variance associated with the analyte relative to the substrate is beneficial. Derivative processing allows the spectral features of blood solids to be slightly better distinguished from the substrate in models, and this improvement continues into the fourth derivative level.

GD4 processing shows improvement over GD2 processing for creating models with higher RPDs in every case; GD4 preprocessing combined with SNV is the best pretreatment method for all blood solids data sets in this report. The preceding discussion about SG pretreatments strongly suggests that the benefit of GD4 preprocessing is not to be found solely in the power of derivative processing. Instead, as suggested above for GD2 processing of polyester data, an additional mechanism for supporting models is being invoked that goes beyond simple differentiation. Further, since the trend is still monotonically upward at the GD4 level, it is possible that even better performance might be obtained with larger gap derivative orders, while it is likely that higher-order SG derivative processing will not prove any benefit in this data set.

It is worthwhile to examine what additional mechanism might be offered by GD4 processing (or even higher orders). Figure 3.4 provides a full mapping of the RPD for GD4 models of blood-solids on polyester, acrylic, and cotton,

respectively. To make these presentable in two dimensions, each axis represents a gap for two steps of differentiation, so all the GD4 treatments illustrated in these figures use at most two separate gaps repeated twice each. On the diagonal of the plot, all 4 gaps are identical. Several features of these figures are instructive.

First, these figures show that SNR is not a limiting factor for these data. We show above that there is an improvement in SNR4 on the order of $\sqrt{\frac{70}{16}}$ when multiple gaps are selected compared to a single gap. Yet none of these figures show a clear diagonal line (all gaps the same) of relatively poor RPDs that would suggest the SNR was limiting model performance. The appearance of small gaps in most of the models further supports that the SNR of the original data is not a limiting factor.

Next, while all the models involve blood solids on fabric in approximately the same range of concentrations, the patterns of RPD representing the best models are very different in the three fabric systems tested. The simplest pattern of RPD is that for polyester, where only the broad Amide A/B bands of blood solids are observed well, and where we found the only acceptable modeling of a system with no derivative pretreatment. The features of this RPD map with gaps up to 50 points (97 cm^{-1}) are smoothly varying (The symmetry of this figure – as well as the others – is a trivial consequence of the fact that the GD4 spectrum is independent of the order distinct gaps are employed in "differentiation").

The optimum GD2 treatment for polyester involved a single small and a single large gap (4 and 50 points); the optimum GD4 treatment in which only two

gap sizes are used mirrors the GD2 treatment, with two small and two large gaps being the optimum (6 and 48 points). Despite the fact that this appears to be almost identical to the GD2 set of gaps, it yields a performance that is slightly better (2%) than that of the GD2 model. (We jump ahead of ourselves to note that when four unique gaps can be selected, the optimum in which all four gaps are forced to be different yields a still better model, but the improvement is less than 0.5%. The gaps selected under that restriction still reflect the same pattern of having two small and two large gaps, in the same range as those of the GD2 model).

There are two characteristics of the blood on polyester spectra that we believe cause the RPD map for this fabric to be relatively simple. First, the major bands attributable to blood solids on this fabric are in the Amide A region, which are clearly identifiable to the eye in a cursory review of the data. The Amide A band is very broad and relatively featureless compared to the lower frequency spectral window for blood solids, and appears in a natural minimum in the polyester absorption spectrum. Meanwhile, the Amide I and II bands appear weakly in a very congested portion of the polyester substrate absorption spectrum and require a much closer review to see where they might be (even then, the peaks are weak and indistinct). If we neglect the minor contribution of the Amide I and II bands, the appearance of blood features on polyester is as simple as one is likely to get in any environment: a single band, broad and strong.

The introduction of one or more large gaps in the GD4 preprocessing accomplishes something rather interesting. We take the example of the best GD4 preprocessing of data for blood solids on polyester with two repeated gaps from Fig. 3.4 and look at it in more detail. Recall that a GD best simulates a true derivative when gaps are small and the points being selected for GD calculation are close to one another. From Eq. 2.1 - 2.3, the reader will also recall a pattern of the coefficients for each of the levels of differentiation – a first derivative would have a coefficient pattern of (1,-1), a second derivative would have a coefficient pattern of (1,-2,1), and a fourth would have a coefficient pattern of (1,-4,6,-4,1). The coefficient set is symmetric for even-order derivatives and antisymmetric for odd-order derivatives. When we look at the pattern of coefficients obtained for polyester's best GD4 model with two repeated gaps (two gaps of 6 and two of 48), the pattern we recover is illustrated in Fig. 3.6, overlaid on the polyester spectrum.

This pattern can be described as one that samples a function at three evenly spaced points. Each point of sampling is done with a triplet of narrowly spaced points evaluated with second derivative-like coefficients. The orientation of the three second-derivative functions is not the same: the set of peaks represents a strong sensitivity to a negative curvature at the center of the function, while the two side-bands add together to give the same magnitude of sensitivity to a positive curvature, but separated from the center by 48 points, or about 93 cm^{-1}.

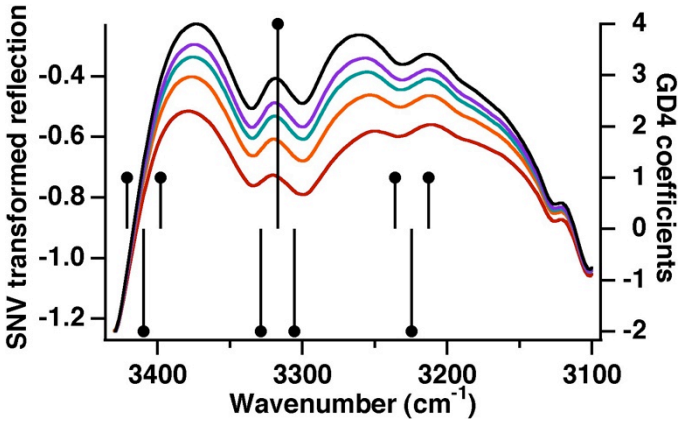

Fig. 3.6: GD4 convolution function plotted with mean spectra of blood on polyester. The convolution function corresponds to the GD4 calibration using two gaps each of 6 and 48, one of the optimal combinations for calibration on polyester. The function comprises three triplets, sampling the curvature of the curvature of the spectra, also known as the fourth derivative. Note how the center and wing triplets are aligned with features of opposite curvature, the sweet spot for these matched filters. The center triplet also shows spacing to match two dips in the spectra on either side of the center peak. The relationship between these three points is closely related to the amount of blood solids present, again pointing to the optimization of gaps as a way of approximating a matched filter.

Looking at the points this way, one can see these as a certain type of approximation to the fourth derivative. Specifically, each of the sets of triplet coefficients samples not the intensity of a peak, but its curvature at the center point of each triplet. The arrangement of double negative sensitivity in the center and single positive sensitivities to the wings is itself in the form of the second derivative. Therefore, this pattern measures the second derivative of the curvature – which is the fourth derivative.

While this explanation may be true, it is silent on the interpretation of the polyester RPD map. If a fourth derivative of the Amide A band were critical to enhancing the relative spectral variance explained by blood solids on polyester, then the basic (1,-4,6,-4,1) pattern obtainable with 4 identical gaps would do the same job. A single gap size of 24 points repeated 4 times would span the same spectral width and give as good an approximation of the fourth derivative – but a glance at the RPD map for polyester shows this results in a much poorer RPD.

Another way of looking at these coefficients is that each of the wavelength triplets in Fig. 3.6 represents a sensor for the curvature of a section of the original spectrum, rather than strictly an approximation for the fourth derivative of the original spectrum. The central large triplet represents a strong sensitivity to the curvature at the point in the spectrum where the calculation is being carried out. The others represent sensitivities to curvature in the opposite direction approximately 93 cm^{-1} to the left and right of the point of the calculation in the optical spectrum.

This interpretation makes sense in the context of pattern recognition. A spectral band has a shape associated with it; if a spectral band is different in shape for the analyte than the matrix, a convolution function that is able to recognize that shape would allow it to be pulled out of the background more effectively and allow the variance associated with the spectral feature to become more prominent in the higher LVs, thus leading to a better calibration and improved RPD. To visualize this effect, the positions and coefficients for the best GD4 pretreatment is shown centered on the Amide A band center (at 3318 cm^{-1}) of polyester in Fig. 3.6. Because of the contribution of substrate bands, the Amide A contribution to the overall spectrum is not symmetric and definitely not simple. The central triplet has a span appropriate to emphasize the curvature of that central point; the sampling location of the wings with sign opposite to the center line up with the regions of the spectrum with opposite curvature on either side of the central increase in reflectance at 3318 cm^{-1}. By sampling the curvature at this point, the GD4 function is sensitive to the change in relative reflectance of either side of the central point, a feature that changes greatly with the presence of blood. As noted above (related to Fig. 3.3a), the FWHM of the feature at 3318 cm^{-1} is about 7 points, a value consistent with the gap size associated with the center triplet. The outside triplets sample curvature to either side of the central triplet and are sensitive to curvature in the opposite direction. The location of each of these triplets appears in a point of the spectrum with more positive curvature, in contrast to the negative curvature of the central peak, increasing the strength of the derivative at the central point. As mentioned above,

the coefficients for a GD4 calculation are constrained to be symmetric with respect to reflection, so the skew of the Amide A band cannot be accurately modeled. The wing triplet coefficients are located in an “average best” position in this sense rather than at the location that would be best if they could be optimized separately.

Others have previously noted the relationship between GD calculation and a convolution operation.[12-14] While this is true, it is only part of the story; another part is that one major purpose of convolution is its use as a tool for recognizing patterns in noisy data, and that one of the early and important concepts in the area of target recognition was the concept of matched filtering.[15-18] Matched filters are typically designed to maximize SNR in signal processing applications where a known signal is to be detected, particularly in the presence of white noise. A matched filter can be implemented as a cross-correlation of a target signal with a waveform that contains the reference target signal along with additive noise.[15-18] It can also be implemented in multi-signal settings, where the optimization is aimed at differentiating two signals from one another in the presence of noise, rather than simply optimizing SNR in the presence of white noise.[18]

In the present circumstance we are concerned with recognizing the “signal” of a blood solids absorption band in the presence of competing signals of the matrix absorption bands, or maximizing the difference between spectra of bloody fabrics and neat fabrics as a binary signal problem. Extending our understanding of GDs in the context of pattern recognition, we can understand

the pattern of coefficients generated by the optimal GD4 preprocessing as the optimal matched filter for enhancing the appearance of target analyte bands that can be achieved within the constraints of a GD4 calculation. Again examining Fig. 3.6, notice that the coefficients of the best model with two repeated gaps takes on the character of the Amide A target second derivative band in the polyester spectrum. We know from attempts to reintegrate the regression vector for the best blood solids on polyester models that the Amide A band is very nearly isolated as a major feature in the regression. When the optimum GD4 is calculated for the difference spectrum between the spectra of the highest and lowest concentrations of blood solids, the strongest negative signal in the derivative is registered with the wavenumber alignment shown in Fig. 3.6, with the most positive signal being immediately adjacent and at slightly lower wavenumber where peaks and valleys in the difference spectrum are reversed. In this new matched filtering view of GD4 preprocessing, we are calculating a moving window cross-correlation between a target part of a spectrum with the full spectrum, using an approach that enhances the signal of the target band relative to the surrounding absorption bands.

To summarize, SG and GD processing, though both based on derivatives, may also operate by different mechanisms. SG processing is intended to mimic a true AD, compensating for noise by simultaneously smoothing noisy numerical data. GD processing may have originated from the same idea of creating a derivative, but its calculation of the derivative is one that permits more flexibility; because larger gaps yield GDs that lose their resemblance to an AD, the

selection of gaps affects more than just the noise in a derivative. Higher-order GD processing offers the opportunity to change the relative importance of bands with differing FWHM values, shapes, and spectral environments through the creation of convolution functions that are flexible enough to imitate a matched filter more closely than anything offered by SG processing. GD processing thus has less to do with differentiation than with filtering, and the improving performance with derivative order results more from the opportunity to refine a filter for a particular spectral pattern than it does to simply emphasize sharp versus broad spectral features. GD processing is more limited than general filtering, due to the restrictions characteristic of GD functions: the values of the filter at each channel are restricted to integers, the absolute values of the filter values must sum to 2^n, the filter must be symmetric, and even in fourth-order functions no more than 16 specific channels are involved in the filter.

Acrylic presents a more complicated RPD map than polyester, though less complex than cotton. The spectra of blood solids on acrylic show prominent features for both the Amide A/B and the Amide I/II regions. The RPD map for acrylic shows an underlying smooth variation that is reminiscent of that seen for polyester. We attribute this broad underlying structure to the ability of some GD4 preprocessing to match portions of the major absorption bands of blood solids in the presence of the matrix acrylic bands. The unusual new feature observed in the map of RPDs for acrylic is a repeating pattern of RPD peaks representing GD4 models with two narrow gaps of 2 points, and a range of repeated larger

gaps: 7, 11, 16, 20, 25, 30, 34, 39, 43, and 48 points, and presumably continuing on beyond 50 points.

These are not simply artifacts in which PLS is modeling noise; RPD is a good tool for identifying artifacts of this type. Nor are the optima single-condition aberrations – they extend over neighboring conditions and are repeated. In addition, we know that the regression vectors for these models are sampling real variance in the data by the locations and peak positions of the regression maxima. However, the simplicity of a GD does not allow it to produce a repeating pattern in the RPD map unless there is something repetitive in the data on which it acts.

The origin of the repeating pattern in the acrylic RPD map lies in a subtle repeating systematic pattern in the original data with a period of about 4-5 data points. Close inspection of the original spectra shows an oscillation in the NIR region of all the acrylic spectra that is so minor it is not easily observable in the spectra, even on close inspection unless the spectrum is expanded greatly and the observer is alert to its potential presence (see Fig. 3.1). Once we understood the origin of this feature, we reviewed the data for polyester and cotton and observed the same pattern in the NIR spectral region in each. As we show below, this gives rise to a repeating pattern in cotton, but the pattern is not as obvious in the RPD map for polyester – perhaps because the polyester models already exhibit good RPDs.

One way to think about the appearance of the repeating pattern in the acrylic RPD map is that two small gaps of 2 points produce a sensor for

curvature with a spacing of 4 units that almost exactly matches the width of a single cycle of the repeating baseline oscillation. The double large gap added on top of this curvature sensor produces three copies of the curvature sensor with spacing equal to the large gap between them, but with the two outer curvature sensors having signs opposite from that of the central sensor of the three. For example, a double large gap of 16 would place the three small curvature sensor groupings at a distance of 16 data points from one another, with the center grouping having the opposite sign of the outer two. Resonances occur where the three curvature sensors fit into the repeating baseline pattern like a lock-and-key. For a repeat length of 4-5 points, this would occur when the large gap equals a half-integral number of cycles of the repeating noise. Since 16 points is the most optimum double large gap in our data set we can estimate a repeat period of 3.6 points; we would then expect resonances at large gaps of 2.3, 6.9, 11.5, 16, 20.7, 25, 29.7, 34.3, 38.8, 43.4 and 48 points – which is exactly where we do observe them, within the limits of our ability to determine, except for the predicted resonance at 2 units, where the picture of the G4 group of points as three separate curvature sensors becomes invalid (since it becomes exactly a fourth derivative at a point).

A repeating oscillation in an FTIR spectrum originates from a spike in the original interferogram from which the spectrum is acquired, either in the background or the spectral collection, or both. Both are believed to be the case here, and as we show below there is a similar feature in the cotton spectra. To have such a high frequency, the noise spike in the interferogram must occur near

the end of the travel of the moving mirror. The fact that it appears fairly reproducibly in our spectra suggests that it is somehow tied to the position at which the mirror reverses, possibly an electronic or mechanical defect caused by a change in the acceleration of the mirror. This repetitive pattern would not have been noticed but for the mapping of the GD4 pretreatment by RPD.

When the higher-energy NIR region that contains most of the noise (Fig. 3.7) is deleted from the spectrum, the RPD map looks nearly identical – except that the oscillation and resonance pattern is completely gone. Unfortunately, the RPDs along the same portion of the map are intermediate between the best and worst RPDs found when the noise is retained. In other words, deleting the noise also eliminates the best calibrations we originally found.

We believe the repeating baseline pattern affects our calibrations by anchoring the SNV preprocessing step. Figure 3.7 shows derivative spectra with different gaps all obtained from the same spectrum. The black traces of this figure show the GD4 spectra corresponding to gaps with “low” RPDs along the line of the resonance for acrylic. The grey traces show the GD4 spectra for large gaps corresponding to the “high” RPDs along the line of resonance. Both sets of spectra use the same repeated small gap of 2 points. The surprise here is that the spectra for which conditions exaggerate the baseline oscillation – grey traces – are those that result in the best spectral calibration for blood solids on acrylic.

Why should an instrument artifact do anything to improve a calibration? Essentially, in this case it acts as a kind of internal standard. The SNV transformation works best when the analyte contribution to the variance of the

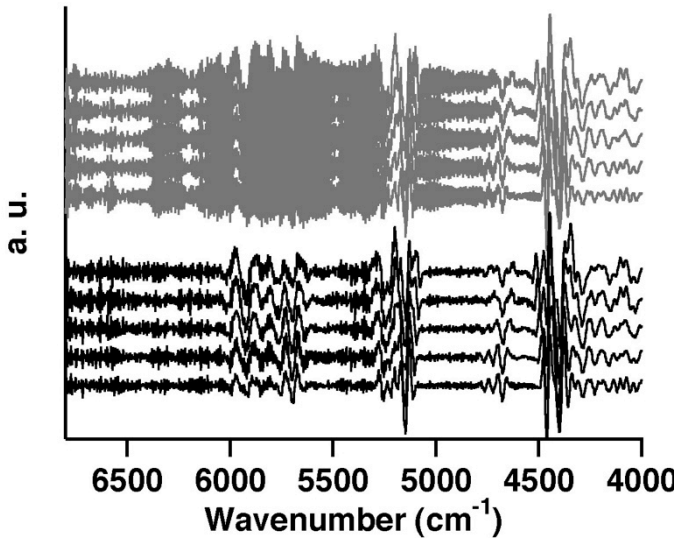

Fig. 3.7: Derivatives of Neat Acrylic. This shows the average derivative of the spectra of neat acrylic fabric using the gaps that are included in the beat pattern of the RPD map (see Fig. 3.4). All the spectra are on the same scale and have been offset for clarity. The grey spectra show derivatives corresponding to RPD peaks: gaps = 2 and 7, 11, 16, 20, 25. The black spectra show derivatives corresponding to RPD valleys: gaps = 2 and 9, 13, 18, 23, 27. The grey traces appear to have higher noise levels, yet consistently perform much better than the gaps corresponding to the RPD valleys.

spectrum is relatively small.[3,19] The presence of a large, analyte-independent contribution to the spectrum improves linearity in the SNV normalization of the analyte. This results in the unanticipated effect of giving better RPDs when the pattern is emphasized and poorer RPDs when it is minimized.

Turning to the RPD map for cotton, we see an underlying broad pattern that is reminiscent of the broad underlying behavior of the polyester and acrylic RPD maps. We also observe a repeating pattern of maxima similar to those just described. This pattern is eliminated upon exclusion of the NIR spectral region, so we attribute it to the same origin. The other unique features of cotton remain, suggesting a different source for those patterns. The cotton RPD map presents a complex series of narrow features that are not repetitive, but are systematic: semicircular and linear features that connect but do not appear to cross one another.

Using the outer ring of the RPD map (the feature extending in an arc from the central point of four gaps of 30 points in Fig. 3.4b) as an example, we investigated the potential sources of this feature. We noted that the calibrations on the feature are consistently more linear than the calibrations using gaps falling on either side of the feature. This suggests that the specific range of gaps falling along the curve compensate for non-linearity inherent for a strong absorbance, such as that of Amide II. Further, the features are only apparent when two LVs are retained in the calibration. Models developed with one or three LVs are relatively featureless. This connects the improved performance to something unique in the second LV for the models connected to those gap sizes. This idea

is further enforced as the first LV for on- and off-feature models are all quite similar, as are the y-block weights associated with LV1. The y-block weights associated with LV2 for off-feature models are very similar, but they are greater for on-feature models, meaning that LV2 contributes more to the final calibration model in these instances.

Upon examination of the second LVs for on- and off-feature models (Fig. 3.8), we noticed that the LVs associated with models that incorporate gaps falling inside the outer ring all appear very similar to one another (blue traces), as do the LVs for models based on gaps falling outside the outer ring (red traces). Furthermore, these two sets of off-feature LV2s are of opposite sign from one another in this region though the shape and location of the features are almost identical. The on-feature LV2s do not have this same consistency (black traces). Rather, this set of LV2s show a range of behaviors, traversing from a shape similar to the LV2s associated with gaps outside the outer ring, to intermediate values, to a shape similar to LV2s associated with gaps immediately inside the outer ring. This behavior is consistent throughout the spectral range. There is one location, however, where the on-feature LV2 deviates from both the above- and below-features LV2s: the region from about 1560 to 1600 cm^{-1}. This corresponds to the region of the spectrum where the substrate spectrum is transitioning from a region of lower to higher absorbance (Fig. 3.2f). This is also a point about half-way between the Amide I and II absorbances of blood proteins. In the difference spectrum of blood on cotton (Fig. 3.3c), the Amide I and II peaks show up as bands on either side of the wavelength region noted above, each

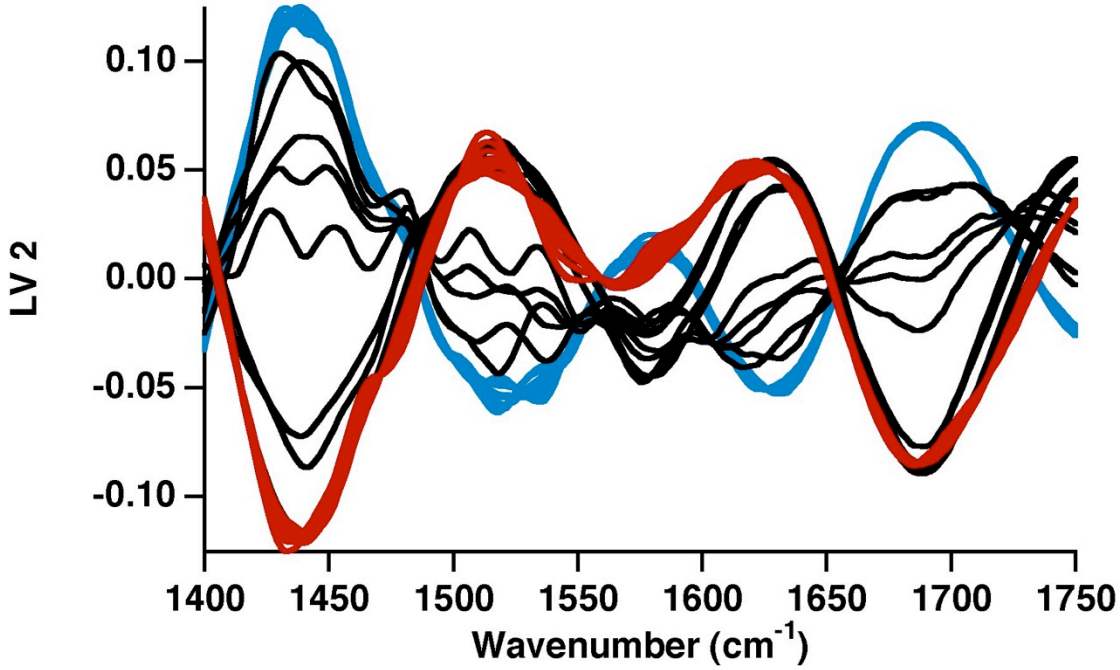

Fig. 3.8: Second latent variable for on- and off-feature models of blood on cotton fabric. The blue traces correspond to gap combinations just inside the outer ring visible in Fig. 3.4, and the red traces correspond to gap combinations just outside the outer ring. The black traces correspond to models corresponding to the gap combinations along the outer ring.

about 30 points away. These peaks are far from symmetric and behave very non-linearly with respect to blood concentration because Amide II is such a strong peak and Amide I is so masked by the cotton spectrum. Here we see another case where the GD4 function is behaving as a matched filter, this time recognizing and fitting to the relationship between two neighboring peaks. All the GD4 functions on the outer ring feature of Fig. 3.4 share this characteristic. The GD coefficients are shown with this region of the difference spectrum for cotton in Fig. 3.9.

In PLSR, the first LV is based on the covariance between the X and Y data blocks, in this case the input spectra matrix and the dilution factor vector, respectively.[20] In cases where the gap sizes implemented provide a better filter to enhance blood features relative to cotton features, the covariance between X and Y is strengthened, leading to a covariance vector with greater length. Because variance not related to the analyte concentration in the data is reduced, the first LV is better able to model the covariance. Conversely, the greater variance accounted for by LV1 means less variance remains for PLS to model (in other words, the length of the remaining covariance is minimized). Again, less non-analyte-related covariance allows the first and second LVs to model important, though subtle, features. Looking along the diagonal of the cotton RPD map (Fig. 3.4, four replicate gaps; diagonal trace is shown in Fig. 3.10), the distance between LV1 and the covariance is minimized at the same gap combinations where the RPD is maximized (Fig. 3.10, blue trace). These particular gaps allow for the situation described above.

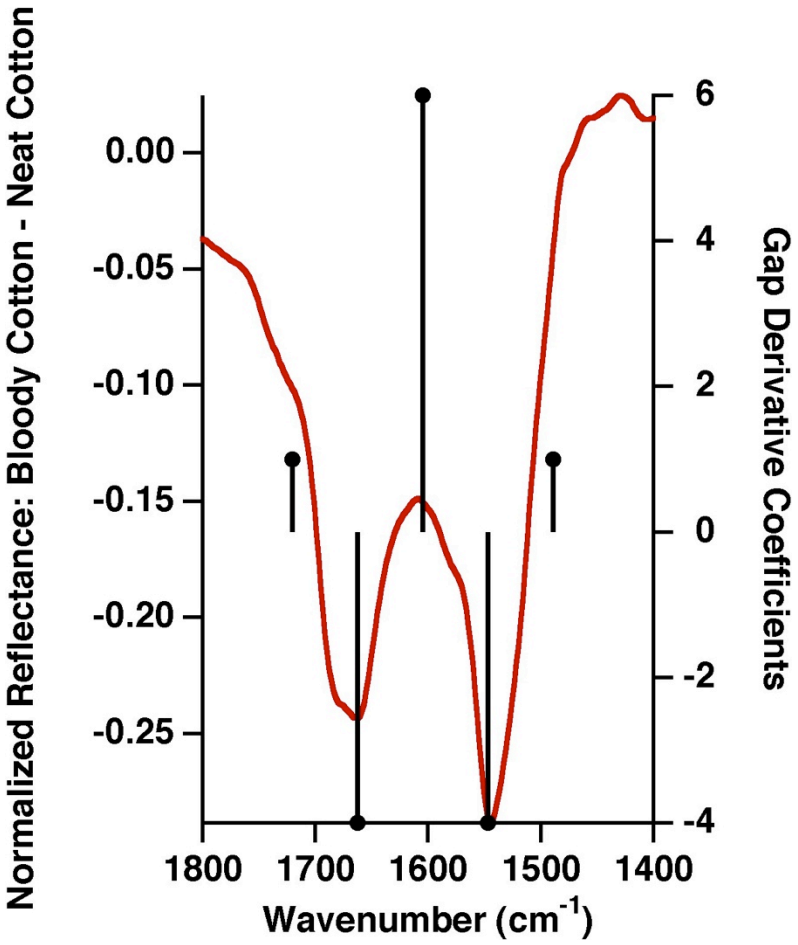

Fig. 3.9: Difference spectrum of blood on cotton fabric in the Amide I/II region of the infrared spectrum. The GD coefficients (black lines, right axis) are for a GD4 function with g = 30.

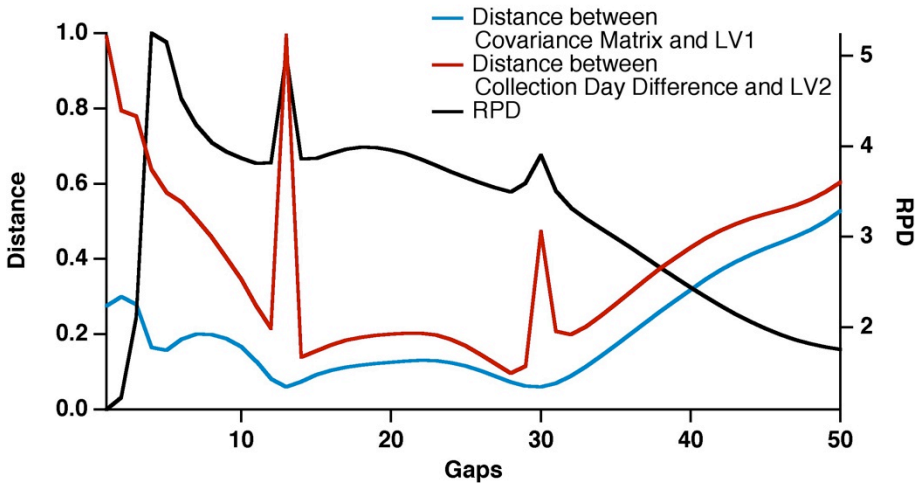

Fig. 3.10: Calibration metrics for models with gap combinations along the diagonal of Fig. 3.4c. The RPD is shown in black and reported on the right axis. The left axis shows the distance between LV1 and the blood component spectrum shown in Fig. 3.3c (blue) and the distance between LV2 and the difference between spectra collected on day 4 and day 1 (red). A distance of 1 indicates little overlap, while a distance of 0 indicates similarity.

In addition to this, as the first LV for all these models accounts for most of the variance, much of the remaining variance is due to artifacts, such as instrument variation. While the experiment was designed to minimize the influence these artifacts might have on calibration, the sensitivity inherent to GD4 processing can wrongly emphasize even these small features, leading to poor calibrations. The second LV for the models along the outer ring, particularly outside and inside the ring, resemble the difference between sample collection days for the highest concentration of blood. In fact, the scores on LV2 tend to separate collection days for those outside- and inside-feature models, though this effect is much less prominent for on-feature models. To evaluate this, the distance between LV2 and the difference between first and fourth collection day spectra of the bloody fabric was calculated. The distance between LV2 and the difference spectrum increases at each of the gap combinations where the RPD also increases (Fig. 3.10, red trace). This means that the models developed with these gaps have less relationship to the instrument variation in the data and so create models with more predictive ability.

Though this discussion has focused on the behavior of the outer ring as an example, it holds true for other features, particularly the inner ring using gaps about half the size of the outer ring. This is evident by the appearance of similar features in two distinct places along the diagonal plot, with gaps of 13 and gaps of 30. In fact, if these distances are displayed in a map similar to that in Fig. 3.4, the same features appear: there are sharp decreases in the distance between the covariance of X with Y and LV1 and sharp increases in the distance between

days and LV2 in all the places Fig. 3.4 shows a sharp increase in RPD. In this way, a variety of gap combinations can enable the same elevation of subtle features into earlier LVs, improving model performance rather dramatically in narrow regions of the maps.

3.4. CONCLUSIONS

We have discussed the optimization of GDs for calibration performance of blood concentration on polyester, acrylic, and cotton fabrics. Zero-, first-, second-, and fourth-order GDs and SG derivatives were optimized and used in combination with the SNV transform as preprocessing for PLSR. We have shown that GDs do not necessarily result in unacceptable SNR degradation, and can even improve SNR when multiple gaps are used in fourth-order GD calculations. Because of this, the smoothing inherent to SG derivatives does not always offer an advantage, and the comparable performance between SG derivatives and GDs at lower derivative orders substantiates that the more important function of SG derivatives is the differentiation rather than the smoothing. At higher derivative orders, the results of SG derivatives and GDs began to diverge, with higher-order GDs continuing to improve in performance while SG derivatives did not follow this trend. Upon investigation, we noted that the fourth-order GD convolution function began to resemble matched filters common to digital signal processing, at least as far as is possible under the constraints of the fourth-order GD function. The optimized fourth-order GD function matched the spectral features of interest, in this case the difference between the spectrum of blood on fabric and the spectrum of neat fabric. Optimized GD preprocessing is a powerful

tool to highlight subtle spectral features and in some situations can result in a significantly better calibration model than its SG analog.

REFERENCES

(1) A. Savitzky, M. J. E. Golay. "Smoothing and Differentiation of Data by Simplified Least Squares Procedures". Anal. Chem. 1964. 36(8): 1627-1639.

(2) J. Steinier, Y. Termonia, J. Deltour. "Smoothing and Differentiation of Data by Simplified Least Square Procedure". Anal. Chem. 1972. 44(11): 1906-1909.

(3) R. J. Barnes, M. S. Dhanoa, S. J. Lister. "Standard Normal Variate Transformation and De-Trending of Near-Infrared Diffuse Reflectance Spectra". Appl. Spectrosc. 1989. 43(5): 772-777.

(4) P. J. Gemperline, J. H. Kalivas. "Sampling Theory, Distribution Functions, and the Multivariate Normal Distribution". In: P. J. Gemperline, editor. Practical Guide to Chemometrics. New York: Taylor & Francis, 2006. 2nd ed. Ch. 3, Pp. 41-67.

(5) T. Fearn. "Are two pretreatments better than one?". NIR news. 2003. 14(6): 9-11.

(6) T. Fearn. "The interaction between standard normal variate and derivatives". NIR news. 2008. 19(7): 16-17.

(7) B. Zimmermann, A. Kohler. "Optimizing Savitzky-Golay Parameters for Improving Spectral Resolution and Quantification in Infrared Spectroscopy". Appl. Spectrosc. 2013. 67(8): 892-902.

(8) M. R. Pearl, H. Brooke, J. N. McCutcheon, S. L. Morgan, M. L. Myrick. "Coating Effects on Mid-Infrared Reflection Spectra of Fabrics". Appl. Spectrosc. 2011. 65(8): 876-884.

(9) P. C. Williams. "Implementation of Near-Infrared Technology". In: P. C. Williams, K. H. Norris, editors. Near-Infrared Technology in the Agricultural and Food Industries. St. Paul, USA: American Association of Cereal Chemists, 2001. 2nd ed. Ch. 8, Pp. 145-170.

(10) T. Fearn. "Comparing standard deviations". NIR news. 1996. 7(5): 5-6.

(11) A. Dong, J. F. Carpenter, W. S. Caughey. University of Northern Colorado. “Protein Infrared Database”. Page last updated Oct 26 2005.

http://www.unco.edu/nhs/chemistry/faculty/dong/irdata.htm [accessed Nov 20 2014].

(12) W. L. Butler. "Fourth Derivative Spectra". Methods Enzymol. 1979. 56: 501-515.

(13) W. L. Butler, D. W. Hopkins. "Analysis of Fourth Derivative Spectra". Photochem. Photobiol. 1970. 12(6): 451-456.

(14) D. W. Hopkins. "What is a Norris derivative?". NIR news. 2001. 12(3): 3-5.

(15) D. O. North. "An Analysis of Factors Which Determine Signal Noise Discrimination in Pulsed-Carrier Systems". Proc. IEEE. 1963. 51(7): 1016-1027.

(16) G. L. Turin. "An Introduction to Matched-Filters". IEEE Trans. Inf. Theory. 1960. 6(3): 311-329.

(17) B. Sklar. "Baseband Demodulation/Detection". In: B. Sklar, editor. Digital Communications: Fundamentals and Applications. Upper Saddle River: Prentice Hall, 2001. 2nd ed. Pp. 122-136.

(18) B. V. K. V. Kumar, L. Hassebrook. "Performance Measures for Correlation Filters". Appl. Opt. 1990, 29(20): 2997-3006.

(19) Q. Guo, W. Wu, D. L. Massart. "The robust normal variate transform for pattern recognition with near-infrared data". Anal. Chim. Acta. 1999. 382(1-2): 87-103.

(20) S. de Jong. "SIMPLS: An Alternative Approach to Partial Least-Squares Regression". Chemom. Intell. Lab. Syst. 1993. 18(3): 251-263.

CHAPTER 4

REVERSIBLE GAP DERIVATIVES AND THEIR INTEGRATION

4.1. INTRODUCTION

Chapters 2 – 3 discussed the ability of derivative transforms of spectral data, such as the gap derivative (GD) transform, to enhance multivariate calibration performance. Those chapters noted the importance of proper gap size selection to highlight the features of interest, particularly as GDs computed with larger gap sizes no longer resemble the analytical derivative. Instead, certain cases show that higher-order GDs behave as a type of matched filter. The matched filter behavior relies on an implicit characteristic of GDs: each derivative point holds information about the relationship between the points in the spectrum from which the GD is obtained. While this characteristic can aid calibration, it also complicates the interpretation of both derivatives and the calibration models developed from derivative transformed data. As the derivative order increases, so does the complexity of the spectrum, with $n + 1$ peaks for every peak in the original spectrum. Each of these peaks is also convolved with the points near it, meaning that higher-order derivatives can have regions of densely packed peaks that are difficult to identify and interpret.[1]

As the spectra passed to a chemometric model such as partial least-squares regression (PLSR) increase in apparent complication, the latent variables (LVs) and regression vectors (RVs) that are developed from those

spectra also increase in apparent complication. To enable interpretation of the models and ensure reliability of the calibrations, it is helpful to look at the RVs in the original spectral space. This domain is more familiar to practitioners, and looking at the derivative RV in zero-order (spectral) space can reinforce the relationship between the original collected data and the calibration model, aiding interpretation of the model and thus understanding of the system under study.

The interpretation of the GD transform performance as a matched filter to enhance calibration was largely based on the integration of the PLSR RVs, though the integration method was not described. This chapter presents a method for integrating GD spectra and the associated RVs. First, a revised method of determining the GD that facilitates integration is detailed. Second, a method for integrating this reversible gap derivative (RGD) is reported. There are several possible methods for defining and integrating the RGD; the algorithm described in this chapter is one that worked in all cases we tested. Calibration performance is then compared between conventional GDs and RGDs as applied to the infrared diffuse reflection spectra of blood on the surface of cotton fabric, one of the data sets discussed in Chapter 3. The integration routine is then applied to both the derivative spectra and the corresponding LVs and RVs. The usefulness of integrated PLSR vectors to discuss model performance is discussed using these examples.

4.2. ALGORITHM

4.2.1. Reversible Gap Derivative Equation 4.1 shows the form of a numerical gap derivative calculated by one of the more common methods, which

approaches a true analytical derivative of a function as the size of the gap *g* approaches 0:

$$\text{Eq. 4.1} \qquad f'(x_i) = \frac{f\left(x_{i+\frac{g}{2}}\right) - f\left(x_{i-\frac{g}{2}}\right)}{g}, \frac{g}{2} < i \leq k - \frac{g}{2}$$

where *g* is a positive, even whole number, and *k* is the number of points in the original spectrum (See Eq. 2.1).[2] To integrate this GD, one might begin by thinking of the integral as a summation of the differentials. However, the GD presents a few complications to this approach. First, the derivative has fewer elements than the original spectrum, thus some values of the integral must be assumed prior to integration. Second, the distance between points used in the calculation of the GD is determined by *g*, so summation must be performed only between points separated by distance *g.* This results in *g* independent vectors contributing to the integral, and each of these vectors is offset from the true value by some arbitrary constant, or the difference between the true first value and that value assumed prior to integration. We sought to develop a method of GD-type differentiation that retained the benefits of GDs while resulting in a derivative that could be integrated exactly.

Integrating GDs requires that three conditions be satisfied. The first of these is that the GDs should have the same number of data points as the original spectrum or spectral region to be used for calibration. The second is that the numerical integration should relate all integral points to a single unknown reference value rather than multiple independent reference values. The third requirement is that the original spectrum and any pretreatments applied to it be

defined so that the single unknown reference value can be assumed to have a specific value (e.g., zero) during integration.

The first condition for a reversible gap derivative (RGD) is that the "derivative" retain the same number of data points as the original spectrum. Our process for achieving this is to define derivative values for the first and last *g*/2 points that would ordinarily be lost by increasing the effective gap size from 1 to *g* at the derivative ends. The first point is defined by

$$\text{Eq. 4.2} \qquad f'(x_1) = \frac{f(x_2) - f(x_1)}{g}$$

For points 2 to *g*/2 − 1, the derivative values are defined as

$$\text{Eq. 4.3} \qquad f'(x_i) = \frac{f(x_{2i-1}) - f(x_1)}{g},\ 2 \leq i \leq \frac{g}{2}$$

The denominator *g* remains constant to prevent the noise amplification that occurs when small gap sizes (i. e., 1) are used. [2]

From this point until the point *g*/2 from the end of the spectrum, the RGD is calculated by Eq. 4.1.

The final derivative values are tapered toward zero as they were at the beginning of the derivative (Eq. 4.4 – 4.5):

$$\text{Eq. 4.4} \qquad f'(x_i) = \frac{f(x_k) - f(x_{2i-k})}{g}, k - \frac{g}{2} < i \leq k - 1$$

$$\text{Eq. 4.5} \qquad f'(x_k) = \frac{f(x_k) - f(x_{k-1})}{g}$$

The RGD retains the character of the gap derivative over most of the spectrum, and the points at either end of the derivative are now treated in a well-defined way that enables integration. This calculation of a derivative vector is demonstrated in Table 4.1 for a 12-point vector $f(x)$ with values x_1-x_{12}, as shown

Table 4.1: Example of differentiation and integration for 12-point vector with gap = 4.

f(x)	f′(x)	RGD formula	I(dx)	RGD forward integration formula	RGD reverse integration formula
x_1	dx_1	$(x_2 - x_1)/4$	I_1	0	---
x_2	dx_2	$(x_3 - x_1)/4$	I_2	$4dx_1$	$I_6 - 4dx_4$
x_3	dx_3	$(x_5 - x_1)/4$	I_3	$4dx_2$	$I_7 - 4dx_5$
x_4	dx_4	$(x_6 - x_2)/4$	I_4	---	$I_8 - 4dx_6$
x_5	dx_5	$(x_7 - x_3)/4$	I_5	$4dx_3$	---
x_6	dx_6	$(x_8 - x_4)/4$	I_6	$4dx_4 + I_2$	$I_{10} - 4dx_8$
x_7	dx_7	$(x_9 - x_5)/4$	I_7	$4dx_5 + I_3$	$I_{11} - 4dx_9$
x_8	dx_8	$(x_{10} - x_6)/4$	I_8	---	$I_{12} - 4dx_{10}$
x_9	dx_9	$(x_{11} - x_7)/4$	I_9	$4dx_7 + I_5$	---
x_{10}	dx_{10}	$(x_{12} - x_8)/4$	I_{10}	$4dx_8 + I_6$	$I_{12} - 4dx_{11}$
x_{11}	dx_{11}	$(x_{12} - x_{10})/4$	I_{11}	$4dx_9 + I_7$	$I_{12} - 4dx_{12}$
x_{12}	dx_{12}	$(x_{12} - x_{11})/4$	I_{12}	$4dx_{12} + I_{11}$	

in the first column. The derivative of this vector is symbolically described in the second column as $f'(x)$ with symbolic derivative values dx_1-dx_{12}. Using the RGD approach, the numeric values of these derivatives are computed using the formulae in the third column for a gap $g = 4$. These are not true derivatives, and deviate from the true numerical derivative most obviously at the first two and last two points, where they decrease toward zero. For the central eight points, the derivatives are calculated using a conventional GD formula as expressed in Eq. 4.1.

These steps (Eqs. 4.1 – 4.5) can be repeated n times to form the n^{th}-order RGD, and a different gap size may be selected for each iteration. The order in which the different gaps are applied does not influence the central portion of the RGD. However, the special treatment of either end of the RGD causes the shape of the derivative ends to vary with the order in which different gap sizes are applied in RGD iterations (for $n \geq 2$). As a general rule, gaps should be applied in ascending order during RGD iterations to make the central portion of the RGD as wide as possible.

Even with the first condition met, an original vector and the integrated form of its RGD differ by at least one arbitrary constant. Further, the integration of the RGD might break into multiple independent sets of related equations with independent arbitrary constants. For example, the integrated form of the RGD might give one set of equations for all even points, and another for all odd points, each with separate arbitrary constants. These separate arbitrary constants, as mentioned above, are related to the difference between the first assumed value

of each set of related equations and the true first value of each set. When we relate the first $g/2$ values of the derivative to the first point of the integrated vector, we ensure that the first g points of the integrated vector can be directly related to the first point (Eq. 4.3). As all points beyond g are directly related to one of these first g points, our integration is now dependent on a single unknown reference value.

The third condition stated above is that this single unknown reference value of the spectrum can be assumed to have a specific value (e.g., zero) during integration. In our work, we have assumed that, when the first two conditions are met, all integrated points can be defined in terms of the value of the first point in the integration, x_1, which we take as zero. To satisfy this third condition we modify the original spectrum, and limit further processing of the spectrum, so the original spectrum and any RGDs calculated from it have values of zero for the first point. When these first values are defined as zero, integration allows the spectrum to be regenerated in its true form and allows any vectors that result from principal components analysis, PLSR, or other multivariate analysis methods to be integrated as well.

To fulfill the third condition, we first pad the beginning of the original vector with p values equal to the first point of the spectrum ($p = 2^{n-1} + 1$ for the n^{th} derivative) to ensure that all RGDs calculated from the spectrum are zero at the first point (see below for an explanation of how p is determined). We then add more copies of the first true point of the spectrum to provide a zone r over which the spectrum can be smoothly weighted from zero to unity that is at least equal to

the gap or, if multiple RGDs will be computed, equal to the sum of the gaps. If *k* is equal to the length of the original spectrum, the modified spectrum will be of length $q = r + p + k$. We require that the length of the RGD vector be even to ensure integration (*vide infra*), so if *q* is not even, we increase *r* by 1 to fulfill this condition.

A weighting vector of length *q* is then created. The first *p* values of the weighting vector are set to zero, and the weight increases from 0 to 1 over the next *r* points. The final *k* points of the weighting vector are set to 1. The final spectrum suitable for computing RGDs is obtained by multiplying the padded spectrum by this weighting vector. We have chosen a half sine wave form of the weighting vector for the *r* points over which the weights transition from 0 to 1 to limit the amplitude of the resulting derivative at the ends.

4.2.2. Example of Spectral Modification for fourth-order RGDs To illustrate the process described in the preceding section, consider a spectrum with *k* = 3320 spectral data points (illustrated in Fig. 4.1a), where we plan to apply a fourth-order RGD with gaps of $g_1 = 2$, $g_2 = 4$, $g_3 = 8$, and $g_4 = 20$ points.

Because we are calculating a 4th derivative, we require a minimum of *p* = 9 copies of x_1, the first data point of this spectrum, to be added as padding at the front of the spectrum. This value for *p* is a results of the treatment of the first points of the RGD expressed in Eqs. 4.2 – 4.3, which requires that the maximum value of *p* is given by $p = 2^{n-1} + 1$. For example, give *g* = 20 and *n* = 5, the first point of the 5th derivative is given by Eq. 4.2 as $f^{v}(x_1) = f^{iv}(x_2) - f^{iv}(x_1)$. After this point, Eq. 4.3 relates the values of each point in the derivative to the point in

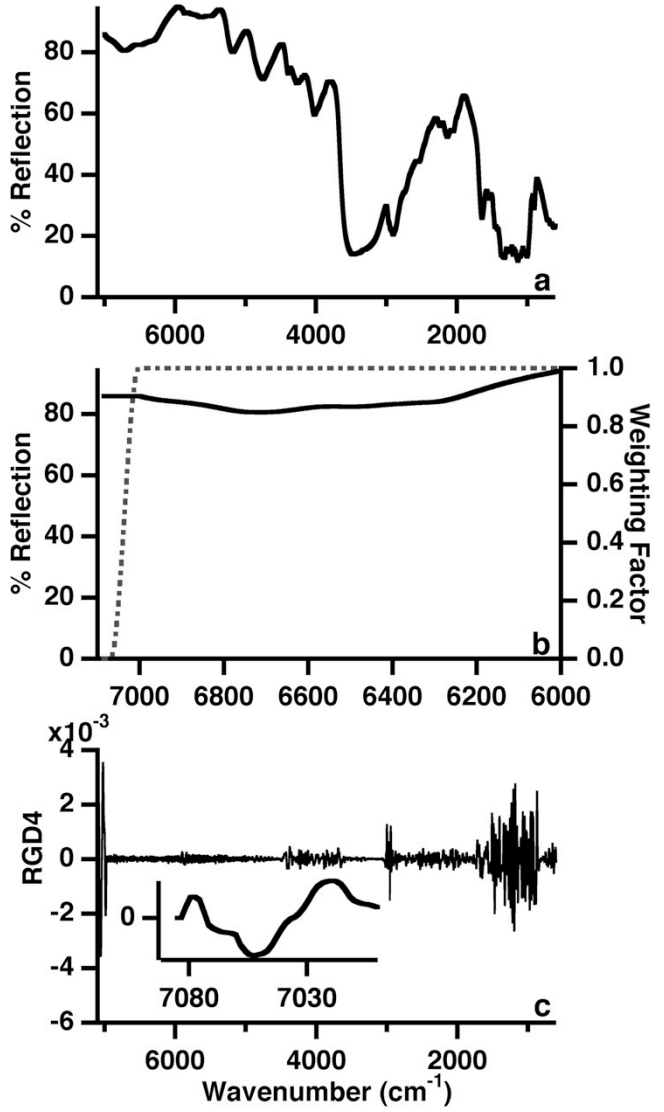

Fig. 4.1: Spectral modification and differentiation. (a) The original spectrum of 25x dilute blood on cotton fabric. (b) The left side of the spectrum shown in (a) now padded to 3364 points (black). The associated weighting vector is also shown (grey, dashed). (c) The fourth-order RGD taken of the product of the padded spectrum and weighting vector shown in (b).

the derivative one order less, as

$$f^{iv}(x_2) = f'''(x_3) - f'''(x_1)$$
$$f'''(x_3) = f''(x_5) - f''(x_1)$$
$$f''(x_5) = f'(x_9) - f'(x_1)$$
$$f'(x_9) = f(x_{17}) - f(x_1).$$

This shows that the most internal point of the original spectrum related to the first point of the 5th derivative is $p = 2^{5-1} + 1 = 17$. The value will often be less than this if the size of the gap is small enough to incorporate the use of Eq. 4.1 rather than Eq. 4.3. For example, if *g* = 6, the value for $f''(x_5)$ would be defined as

$$f''(x_5) = f'(x_8) - f'(x_2)$$

$$f'(x_8) = f(x_{11}) - f(x_5).$$

While the gap size influences the necessary value of *p*, the formula given to define *p* above is the maximum value for any gap size used at order *n*.

In addition to *p* = 9 points, we also need to allow a minimum of *r* = 34 points (= $g_1 + g_2 + g_3 + g_4$) to allow for gradual sinusoidal weighting of the spectrum from 0 to 1. Our modified vector length *q* is therefore 3320 + 34 + 9 = 3363 points. Because we require that our vector length be even, *r* increases to 35 points, and *q* becomes 3364 points, 44 points more than the original spectrum. We repeat the first point in the spectrum 44 times to get a vector of this length.

The weighting vector that we generate for the new *q* = 3364 point spectrum data has the first *p* = 9 points set to zero, and weights w_i for points *i* = 10 to *i* = 44 that sinusoidally increase as defined by

Eq. 4.6 $$2w_i = 1 - \cos\left(\frac{i-7}{3362-3320-7}\pi\right)$$

or more generally by

$$\text{Eq. 4.7} \qquad 2w_i = 1 - \cos\left(\frac{i-p}{r}\pi\right)$$

The remaining *k* = 3320 points in the weighting vector are set equal to 1 (Fig. 4.1b, grey trace). Multiplying this weighting vector by the augmented spectral data results in a dataset that smoothly increases from 9 initial zeros to the start of the original spectrum, ensuring that the original spectrum and its RGDs to the fourth-order all begin with zero. The same weighting vector is applied to all spectra in a set, each padded with 44 copies of its first point. The fourth-order RGD taken of the modified spectrum is shown in Fig. 4.1c (black trace).

4.2.3. Integration of RGDs The RGD defined by Eqs. 4.1 – 4.5 can be integrated to retrieve the zero-order spectrum. Each value of the derivative is defined by a relationship between two values of the original spectrum, which means that the integration is impossible to solve directly unless at least one of the values of the integrated vector is known *a priori*. The modification of the original spectrum described above ensures that we know the first value of the integrated vector, allowing us to begin integration with Eq. 4.8:

$$\text{Eq. 4.8} \qquad f(x_1) = 0$$

From here, we can determine values for the points of the integrated vector directly related to $f(x_1)$. The application of this and the following integration steps is demonstrated in Table 4.1 for the 12-point derivative vector introduced in the differentiation section (a discussion of the example follows this introduction of the equations). Many of the first *g* points of the integrated vector are found by solving Eqs. 4.1 – 4.1 (Eq. 4.9 – 4.10):

Eq. 4.9 $$f(x_2) = g * f'(x_1)$$

Eq. 4.10 $$f(x_{2i-1}) = g * f'(x_i), 1 < i \leq \frac{g}{2}$$

Note that even points from 4 to *g* are undetermined by Eq. 4.10. From the points for which values are defined by Eqs. 4.8 – 4.10, we can estimate much of the remainder of the spectrum using a recursive formulation given by Eq. 4.11 (based on Eq. 4.1):

Eq. 4.11 $$f\left(x_{i+\frac{g}{2}}\right) = g * f'(x_i) + f\left(x_{i-\frac{g}{2}}\right), \frac{g}{2} < i < k - \frac{g}{2}$$

Though we now have estimates for many points of the integrated spectrum, there are values that we cannot compute by recursion because the first term was not determined by Eqs. 4.8 – 4.10.

These currently undefined points can be determined by a reverse operation based on redundant definitions for the unknown variables, primarily those afforded by Eq. 4.4. We begin by defining the final point of the integrated vector as a function of the next-to-last point of the integrated vector and the final point of the derivative:

Eq. 4.12 $$f(x_k) = g * f'(x_k) + f(x_{k-1})$$

So long as the derivative vector is even, the next-to-last point of the integral will be directly related to the first point (as are all odd points). With the two final values of the integrated vector known, a relation similar to Eq. 4.10 can be used to find values for any points missing from the last *g*/2 points of the integrated vector (Eq. 4.13).

Eq. 4.13 $$f(x_{2i-k}) = f(x_k) - g * f'(x_i), k - \frac{g}{2} \leq i < k$$

Again, so long as the length of the derivative vector is even, Eq. 4.13 will be able to relate the missing values of the integrated vector to the first point of the integrated vector. After this point, we can fill in any missing values by working back through the vector toward the beginning using a recursion relation similar to Eq. 4.11 (Eq. 4.14):

Eq. 4.14 $$f(x_{k-i}) = f\left(x_{k-i+g}\right) - g * f'\left(x_{k-i+\frac{g}{2}}\right), g+2 \leq i \leq k-2$$

4.2.4. Example of RGD Integration Integrating an RGD is a more complicated process than calculating an RGD. To illustrate the process, refer to Table 4.1. The integral of $f'(x)$ is described by a vector $I(dx)$ where the integral has values I_1-I_{12} for each point at which the derivative is defined. The numerical values of this integral vector are defined by formulae obtained from algebraic manipulation of the RGD formulae, and are given in the last two columns of the table.

In the integration of the RGD, we assume the first point has a value of zero (Eq. 4.8). With that assumption we can write formulae for the first three values of the integral, I_1-I_3, and compute them explicitly (Eq. 4.9 – 4.10). The value I_4, however, cannot be found from any of these three values because x_4 does not appear in any RGD formulae of the third column in combination with values we know at this point in integration. The integrated values I_1-I_3 along with RGD values for dx_3-dx_5 allow I_5-I_7 to be determined (Eq. 4.11). The next value in the sequence, I_8, cannot be found at this point because its value is related to the RGD value dx_6 by I_4, which is yet unknown. The points I_9-I_{11} can be found from the values I_5-I_7 along with values of dx_7-dx_9.

The final point of the vector, I_{12}, cannot be calculated by Eq. 4.11. However, I_{12} is explicitly defined by Eq. 4.12, relating its value to I_{11} and the RGD value for dx_{12}. With I_{12} established, we can use Eqs. 4.12 – 4.13 to find redundant definitions for I_{11} and I_{10} based on I_{12}. There is not a reverse definition for I_9, but since it was defined in the forward integration that is unimportant. Using Eq. 4.14, we find definitions for I_8 and I_4 (along with more redundant definitions), which fills in the missing portions of the integral by working in reverse from the established terminal value of the integral.

In this example, as in the general practice, we defined the first point of the integral as $I_1 = 0$. If x_1 is not zero, the integrated vector will differ from the original spectrum $f(x)$ by the difference between I_1 and x_1. This offset is eliminated by conditioning the original spectrum such that $x_1 = 0$ by the method described earlier. Ensuring that $x_1 = I_1 = 0$ allows the integrated vector to be identical to the original spectrum except for numerical imprecision.

4.2.5. Numeric Precision Errors Numeric precision is the limiting factor in how accurately a spectrum can be integrated. Generally, a first-order RGD can be integrated with single precision calculations, generating errors on the order of 10^{-5} with the use of larger gap sizes (around 40 points) and spectra having lengths similar to those used here. Smaller gap sizes typically result in smaller errors; shorter spectral data also yield smaller errors (Fig. 4.2). Using double precision calculations, the error associated with the integration of a first-order RGD is on the order or 10^{-15}. As the derivative order increases, so does the error in integration. The influence of error on the shape of the integrated spectrum is

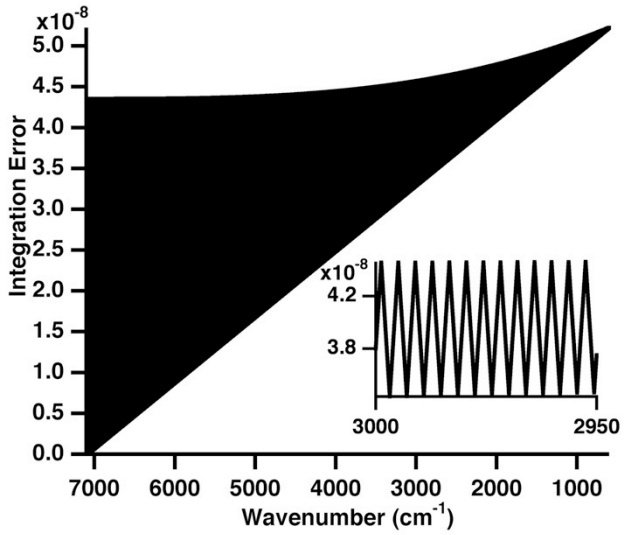

Fig. 4.2. Difference between original spectrum and vector integrated from fourth-order RGD.

visible in graphical representations of the data when the difference is near 1% of the spectral intensity. In our experience, this occurs at the around the seventh-order derivative.

Because the calculation used in integration is recursive, the numerical errors are not evenly distributed in the spectrum, but tend to grow from the values calculated first to the values calculated last. The derivative calculation is not recursive, so errors from the calculation of the RGD are always small; it is the integration step that dominates numerical precision errors.

4.2.6. Preprocessing Effects Based on the preceding explanation, we must ensure that the spectrum and any RGDs calculated from it have initial points equal to zero. This is especially true when working with RGDs beyond the first order, where offsets at the first stage of integration can dominate the actual spectral features at subsequent stages.

When we perform multivariate analysis of spectral data that meet this criterion, the initial points of LVs, RVs, and any vectors consisting of linear combinations of spectra will likewise have zeros as their first point, thus allowing integration. When derivatives are used without further transformation prior to multivariate calibration, the method described above fulfills this condition. However, derivatives are often used in conjunction with other preprocessing methods to improve calibration. Some transformations are applied exclusively prior to differentiation, such as response linearization (log(1/R), Kubelka-Munk transformation, *etc*.) or baseline correction. The first class of these transformations cannot be applied meaningfully to derivatives due to the

presence of negative values, and baseline correction would be redundant as derivatives work well to eliminate baseline effects. Other transformations might be applied before or after differentiation to achieve different results or per investigator preference. Any preprocessing method can be applied to the spectra prior to modification and differentiation without affecting the character of the RGD. However, caution must be exercised when these methods are applied to derivative spectra. Generally, transformations that maintain the value of the first points or scale the entire derivative are suited for partnership with RGDs, while transformations that involve addition or wavelength scaling must be adapted. Table 4.2 lists some preprocessing steps that might be applied after differentiation and discusses their compatibility with integration.

4.2.7. Matrix Formulation of RGDs It is possible to write a matrix formulation for the RGD process (Eqs. 4.1 – 4.3); the RGD matrix for a single differentiation step is a sparse *k* x *k* matrix (where *k* is the length of the original vector). For the simple example given above with a 12-point spectrum and a gap of 4, the transformation matrix T (12 x 12) is given as:

$$\mathbf{T} = \begin{pmatrix} -1 & 1 & 0 & 0 & 0 & 0 & 0 & 0 & 0 & 0 & 0 & 0 \\ -1 & 0 & 1 & 0 & 0 & 0 & 0 & 0 & 0 & 0 & 0 & 0 \\ -1 & 0 & 0 & 0 & 1 & 0 & 0 & 0 & 0 & 0 & 0 & 0 \\ 0 & -1 & 0 & 0 & 0 & 1 & 0 & 0 & 0 & 0 & 0 & 0 \\ 0 & 0 & -1 & 0 & 0 & 0 & 1 & 0 & 0 & 0 & 0 & 0 \\ 0 & 0 & 0 & -1 & 0 & 0 & 0 & 1 & 0 & 0 & 0 & 0 \\ 0 & 0 & 0 & 0 & -1 & 0 & 0 & 0 & 1 & 0 & 0 & 0 \\ 0 & 0 & 0 & 0 & 0 & -1 & 0 & 0 & 0 & 1 & 0 & 0 \\ 0 & 0 & 0 & 0 & 0 & 0 & -1 & 0 & 0 & 0 & 1 & 0 \\ 0 & 0 & 0 & 0 & 0 & 0 & 0 & -1 & 0 & 0 & 0 & 1 \\ 0 & 0 & 0 & 0 & 0 & 0 & 0 & 0 & 0 & -1 & 0 & 1 \\ 0 & 0 & 0 & 0 & 0 & 0 & 0 & 0 & 0 & 0 & -1 & 1 \end{pmatrix}$$

Table 4.2: Data treatments applied after differentiation.

	Method	Compatible with RGD[a]	Modification for Use
1	Smoothing[3-7]	No	
2	Mean-centering[3]	Yes	
3	Normalization[3]	Yes	Includes scaling to unit length, unit variance, unit area, or to the value at a reference wavelength.
4	Auto-scaling[3]	No	Works if the RV is divided by the standard deviation vector, integrated, then multiplied by the vector.[b]
5	Standard Normal Variate[5]	No	Scaling by the standard deviation achieves similar results because most derivatives have a mean near zero. Alternatively, the RV could be offset by the first value of the RV prior to integration.
6	Multiplicative Signal Correction[6-7]	No	This incorporates both a slope and offset term. Using only the slope achieves similar results because most derivatives have negligibly small offsets. Alternatively, the RV could be offset by the first value of the RV prior to integration.
7	Wavelength Weighting[4]	No	Works if the RV is divided by the weighting vector, integrated, then multiplied by the vector.[b] Does not work if the weighting vector contains zeros beyond the initial points.
8	Spectral Interference Subtraction[8]	Yes	

[a]All transformations are compatible with this technique if they are performed prior to extending the spectrum and taking the derivative. The question of compatibility refers to application to the modified zero-order or derivative spectra.
[b]Where division by zero occurs, the value should be corrected to zero prior to integration.

Notice that the matrix primarily comprises two off-diagonal vectors of − 1 and 1 starting at the locations $-g/2$ and $g/2$, respectively. The upper left and lower right corners of the matrix have unique definitions, corresponding to the regions of the spectrum we calculate differently from a typical GD. Transformation matrices corresponding to higher-order derivatives can be found by multiplying the appropriate first-order derivative transformation matrices together. To integrate the derivative to zero-order space, we would expect to find the reverse transformation matrix by taking the inverse of the derivative matrix. This allows simultaneous evaluation of every point in the integrated vector, eliminating the need for recursive calculations and thus for modification of the original spectrum as described above (though the spectrum must still have an even number of points). While this appears to be an elegant solution compared to our step-wise recursive calculation, the matrix approach has its own problems that outweigh its advantage in nomenclature and potential for combining multiple individual steps in a product matrix transformation.

First, the full-rank matrices used to describe RGDs are singular and cannot be inverted. This problem can be solved by eliminating the first column and row, reducing the matrix dimensions to k - 1 x k - 1, because we know that the first points in the derivative and integral are defined as zero. The transformation matrix reduced in rank by this method is not singular and can be inverted. This rank reduction means that the first point of the integrated vector cannot be determined by the matrix formulation and the derivative calculated will not be exactly the same as an RGD calculated by Eqs. 4.1 – 4.3 unless the

original spectrum is conditioned with zeros as described previously. Alternatively, we can look at the reduced rank matrix just described as a variant approach to defining the derivative in which opposite ends of a spectrum whose length is that of the reduced rank are treated differently. This alternative approach makes it possible to compute the “derivative” without conditioning the original spectrum, but with the caveat that the result is a hybrid of different levels of “differentiation”. In our laboratory we are still considering whether this approach has any benefits relative to RGDs as described here.

Secondly, while the calculation errors in integrating a first derivative RGD by the matrix method are similar to the recursive method, the errors mount faster with higher-order derivatives if the RGD transformation matrices are multiplied and a single inversion is used to find the integration matrix. This is because the product RGD matrices have more and more nonzero elements, which leads to greater imprecision in the inversion; however, this result is still due entirely to numerical precision limits. We have been unable to find a way around this numerical precision defect to the matrix approach without breaking the process into multiple steps of integration, the same as in the recursion method. For now it appears the matrix method offers no advantages, but may suffer from some disadvantages, compared to the recursion method.

4.3. EXPERIMENTAL

The sample preparation and data collection for the spectra presented here were previously described in Chapter 3. The spectra are infrared diffuse reflection spectra of blood on cotton fabric. PLSR calibrations (conducted using

PLS toolbox 6.7.1, Eigenvector Research Inc., Wenatchee, WA) were performed under four sets of preprocessing conditions, each followed by mean-centering: no preprocessing, standard normal variate transformed (SNV),[5] fourth-order RGD transformed, and fourth-order RGD transformed data scaled by the standard deviation. Throughout this manuscript, spectra scaled by the standard deviation will be referred to as normalized to unit variance. These data treatments are similar to those described in Chapter 3. In the case of RGD transformed data, the spectra were transformed using the combination of gap sizes previously reported to achieve the best calibration for blood on cotton fabric (g_1 = 2, g_2 = 4, g_3 = 10, and g_4 = 32 points), or the gap combinations noted in the following discussion. The calibration performances using the modified raw, modified SNV, and RGD approaches were compared to the calibration performance using the typical GD approach. In all cases, the results were nearly identical, showing that the modification of the spectrum and subsequent RGD calculation did not affect calibration. The optimum number of PLSR factors was determined for each calibration from the root mean squared error of calibration and root-mean- square error of prediction. For all models here, the optimum was 2 factors.

The routines for spectral modification, differentiation, and integration in both the recursive and matrix formulations were written in MATLAB® (The MathWorks, Inc., Natick, MA) and are reported in Appendix A.

4.4. RESULTS

4.4.1. Difference Spectra Figure 4.3 shows the mean difference between the spectra of cotton dip-coated in 25× dilute blood and the spectra of uncoated

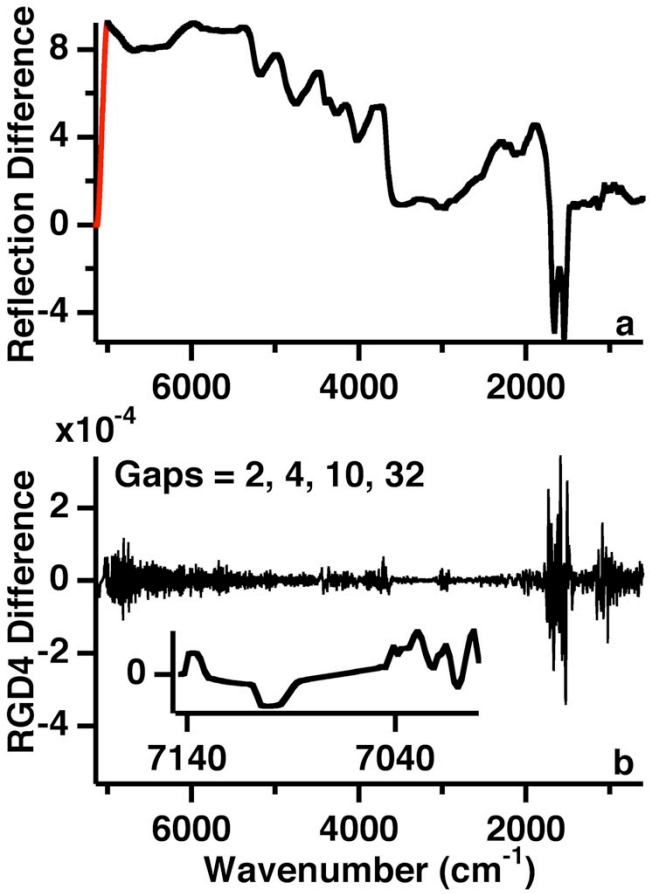

Fig. 4.3: Difference spectra in zero- and fourth-order space. (a) The difference spectra of 25x dilute blood on cotton and the uncoated cotton. The two traces in (a) are the original difference spectrum (black) and the difference spectrum of modified data (red). (b) The fourth-order RGD of the difference spectrum shown in (a). The gap combinations used were those previously shown to achieve the best calibration: $g_1 = 2$, $g_2 = 4$, $g_3 = 10$, $g_4 = 32$.

cotton. The top panel shows the mean difference spectrum in zero-order spectral space, and the bottom panel shows the equivalent difference in fourth-order derivative space. As mentioned in Chapter 3, the component spectrum of blood varies with the fabric on which it is deposited as a function of how the fabric spectrum interferes with the spectrum of blood. Thus, these spectra are characteristic of blood on cotton fabric, and differ from the component spectrum of blood on any other fabric. The RGD difference spectrum appears much more complicated than its zero-order analogue, and this complication obscures the identification of dominant peaks that are related to the presence of blood on the fabric. It is particularly difficult to interpret which wavelengths relate to an increase or decrease in reflection due to the presence of blood, information that indicates spectral changes caused by physical or chemical differences corresponding to the presence of blood. These kinds of differences are easier to discuss and interpret in zero-order space.

Two overlapping traces are shown in the top panel of Fig. 4.3. The first trace is the difference spectrum of the original, unmodified data (black; this is the same curve that appears in Fig. 3.3c). The second trace is the difference spectrum, modified to the to facilitate integration (red). The difference between the two is a length extending from the end of the original spectrum to zero, with the remainder of the difference spectrum unchanged. The zero-order spectrum integrated (not shown) from the fourth-order difference spectrum shown in the bottom panel perfectly overlays the original spectrum to the level of numerical precision.

Numerical integration of an RGD follows general rules of integration. For instance, if a block of derivative spectra have been mean-centered in derivative space, their integrals will be spectra mean-centered in zero-order space. Integrating a derivative spectrum that has been normalized to unit variance results in a zero-order spectrum that is likewise scaled by the standard deviation of the derivative spectrum. So long as the transformation does not alter the first values of the derivative, the integration remains possible (see Table 4.2 for a list of valid preprocessing options).

One commonly performed transformation that does not satisfy this criterion is the SNV transform, which involves subtracting the average value of each spectrum from the spectrum followed by normalization to unit variance.[5] The subtraction step alters the first values of the derivative, violating the third condition for integration. While the SNV transform cannot be performed, a similar effect can be achieved in derivative space by simply normalizing to unit variance without centering the derivative. These two treatments perform similarly because the mean of a fourth-order derivative is typically very close to zero.

While we can integrate the mean-centered derivative to its zero-order analogue, and we can integrate the derivative normalized to unit variance to a scaled zero-order spectrum, it is more difficult to define a zero-order analogue for a block of derivative spectra that have been mean-centered after normalizing to unit variance. The mean subtracted in this case contains variance information of all the spectra in the data block, and is a different mean from one that would be subtracted in zero-order space. Adding the integrated mean-centered spectrum

to the integrated mean yields the zero-order spectrum scaled by the standard deviation of the derivative, but neither the integrated spectrum nor the integrated mean have a direct zero-order analogue.

While looking at an integrated derivative spectrum is generally of little value (assuming the original spectrum used to calculate the derivative is available), this is one case where it can prove beneficial. To demonstrate, Fig. 4.4 shows difference spectra integrated from fourth-order RGDs calculated with different combinations of gaps sizes. The differences were taken between the mean spectra of 25x dilute blood on fabric and the spectra of uncoated fabric after the RGDs were normalized to unit variance and mean-centered. From these spectra one can see that different combinations of gap sizes followed by normalizing to unit variance can alter the appearance and relative intensity of spectral features, even when the difference in gap sizes is small, and these differences are often difficult to examine in derivative space. The importance of understanding these subtle differences is demonstrated in Chapter 3.

4.4.2. Regression Vectors Integrated weighting, loading, and regression vectors generated from PLSR of RGD-transformed data enable understanding of how gap sizes influence calibration. The derivative forms of these vectors are often difficult to interpret for the same reasons that the corresponding derivative spectra are difficult to interpret. Looking at the models in original spectral space is more convenient, and is possible by applying the integration algorithm presented above.

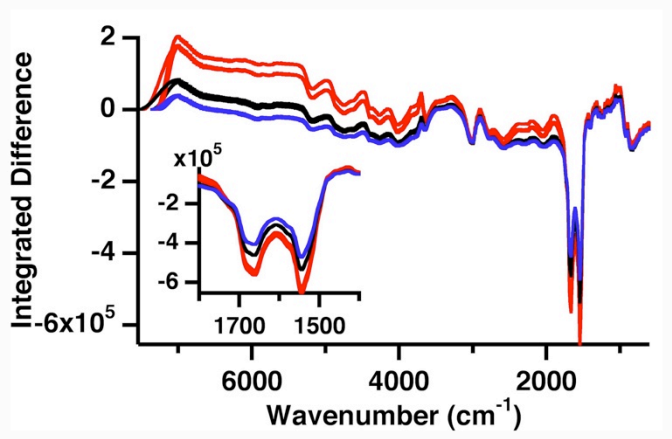

Fig. 4.4: Integrated difference spectra of mean-centered fourth-order RGD spectra normalized to unit variance. These are similar to the difference spectra in Fig. 4.3a, this time taken with different combinations of gap sizes. The combinations of gap sizes for the black traces are: 20,20,36,36; 24,24,34,34. The combinations of gap sizes for the red traces are: 20,20,40,40; 24,24,38,38; 30,30,34,34. The combinations of gap sizes for the blue traces are: 20,20,34,34; 24,24,32,32. The inset is an expansion of the Amide I and II region. The black traces correspond to gap sizes that have better calibration performance than the blue and red traces. The slightly different gap sizes cause noticeable changes in the difference spectra upon integration.

The black trace in the top panel of Fig. 4.5 shows the RV for the calibration of the SNV-transformed data, while the grey trace shows the integrated RV for the RGD data normalized to unit variance. Calibration using the RGD performs better than calibration of the original spectra, and it is useful for the analyst to have a means of comparing the two RVs. The bottom panel of Fig. 4.5 shows the RV from which the grey trace is integrated. The derivative RV shows regions of highly congested peaks where we would expect to see peaks related to the presence of blood, but it is difficult to say much beyond that. In contrast, both RVs in spectral space are much simpler, with two primary peaks corresponding to the Amide I and II protein bands of blood (See Fig. 3.2). While these two RVs are similar, there are a few key differences. The integrated RV places more emphasis on the Amide I and II bands relative to other features. This suggests that the derivative calibration model is less sensitive to the change in surface morphology of the cotton fabric in the presence of a coating, and is rather more specific for the presence of blood. This difference is apparent where the SNV-based RV has positive features, denoting an increase in reflection with the presence of a coating, a characteristic that is not of particular interest when developing a calibration for a specific surface coating.

Further, the Amide I and II bands are more equally weighted in the integrated RV than they are in the SNV-based RV, a relationship more closely resembling that shown in Fig. 4.3. The Amide II band appears in a region of higher reflectance for the spectrum of cotton fabric while Amide I overlaps with a reflectance minimum in the spectrum of cotton. The derivative processing is

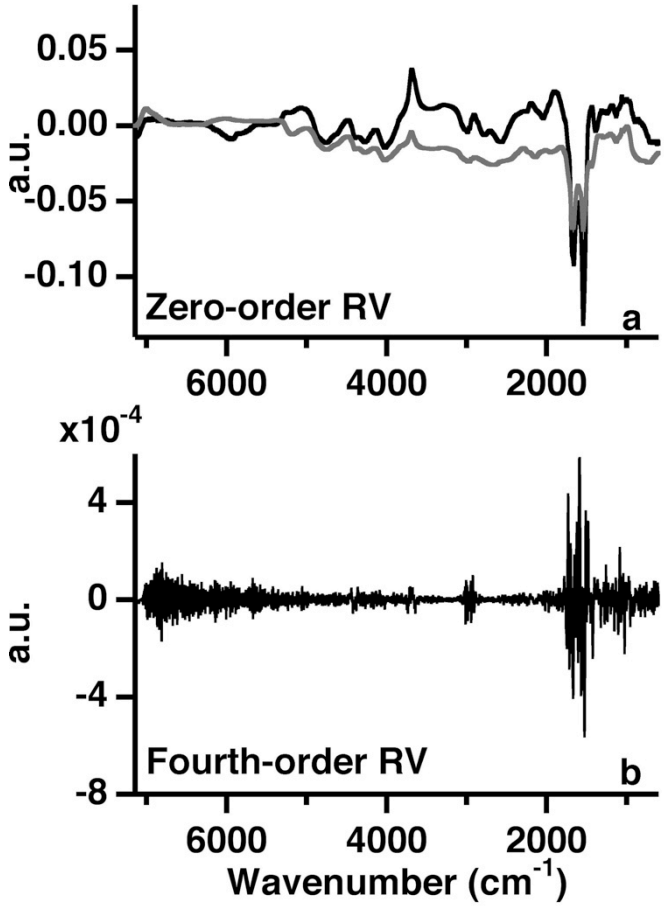

Fig. 4.5: Regression vectors (RV) for the PLSR calibrations. (a) The RV based on SNV-transformed data (black) and the integrated RV based on RGD transformed data normalized to unit variance (grey), both normalized to unit length. (b) The RV based on RGD transformed data normalized to unit variance in fourth-order space. The derivative RV appears much more convoluted than the zero-order analogue shown in the top panel. Generally, the integrated RV is less sensitive to changes in the NIR region (beyond 5000 cm^{-1}) and features the amide bands more prominently.

better able to separate the Amide I band from the cotton band, thus enabling calibration more evenly based on both Amide I and II bands, capitalizing on the relationship between these bands to strengthen the calibration.

Integrated RVs can also aid comparison of model performance between calibration models based on derivative spectra transformed with different combinations of gap sizes. To demonstrate, Fig. 4.6 shows the RVs based on the RGD transformed data shown in Fig. 4.4 (whose caption records the relevant gap combinations). The inset of Fig. 4.6 shows the Amide I and II portion of the second factor of these models. Though the differences in gap size combinations used for each model are minor, they result in noticeably different calibration performance (displayed in Fig. 3.4). The black traces in Fig. 4.4 and Fig. 4.6 have lower prediction error compared to the blue and red traces, suggesting those gap sizes affect a change in spectral features that improves calibration. Chapter 3 explained this improved calibration performance by interpreting the derivative transformation as a matched filter for spectral features. In this interpretation, certain combinations of gap sizes selectively highlight particular patterns in the spectra and minimize others, thus improving PLSR calibration.

With that in mind, we notice that the RVs with smaller errors more equally weight the Amide I and II bands (this difference is similar to the difference between the SNV and derivative RVs). Also, and perhaps even more readily apparent, the center region between the two bands is more heavily weighted relative to the amide bands in the black traces. This difference can be attributed to the second factor (Fig. 4.6, inset; the first factor, not shown, is similar for all

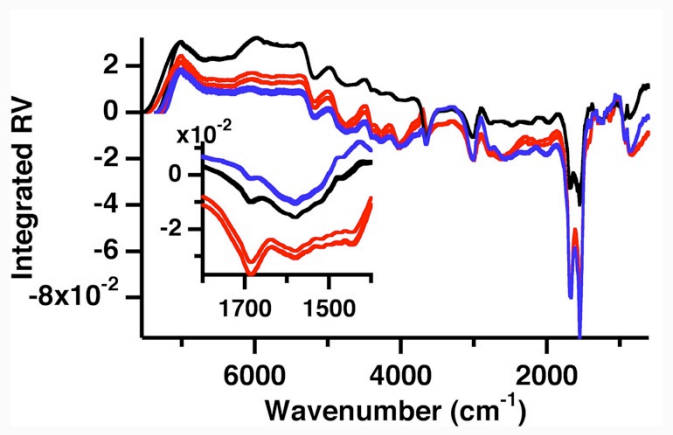

Fig. 4.6: Integrated regression vectors (RVs) based on data in Fig. 4.3. The integrated RVs are normalized to unit length. The black traces corresponding to enhanced model performance show generally lower amplitude, and greater emphasis on the values near 1600 cm^{-1} relative to the amide bands than seen in the other RVs. The inset displays the second factor from the same models. The first weighting for each is similar, but this vector shows important differences. The black traces have a feature at 1600 cm^{-1}, the area of the RV that is different, and the second factor is weighted more heavily in the definition of the RV. These factors demonstrate that small differences in gap size can cause larger differences in calibration that can best be explored by integrating the model vectors.

models and resembles the difference spectra in Fig. 4.4). The second factor in the better models is weighted more heavily in that region, and this factor is more strongly weighted in the final RV of the model compared to the red and blue traces. These differences suggest that the combination of gap sizes used in the RGD transformation of the data corresponding to the stronger models better enhances the relationship between the amide bands relative to other sources of variance in the spectra.

The usefulness of integrated RVs is currently limited to qualitative examination of model performance in zero-order space, not quantitative application. Integrated RVs cannot be used to make predictions in zero-order space because (1) there is no direct zero-order analogue for the integrated derivative vectors that have been normalized to unit variance prior to mean-centering and (2) the integrated RVs are based on derivative models, which do not have sources of variance such as baseline slope and offset. Calibration models only perform well when presented with data that contain variation also present in the calibration set. In this case, zero-order spectra contain more sources of instrumental and environmental variability than the derivative spectra contain, so the integrated RV cannot properly predict the analyte concentration. An optimized polynomial function might be added to the integrated RV to account for some of this variance, but the results are unlikely to exceed the performance of a calibration created in zero-order space.

4.5. CONCLUSIONS

We have demonstrated the integration of both spectral derivatives and the vectors resulting from PLSR calibration, as well as shown how integration can shed light on how gap sizes selected for RGD transformations influence calibration. The integrated RVs cannot be used for calibration in zero-order space because the zero-order spectra are characterized by variance that is simply not present in the derivative data. However, differences between integrated RVs and zero-order RVs might offer insight to how those variations in the zero-order data influence calibration.

Derivative-based RVs are developed in a space free of spectral artifacts such as baseline offset, slope, and curvature. These artifacts are different for each spectrum, and complicate the formulation of a RV in zero-order space. The RV is meant to be orthogonal to variance not related to analyte concentration. If each spectrum has its own specific spectral artifacts, the RV appears orthogonal to the mean of those artifacts present in the calibration data. The differences between a RV developed in a space free of artifacts and one developed in the presence of artifacts can be indicative of the (a) the extent of variability due to artifacts in the calibration data, and (b) the extent to which these artifacts influence calibration in the zero-order.

REFERENCES

(1) W. L. Butler. "Fourth Derivative Spectra". Methods Enzymol. 1979. 56: 501-515.

(2) S. A. DeJong, W. L. O'Brien, Z. Lu, B. M. Cassidy, S. L. Morgan, M. L. Myrick. "Optimization of Gap Derivatives for Measuring Blood Concentration of Fabric from Vibrational Spectroscopy". Appl. Spectrosc. 2015. 69 (6).

(3) P. J. Gemperline. "Principal Component Analysis". In P. J. Gemperline, editor. Practical Guide to Chemometrics. New York: Taylor & Francis, 2006. 2nd ed. Ch. 4, Pp. 69-104.

(4) H. Martens, T. Naes. "Pretreatment and Linearization". In: Multivariate calibration. New York: Wiley, 1989. Ch. 7, Pp. 314-356.

(5) R. J. Barnes, M. S. Dhanoa, S. J. Lister. "Standard Normal Variate Transformation and De-Trending of Near-Infrared Diffuse Reflectance Spectra". Appl. Spectrosc. 1989. 43 (5): 772-777.

(6) P. Geladi, D. Macdougall, H. Martens. "Linearization and Scatter-Correction for near-Infrared Reflectance Spectra of Meat". Appl. Spectrosc. 1985. 39 (3): 491-500.

(7) H. Martens, T. Naes. "Multivariate Calibration by Data Compression". In: P. C. Williams, K. H. Norris, editors. Near-Infrared Technology in the Agricultural and Food Industries. St. Paul, USA: American Association of Cereal Chemists, 2001. 2nd ed. Ch. 4, Pp. 59-100.

(8) H. Martens, E. Stark. "Extended Multiplicative Signal Correction and Spectral Interference Subtraction - New Preprocessing Methods for Near Infrared Spectroscopy". J. Pharm. Biomed. Anal. 1991. 9 (8): 625-635.

CHAPTER 5

DETECTION LIMITS FOR BLOOD ON FABRIC USING INFRARED DIFFUSE REFLECTION SPECTROSCOPY

5.1. INTRODUCTION

Luminol, which undergoes a chemiluminescent reaction with the heme groups of blood, is one of the most commonly used presumptive tests for the visualization of blood in criminal investigations.[1] Though favored for its potentially high sensitivity and ease of use,[1] luminol has several drawbacks, including the limitation of use in a dark environment.[2] Luminol gives false positives for a variety of common interferents, including iron, copper, paints and varnishes, and plant peroxidases.[3] Luminol also requires investigators to take precautions to limit potential health hazards.[4-5] Further, while luminol does not degrade DNA on fast time scales, it does reduce the recoverable quantity of DNA in a treated bloodstain relative to the amount of blood present in an untreated bloodstain over the course of six months. As a result, DNA recovery from luminol treated bloodstains must be analyzed well within this time period.[6]

As mentioned in the Chapter 1, infrared (IR) spectroscopy has been suggested as an alternative presumptive method for blood detection, offering the benefits of being non-destructive, non-hazardous, and field ready. Infrared imaging and spectroscopy have already been demonstrated for the analysis of fabrics and bloodstains.[7-10] Recently, a digital camera was adapted to image

forensic samples in the near-IR region.[11] Protein structure has long been investigated with IR spectroscopy[12-14] and the age of bloodstains has been studied by near-IR spectroscopy.[15-16] Diffuse reflection IR spectroscopy has also been used to examine fabric composition, dye state, and treatments.[17-24] We recently reported a thermal IR (8 – 14 μm) imaging system using reflectance imaging as a stand-off technique to visualize blood on a fabric.[25-27]

The performance of presumptive forensic tests is often reported as a detection limit (DL), typically in terms of dilution factor. Dilution factor DLs are quantitatively useful when comparing analyses of solutions because the unit can be readily converted into mass percent or other units, but the concept is only qualitatively or relatively useful when discussing a dried analyte on a surface. If a specific quantity of diluted solution is dried on a consistent substrate, and a single experimental method is used to characterize the sample, then dilution factor DLs have some significance. But when substrates are of very different types (e.g., porous vs. nonporous); or when methods have different depths of penetration (e.g., X-ray absorption vs. IR attenuated total reflection); it is difficult to perform a quantitative comparison of DLs in terms of dilution factors. In the case of forensic analysis, DLs in terms of dilution factor are not readily converted into analyte mass available for a biochemical assay or genetic testing. Depending on the type of substrate and method, DLs in terms of coverage (mass/unit area), average film thickness, or mass percentage may be more appropriate for comparing DLs of different experimental methods.

Further, while a known volume of blood at a certain dilution factor may be applied to a substrate, there is currently little control over how this solution might be distributed on that substrate. Partly for this reason, the DLs reported for the visualization of blood on fabric using luminol span nearly 5 orders of magnitude,[28-31] from 100x blood dilution[32] to more than 5,000,000x dilution.[1] It is difficult to resolve the disparities in these reported DLs because none have been determined using a statistically valid approach. Beyond having an incomplete description of sample preparation, it is common to find one or more of the following problems in the literature of blood detectability with luminol: (a) lack of or incomplete control measurements, (b) failure to observe any samples without a response, (c) visual observation with a non-blind measurement protocol, (d) incomplete reporting of the experimental method, (e) lack of quantitative measurements, and (f) lack of statistical analysis of data, including lack of data validation of any type.

We follow earlier work from this laboratory showing that an even distribution of fluid and dissolved analytes on fabrics can be obtained reproducibly via dip-coating.[17] While dip-coating is consistent, the amount of material deposited on different samples dip-coated from the same solution varies as a function of substrate characteristics. For example, the surface area available for deposition varies with fabric type, fabric thickness, fiber size and shape, and fabric weave. Following the method of reference 17, we use gravimetric measurements to convert DLs in dilution factors into DLs in mass percentage and coverage of blood solids on our fabrics. A separate measurement of the

specific surface area of each fabric by Brunauer-Emmet-Teller (BET) adsorption isotherms plus the density of solid crystalline albumin[35] as a proxy for the density of blood solids is used to determine a DL in terms of the average film thickness in nanometers.

This work reports DLs in different wavelength regions across the IR, and discusses the DLs reported in the literature for blood detection by luminol in alternate units that may be better suited for comparing method performance.

5.2. METHOD

The spectra used to estimate DLs for blood on acrylic, cotton, and polyester fabrics are the same as those used in Chapter 3. Nylon is also included in this study, and the sample preparation and spectral collection for that fabric is the same as for the others.

5.2.1. Calibration The spectra were analyzed using multivariate calibration. There are many different flavors of multivariate calibrations and pretreatment methods. While our spectra were acquired to minimize misinterpreting moisture and temperature variation, instrument drift, fabric alignment variations, and other experimental factors over different days as factors in blood detection, diffuse reflection spectra still show variations in offsets and intensity that can degrade calibrations. A variety of spectral pretreatments have been developed to mitigate these problems, among which are various types of normalizations, corrections, and derivative procedures. Chapters 2-3 provide an extensive investigation of the effects of different derivative treatments combined with normalization as preprocessing for partial least-squares regression (PLSR). Of the methods

tested, we found that higher-order gap derivatives (GDs) have characteristics that enable more sensitive detection of blood on fabrics when optimized compared to Savitzky-Golay smoothing or derivatives. Accordingly, we chose to focus on fourth-order GDs (GD4s) optimized by exhaustive searching using combinations of 4 gaps from 1 – 50 points.

The IR diffuse reflection spectra (600 – 7000 cm^{-1}) were processed by GD4 transformations with combinations of gaps ranging from 1 – 50 points (1.93 – 96.4 cm^{-1}).[36] Because GD4 processing causes data points to be lost from either end, the derivative spectra were trimmed to the length of the shortest derivative: 793 – 6808 cm^{-1}. The derivative spectra were divided into each of the following wavelength regions: all wavelengths (793 – 6808 cm^{-1}), long-wave mid-infrared (LWMIR, 793 – 2000 cm^{-1}), short-wave mid-infrared (SWMIR, 2000 – 3800 cm^{-1}), long-wave near-infrared (LWNIR, 3800 – 5000 cm^{-1}), and short-wave near-infrared (SWNIR, 5000 – 6808 cm^{-1}). Models were also developed in the wavelength region pertinent to the IR camera used in the above-mentioned instrument: 793 – 1250 cm^{-1} (12.6 – 8 μm).

The derivative spectra of each wavelength region were then standard normal variate (SNV) transformed and mean-centered prior to calibration for concentration of blood on fabric by PLSR using the PLS toolbox 6.7.1 (Eigenvector Research Inc., Wenatchee, WA). The method was calibrated to the inverse dilution factor because it is known that the mass of solids deposited during dip-coating from a solution is inversely related to the dilution factor.[17,36] The number of latent variables (LV) retained in all models was the most common

optimum number identified by the root-mean-square error of cross-validation (RMSECV) and the root-mean-square error of prediction (RMSEP) among the calibrations with varying gap sizes of that particular wavelength region. After the number of LVs was determined, models were evaluated by the ratio of the standard deviation of the reference values to the RMSEP (known as the RPD) and only models with an RPD ≥ 3 at this number of LVs were retained as calibrations with acceptable performance.[37]

5.2.2. Non-Linearity Studying diffuse reflection spectra of coatings such as blood on fabrics involves dealing with highly non-linear spectral behavior,[17] particularly when weak fabric absorption is combined with strong coating absorption, as discussed in reference 17 (see Fig. 7 of ref. 17, Fig. 5.1). This non-linearity complicates DL estimation from linear techniques such as PLSR. Though the log(1/R) transform and non-linear techniques are commonly applied to improve calibrations of non-linear data, our investigations did not show improvement upon implementation, so those results are not included here.[36] DL estimates may be improved by using only the most dilute samples, where the calibration is also most linear. Consequently, we estimated DLs for the retained calibrations from the slope across the blank, 200x dilute, and 100x dilute samples of the validation set, where it will be most similar to the slope at the DL. To ensure models remain valid for predicting blood concentration at higher values, we continued to develop calibrations using the full span of concentrations and retained only those full models with RPD ≥ 3, using the slope across the predictions of the lowest three concentrations to estimate the DL. This DL can

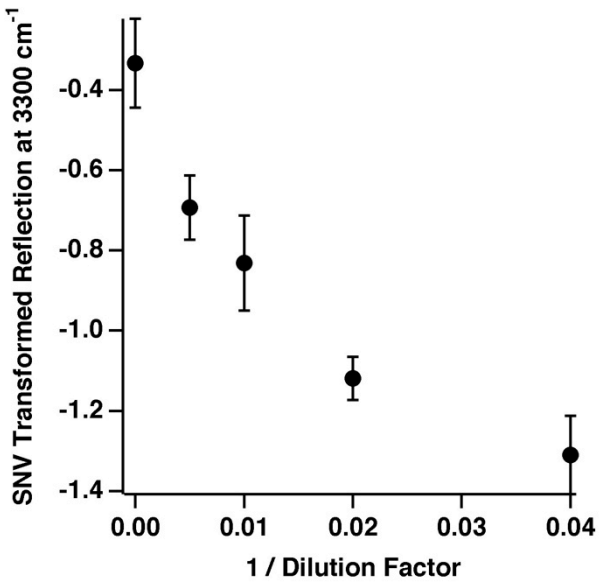

Fig. 5.1: The average SNV transformed reflection of blood on acrylic at 3300 cm^{-1} (corresponding to Amide A) shown as a function of inverse dilution factor (error bars are sample standard deviation).

still be considered a conservative estimate because the slope representing the calibration response is greatest between the blank and 200x dilute samples and is reduced by the inclusion of the 100x dilute sample.

5.2.3. Detection Limit Estimation Detection limits were estimated by Eq. 5.1 (similar to univariate techniques[38-39]):

Eq. 5.1 $$DL = \frac{1}{3 \times \sigma_{\hat{y}} / m_{y,\hat{y}}}$$

where $\sigma_{\hat{y}}$ is the standard deviation of the predicted values of the blank samples and $m_{y,\hat{y}}$ is the slope of the linear fit between the model reference and predicted values. Equation 5.1 includes the inversion of the initial DL estimate because the model is calibrated to inverse dilution factor, thus resulting in an initial DL estimate in terms of inverse dilution factor. DLs estimated using $3\sigma_{\hat{y}}$ correspond to a 0.14% false positive rate assuming normally distributed measurement errors. Using the standard deviation of the blank samples and the slope across concentrations reasonably assumes that the variance is not dependent on analyte concentration. The DLs reported here are the best DL determined among models with an RPD ≥ 3 for a given wavelength region. We note the specific cases where no models are considered satisfactory by the RPD criterion. The combinations of gap sizes that resulted in these best DLs are reported alongside the calibration results for each wavelength region.

5.2.4. Detection Limit Unit Conversion To better enable DL comparison among experiments and detection methods, we converted the estimated DLs in units of dilution factor to mass percentage, coverage, and film thickness using the mass of blood added, density of albumin (taken as an approximation of the

density of blood solids),[35] fabric areal density, and the specific surface area of the fabrics found using a BET isotherm technique.

To determine the relationship between the dilution factor of a solution of blood and the amount of blood solids added to a fabric by dip-coating from that solution, we determined the mass of blood solids added to each fabric square by dip-coating. The sample squares were weighed 5 consecutive times 24h after sonication in deionized (DI) water, and again 24h after dip-coating from DI water, 200x dilute blood in DI water, 100x dilute blood in DI water, 50x dilute blood in DI water, or 25x dilute blood in DI water. The difference between the mass of dip-coated fabric and the mass of the cleaned fabric is the mass of blood added to the sample. This value was used to determine mass percent (% w/w) blood of the fabric samples or coverage ($\mu g/cm^2$, with an apparent sample surface area taken as exactly 25.8 cm^2). Upon determining the mass percent of the fabric samples, we noted that the samples dip-coated from DI water had an apparent increase in mass after dip-coating. We attribute this apparent mass increase to the hygroscopic nature of fabrics:[40] the masses of the dip-coated fabric squares were obtained on a day with 15% higher relative humidity than the day on which the masses of the sonicated fabrics squares were obtained (a disadvantage of working in South Carolina in the summertime). As a result, the samples lost less water during the 24h after dip-coating than the samples had lost during the 24h after sonication. To account for this, the mass percent or coverage values for each fabric were offset by the average apparent value of the blank samples (those dip-coated from DI water). The corrected sample values at each dilution

are shown in Fig. 5.2-5.3. The best-fit line for the data of each fabric was found without any constraints on the intercept. The *y*-intercepts for these lines were all statistically indistinguishable from zero, so the fit was repeated, now constraining the *y*-intercept to zero. The resulting linear fits are shown in Fig. 5.2 – 5.3 with the slopes recorded in the legend. These slopes can be used to convert the units of dilution factor to mass percent and coverage by Eqs. 5.2 – 5.3:

Eq. 5.2 $$\frac{100*g\ blood}{(g\ blood+g\ fabric)} = \left(\frac{1}{df}\right) m_1$$

Eq. 5.3 $$\frac{mg\ blood}{cm^2\ fabric} = (\frac{1}{df}) m_2$$

Conversion to an estimated DL in terms of the effective film thickness divides the coverage value by the product of the specific surface area per gram of fabric with the areal density of the fabric in g/cm^2 and the estimated density of blood solids. This result is then expressed in units of nanometers for convenience. The specific surface area of each fabric is found using a BET isotherm technique (Fig. 5.4), and are as follows: (1) acrylic: 0.272 ± 0.007 m^2/g; (2) cotton: 0.940 ± 0.002 m^2/g; (3) nylon: 0.41 ± 0.04 m^2/g; and (4) polyester: 0.057 ± 0.014 m^2/g. The areal densities of these fabrics were measured by gravimetry as follows: (1) acrylic: 0.0296 g/cm^2; (2) cotton: 0.0257 g/cm^2; (3) nylon: 0.0346 g/cm^2; and (4) polyester: 0.0121 g/cm^2. The density of albumin is used as an approximation of the density of blood solids, and is taken from reference 35 of the manuscript as ρ = 1.36 g/cm^3. Equation 5.4 relates film thickness to the coverage defined in Eq. 5.3:

Eq. 5.4 $$film\ thickness = \frac{coverage}{areal\ density * specific\ surface\ area * \rho_{blood}}$$

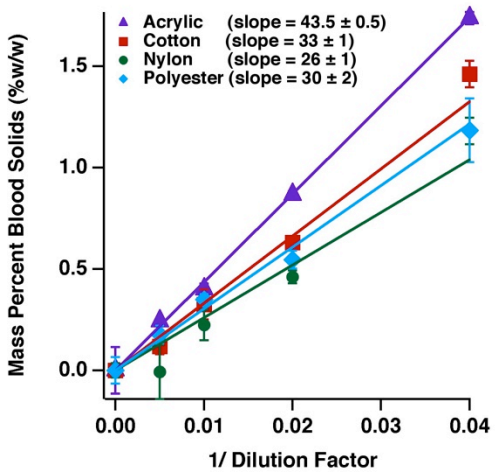

Fig. 5.2: Relationship between mass percent blood solids and dilution factor. Each marker is the average mass percent (% w/w) of blood added to 5 replicate sample squares of each fabric, offset by the apparent average value of the blank samples. The error bars are ± one standard deviation of the replicates.

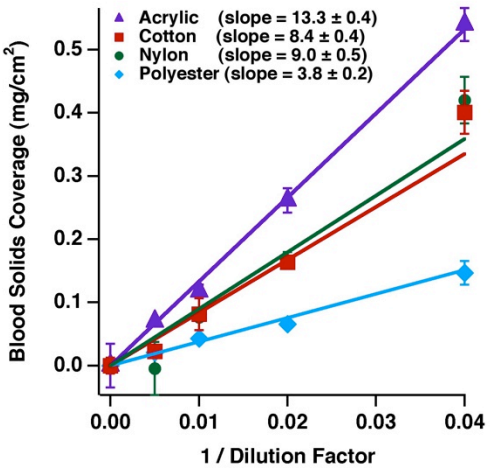

Fig. 5.3: Relationship between coverage of blood solids and dilution factor**.** Each marker is the average coverage (mg/cm^2) of blood added to 5 replicate sample squares of each fabric, offset by the apparent average value of the blank samples. The error bars are ± one standard deviation of the replicates.

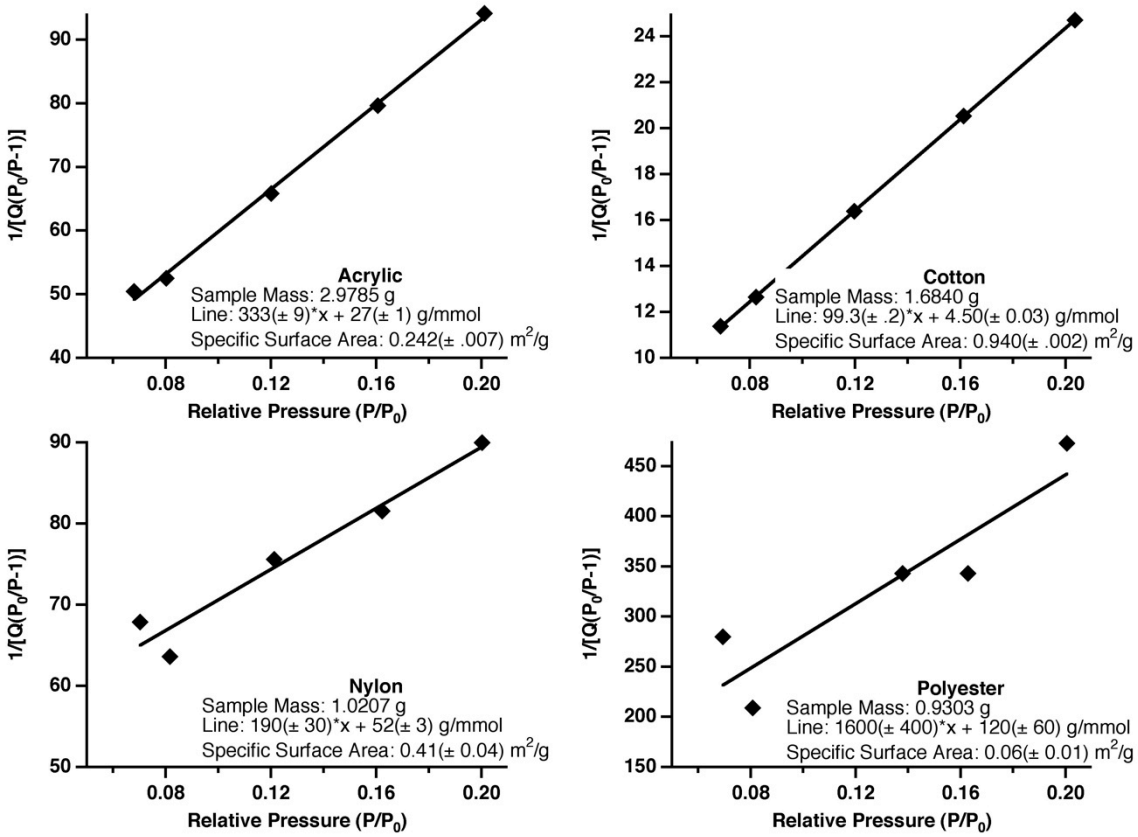

Fig. 5.4: BET Isotherm Experiments. The results of the 5-point BET isotherm experiments are shown for each fabric. The legend records the sample mass, the line of best fit, and the specific surface area reported. All BET isotherm experiments were run on a Micromeritics ASAP 2020 in physisorption mode.

5.2.5. DL Confirmation To test the DLs found through PLSR, new samples were prepared as described above, now dip-coated from solutions closer to the best DL found for each fabric. Six sample squares each of acrylic, cotton, and polyester were sonicated in DI water and suspended to dry for 24 h. Of these, 3 squares of each fabric were dip-coated from DI water and suspended to dry. The other three sample squares were dip-coated from blood diluted to a level near the DL and suspended to dry. Acrylic squares were dip-coated from blood diluted to 2000x (DL = 2300x); cotton squares were dip-coated from blood diluted to 400x (DL = 610x); polyester squares were dip-coated from blood diluted to 800x (DL = 900x).

Ten replicate diffuse reflection spectra were collected of each sample square and transformed by the optimal gap combination prior to prediction by the model resulting in the best DL. Due to the time elapsed between the original set of measurements and this new sample collection (about 2 years), the new spectra corresponding to the blank samples showed marked differences from the original calibration spectra. In part, these differences resulted from degradation of the SNR of the instrument over a period of two years; the new spectra were acquired at a time when the purge gas system for the spectrometer was broken, leading to a general degradation of the instrument. The instrument was originally chosen for this work because it had the best overall SNR of any instrument available to the authors, so this loss of quality affected the precision of our blanks most noticeably.

Other differences resulted from long-term changes in the response of the instrument (probably related to the general degradation mentioned above), but also from long-term changes in the chemistry of one fabric (polyester, which slowly hydrolyzes when exposed to air, and which was two years older for the new experiments). Despite these problems, in each case the test concentration samples showed a response relative to the new blanks as expected and reported in the manuscript. The blanks showed greater imprecision, leading to a higher than expected false positive rate (6% instead of the expected 0.13%).

The new blanks showed spectral characteristics due to instrumental and fabric changes such that they were not the same as the original blanks. However, the new spectral data could be reduced to the space of the original spectra as follows. To make the old and new spectral sets more comparable, principal component analysis was performed on the blanks of the calibration set and the new blank spectra. The new spectra were corrected by recentering the new spectra so the blanks scored on average the same as the old blanks on the first or second principal component of the blank samples. The number of true and false positives out of the 30 blank and 30 coated spectra are displayed below.

5.3. SPECTRAL REGION OVERVIEWS

Two characteristic strong protein absorptions are expected to appear in the information rich LWMIR wavelength region (600 – 2000 cm^{-1}): the Amide I and Amide II bands. The Amide I band typically appears near 1650 cm^{-1} and corresponds to the hydrogen-bonded carbonyl stretch of the peptide backbone. The Amide II band appears around 1550 cm^{-1} and can be considered a peptide

group frequency, related to both C-N stretching and N-H bending of the peptide backbone.[12,41] These two bands appearing in combination with one another is highly indicative of the presence of proteins and other secondary amides, and so can be expected to provide a strong basis to calibrate for the concentration of blood on fabrics. Other bands related to proteins, though less specific, are found at 1250 cm^{-1} (another peptide group vibration), and from 1300 – 1460 cm^{-1} (related to C-H deformations).[12,41]

While the LWMIR wavelength region is highly informative, it is more challenging to develop a system robust enough to use in the field with the available optics and instrumentation. Traditional inexpensive and easy-to-manufacture glass optics are not transparent in this region, necessitating the use of alternative materials, which are often difficult to form into high quality optics. Some IR-transparent materials are also hygroscopic, meaning any exposure to atmospheric humidity will be detrimental to the system's operation.[42-48] Thermal detectors used in this region tend to be less sensitive than the detectors used in the shorter wavelength regions, while IR photon detectors usually require thermoelectric or cryogenic cooling.[49]

The SWMIR region (2000 – 3800 cm^{-1}) contains the characteristic Amide A and Amide B protein bands. The Amide A band, a broad feature near 3300 cm^{-1}, corresponds to the N-H stretching of a secondary amide. The Amide B absorption band is much weaker and might be seen near 3100 cm^{-1}. This band is the overtone of the Amide II band strengthened by Fermi resonance with the Amide A.[12,41,50] In addition to the amide bands, CH_2 symmetric and anti-

symmetric stretching vibrations are seen near 2900 cm^{-1}. Again, these bands are less specific to the presence of proteins and so are less useful for discriminating blood from a matrix. [37,49] However, sapphire optics, which are more robust and easier to tool than the longer wavelength optics, may be used in this wavelength region. [42,47-48] Some quantum detectors can be used in this region, such as HgCdTe (MCT), PbSe, and InSb detectors. These detectors can be either thermoelectrically cooled or even uncooled (like photoconductive PbSe). MCT detectors can be used in this wavelength region as well as at even shorter wavelengths because the spectral response of MCT detectors can be adjusted by varying the relative amounts of each material in the detector.[49]

Bands located in the LWNIR region are generally overtone and combination bands that can be described in terms of the fundamental normal mode vibrations of molecules, particularly those vibrations that involve motion of hydrogen atoms. These bands are typically an order of magnitude or more weaker than strong vibrational absorption bands in the mid-IR spectral window. Spectral congestion, broad linewidth, and the ubiquity of hydrogen in the molecular structure of both fabrics and blood solids often make it difficult to differentiate analyte bands from those of the substrate in the near-IR. If protein bands are distinguishable from the substrate spectrum, they would appear in three primary locations in the LWNIR (3800 – 5000 cm^{-1}). Combinations of the CH_2 stretching and bending vibrations (2900 and 1300 – 1460 cm^{-1}, respectively) might be seen from 4200 – 4360 cm^{-1}.[12,41,50] More specific to proteins, combination and overtone bands related to amide fundamentals are located in

this region. The combination of Amide II (1550 cm^{-1}) with Amide A (3300 cm^{-1}) results in a band near 4850 cm^{-1}.[12,41,50] Another band appearing near 4590 cm^{-1} has been attributed to several possible sources, including the first overtone of the Amide I band (1650 cm^{-1}) combined with the group frequency vibration at 1250 cm^{-1}.[37] However, since this part of the LWNIR is dominated by features arising from vibrations involving 2 quanta of excitation, a more likely assignment is to the combination of CH stretching (near 2900 cm^{-1}) and the Amide I vibration. The detectors available in this wavelength region are similar to those listed above, with the addition of InAs and PbS detectors.[49] Working in the LWNIR and shorter wavelength regions allows the use of glass and quartz optics, which are much less expensive and more readily available than IR specific optics.[37]

Going to higher frequencies in the SWNIR region (5000 – 7000 cm^{-1}), the strength of protein absorption should be further diminished, the depth of penetration of light into fabric is increased, and calibration for blood on fabrics is increasingly difficult because both the strength and the distinctiveness of the protein spectrum is reduced. The first overtone of the CH_2 stretching or combination of anti-symmetric and symmetric stretches of this group appears around 5800 cm^{-1}. The first overtone of the Amide A vibration gives rise to weak bands in the region of 6500 cm^{-1} that are difficult to see in our spectra.[41,50] Though the spectral features in the SWNIR might be weak, this wavelength offers the opportunity to work with glass optics and detectors that are faster and less noisy than traditional IR detectors. SiGe detectors[49] and small germanium charge coupled devices[51] can extend to 6000 cm^{-1}, but both have high dark

currents and so produce noisy spectra. InGaAs detectors can be operated at room temperature to 6000 cm^{-1}, and perhaps further, though with degraded performance. The IR imaging system introduced above operates in the 700 – 1300 cm^{-1} region of the IR spectrum using a microbolometer array detector. To compare this instrument to other blood detection techniques and regions of the IR spectrum, we are interested in exploring the possible limits of this instrument using a more traditional technique, in this case a bench-top FTIR.

5.4. CALIBRATION RESULTS

Figures 5.5 – 5.8 show the spectra of blood on acrylic, cotton, nylon, and polyester fabrics. Figures 5.5 – 5.7 and Table 5.1 show the results of PLSR calibrations for blood on acrylic, cotton, and polyester; no valid calibrations were found for blood on nylon fabric due to the similarity between the IR spectra of blood and nylon. The bar graphs of Fig. 5.5 – 5.7 show the calibration results in each wavelength region in terms of dilution factor (left axis) and mass percent blood solids (right axis), with grey bars indicating calibrations with an RPD < 3 and black bars indicating calibrations with an RPD ≥ 3. When the entire spectrum is used in the calibration, the best DL is found for blood on acrylic at 930x dilute (0.047% w/w blood). The DL for blood on polyester is the next best at 610x dilute (0.050% w/w blood). The DL for blood on cotton is a bit worse at 500x dilute (0.066% w/w blood). While the DL for polyester in terms of dilution factor is two-thirds that of acrylic, the DL in terms of mass percent shows that the two DLs by this metric are quite close to one another. This is likely because polyester has a lower surface area per unit mass of fabric, meaning that dip-coating both

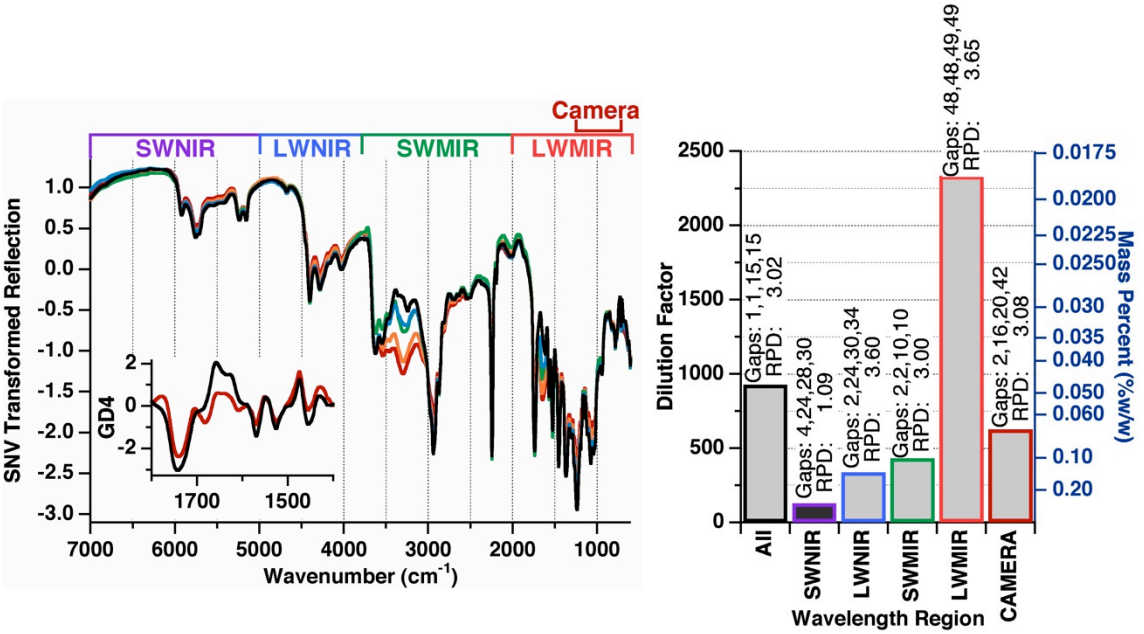

Fig. 5.5: (a) Spectra of blood on acrylic and (b) calibration results. The spectra in (a) are acrylic fabric dip-coated from water (black), or blood diluted by a factor of 25 (red), 50 (orange), 100 (green), or 200 (blue). The inset is the mean derivative spectrum of the 25x dilute coated samples (red) and uncoated fabric (black) under the optimum conditions (LWMIR region).

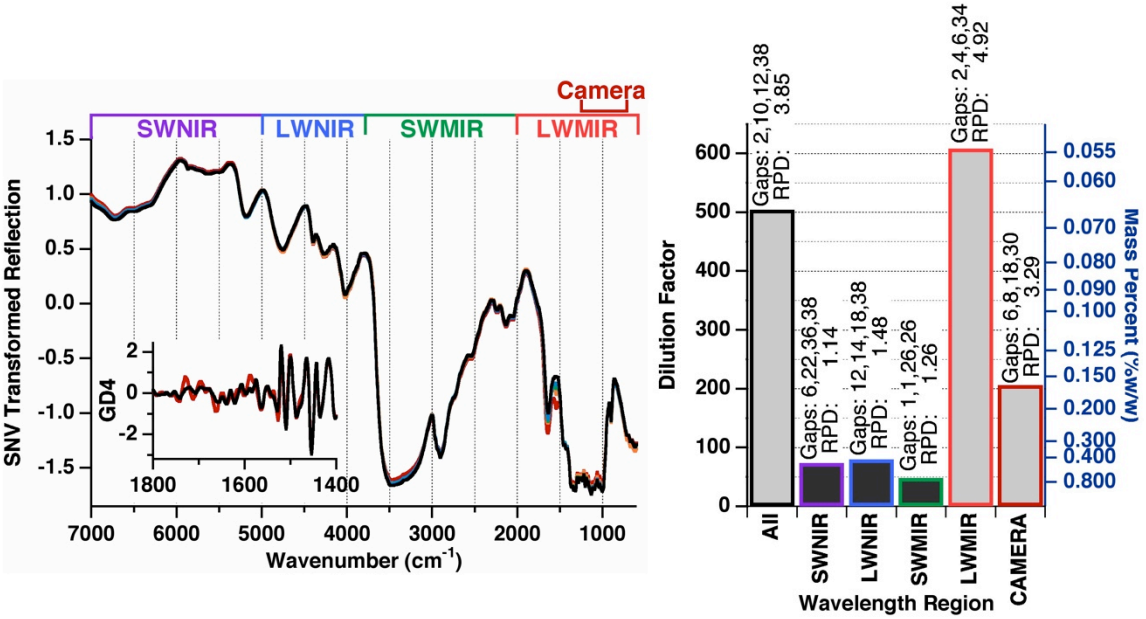

Fig. 5.6: (a) Spectra of blood on cotton and (b) calibration results. The spectra in (a) are cotton fabric dip-coated from water (black), or blood diluted by a factor of 25 (red), 50 (orange), 100 (green), or 200 (blue). The inset is the mean derivative spectrum of the 25x dilute coated samples (red) and uncoated fabric (black) under the optimum conditions (LWMIR region).

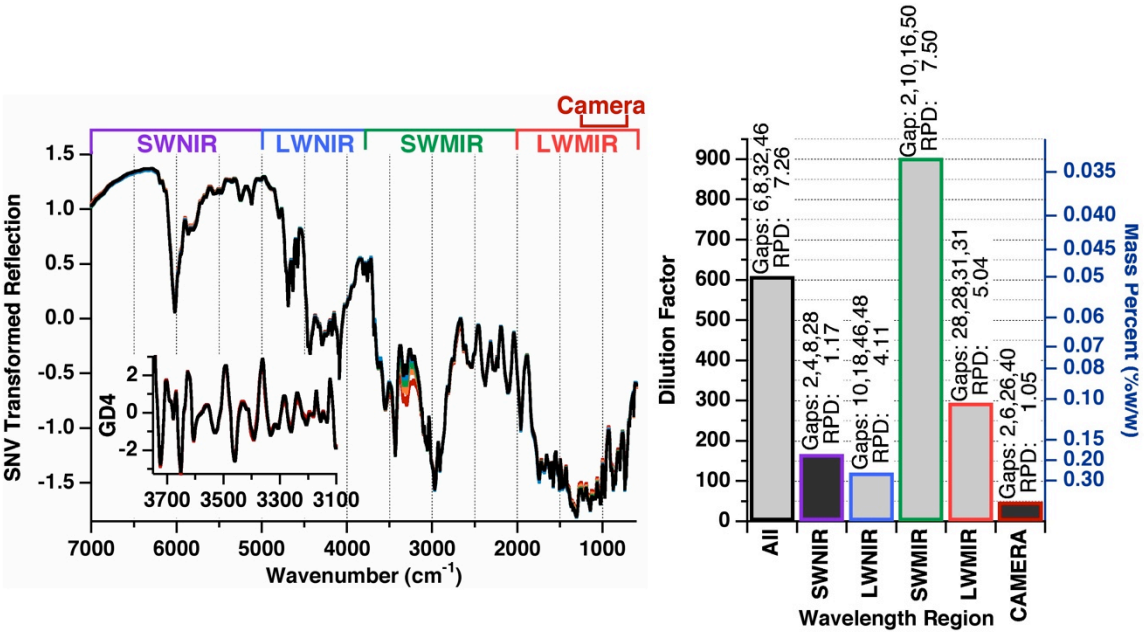

Fig. 5.7: (a) Spectra of blood on polyester and (b) calibration results. The spectra in (a) are polyester fabric dip-coated from water (black), or blood diluted by a factor of 25 (red), 50 (orange), 100 (green), or 200 (blue). The inset is the mean derivative spectrum of the 25x dilute coated samples (red) and uncoated fabric (black) under the optimum conditions (SWMIR region).

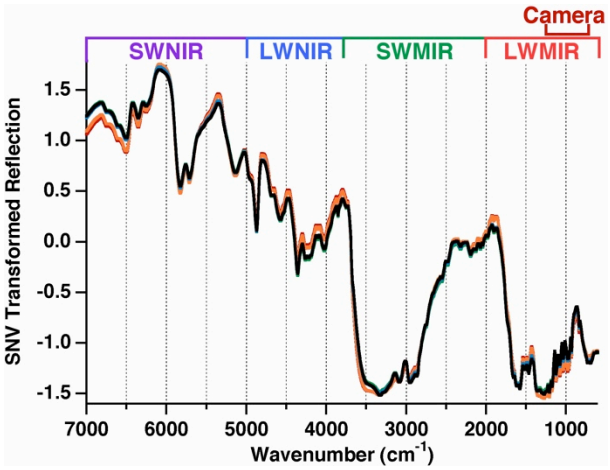

Fig. 5.8: Spectra of blood on nylon fabric. The SNV transformed spectra nylon fabric dip-coated from water (black), or blood diluted by a factor of 25 (red), 50 (orange), 100 (green), or 200 (blue).

Table 5.1: DLs for blood on fabric in different spectral regions expressed as mass percentage (%w/w), dilution factor, coverage (μg/cm^2), and film thickness (nm).

Spectral Region	Blood on Acrylic	Blood on Cotton	Blood on Polyester
All	0.047%w/w 930x 14 μg/cm^2 1.3 nm	0.066%w/w 500x 17 μg/cm^2 0.53 nm	0.050%w/w 610x 6.2 μg/cm^2 6.5 nm
SWNIR	0.34 130x 100 9.3	0.45 74x 110 3.6	0.18 170x 23 24
LWNIR	0.13 340x 39 3.5	0.41 80x 100 3.4	0.25 120x 31 33
SWMIR	0.10 430x 31 2.8	0.69 48x 170 5.6	0.034 900x 4.2 4.4
LWMIR	0.019 2300x 5.7 0.51	0.054 610x 14 0.44	0.10 300x 13 13
Camera	0.069 630x 21 1.91	0.16 210x 41 1.3	0.62 49x 77 80

polyester and acrylic fabrics from an equivalent solution results in fewer blood solids deposited on polyester samples. This demonstrates the importance of relating DLs in terms other than dilution factor to make meaningful comparisons.

To confirm the DLs, three samples were dip-coated from DI water as new blanks, and three samples were dip-coated from blood diluted near the best DL for each fabric: 2000x for acrylic, 400x for cotton, and 800x for polyester. Ten measurements were made for each sample. Predictions for all fabrics were above the DL the extent expected compared to fresh blanks (Table 5.2).

5.4.1. Acrylic Valid calibrations for blood on acrylic fabric were found in all wavelength regions except the SWNIR wavelength region where one might expect to see only weak overtone and combination bands (Fig. 5.5). The best calibration was found in the LWMIR region, where calibrations are based on the presence of the Amide I and II bands of proteins. The DL in this region is 2300x dilute (0.019% w/w blood solids). Of 30 spectra collected at 2000x dilute, 15 resulted in a signal above the DL. In the case of acrylic fabric, the Amide I and II absorption bands appear in regions of the spectrum where acrylic has relatively high reflection. Further, the protein bands here are broader than the acrylic bands. In a case like this, derivative processing of the data works well to emphasize those broader bands, optimizing at a large gap size that reduces narrow features relative to the broad features, thus improving the calibration. In some respects, it is surprising that the Amide I and II peaks result in a calibration that is much better than the Amide A/B region because the protein spectral features centered at 3300 cm^{-1} are located at a reflectance maximum

Table 5.2: DL confirmation results.

Fabric	Wavelength Region	Detection Limit	Concentration	False Positive	True Positive
Acrylic	LWMIR	2300x	2000x	2	15
Cotton	LWMIR	610x	400x	2	29
Polyester	SWMIR	900x	800x	2	20

for the acrylic fabric, resulting in clearly visible blood absorption bands at each dilution. The most-likely reason that this does not result in the expected excellent PLSR calibration is that the spectra in this region are particularly nonlinear (Fig. 5.1). As the amount of blood solids on the surface increases, the protein absorption deepens and shifts position (Fig. 5.5). This shift requires more LVs to model the features. As LVs are added, though, the model becomes increasingly susceptible to noise and the calibration worsens as a result.

5.4.2. Cotton While the Amide I, Amide II, and Amide A bands all appear in the spectrum of acrylic, only the Amide I and II bands appear in the spectrum of cotton (Fig. 5.6). The protein Amide A band is obscured by the strong hydroxyl absorption of the cotton fabric. As a result, cotton only achieves a good calibration in the LWMIR and camera regions (in addition to the full spectrum calibration that includes the LWMIR region). In the LWMIR, the Amide II band of blood solids on cotton is very distinct, while the Amide I overlaps a moderate absorption band in the cotton spectrum.

The difference spectrum between the clean fabric spectrum and that of the fabric with blood solids, however, shows that the Amide I is still present and strong. The relative location of these two absorptions allows a good calibration for blood solids on cotton with a DL of 610x dilute (0.055% w/w blood solids). Twenty-nine of the 30 spectra collected at 400x resulted in a signal above the DL.

5.4.3. Polyester In contrast to cotton, the Amide A band is a prominent feature in the spectrum of blood solids on polyester fabric, though this feature is

less prominent here than it is in the spectrum of blood solids on acrylic (Fig. 5.7). This diminished prominence works to our advantage because the behavior of the Amide A absorption becomes more linear in this case. The increased linearity in the relationship between the Amide A band and the concentration of blood leads to a better calibration. In the case of polyester, this region results in the best DL at 900x dilute, or 0.034% w/w blood solids. Of the 30 spectra collected at 800x dilute, 20 resulted in signals above the DL. Valid calibrations were found for blood on polyester in both the LWMIR and the LWNIR regions, though these calibrations result in DLs about 3x and 10x worse, respectively, than that of the SWMIR region. While the Amide I and II bands are just visible in the LWMIR region upon inspection, the polyester spectrum is congested in that region, interfering with the blood bands and preventing the determination of low DLs.

5.4.4. Nylon No valid calibrations for blood on nylon fabric have been found to date. This calibration is difficult because nylon is a polyamide, meaning that it has strong amide absorption where one would expect to find the characteristic protein bands discussed in the manuscript. This similarity in IR spectra complicates discrimination of the blood coating from the fabric matrix. In Fig. 5.8, most spectral differences can be attributed to a change in surface reflection of nylon due to the presence of a coating rather than spectral changes due to the absorption profile of blood solids. However, two sets of spectra separate more distinctly from one another near 3400 – 3700 cm-1. At these wavelengths, the average spectra of uncoated nylon, 200x dilute blood on nylon, and 100x dilute blood on nylon separate from the average spectra of 25x and 50x dilute blood on

nylon. This region falls along the high frequency side of the Amide A band, which suggests the possibility for discrimination using these wavelengths with DLs near 50x dilute (0.52% w/w).

5.4.5. Comparing DLs with other methods Even when the application of the analyte solution is well-controlled, substrates, particularly fabrics, exhibit different deposition characteristics (Fig. 5.2 – 5.3). This substrate dependence is particularly important when comparing absorbent and non-absorbent substrates; several authors have reported an order of magnitude difference in DL in dilution factor units between blood deposited on these substrate types using luminol.[28-29,32] To facilitate DL comparison between IR spectroscopy and luminol, we have calculated DLs in units of weight percent, coverage, and film thickness. Literature luminol DLs in units of dilution factor can be approximately converted to other units if the volume of blood deposited is reported (which is typical) and if the spot size of the stain is known (which is rare). The mass of blood solids in a volume of dilute blood can be approximated by first using the specific gravity of blood (1.0595 mg/μL)[52] to estimate the mass of dilute blood added to the substrate, roughly 20% of which is blood solids,[53] providing an estimate for the mass of blood added to the substrate. For diluted blood, the mass must be divided by the dilution factor. The coverage can then be approximated if the area of the spot size is known. To obtain a rough estimate for the spot size formed by adding a given volume of diluted blood, we used the values reported by van Dalen[7] for a 300 μL addition of blood on cotton fabric, and spot sizes for 50 μL and 100 μL additions of blood on cotton prepared in our lab. (For more information, see Fig.

5.9, Table 5.3) Given the uncertainties of fabric types, weaves, etc., our DLs in terms of coverage, mass percent and film thickness for literature results can only be approximate.

Table 5.4 displays some DLs reported for the detection of blood on cotton fabric and filter paper using luminol and IR presumptive tests. The most conservative value reported for a luminol DL is 100x dilution by Budowle et al.[32] However, that study focused on the effects of presumptive tests on DNA recovery rather than the determination of DLs, so the experiment was not optimized for DLs. At the other extreme, the DL of ≥ 5,000,000x (≤ 0.40 ng solids/cm^2) dilution on cotton fabric stands apart not just by its value, but also its method: the authors used a hemoglobin solution rather than diluted whole blood.[1] The luminol test is catalyzed by iron in the sample, and this concentration of blood solids corresponds to fewer than 20 fmol of iron per cm^2 of fabric.
The most commonly reported DL for blood on cotton is the intermediate value of 1000x dilution.[28-31,54] In the work presented here, the best DL for blood on cotton using diffuse reflection is 610x (14 μg/cm^2, Table 5.1), which is on the order of the luminol DLs reported at 1000x dilute (2.0 μg/cm^2).

5.5. CONCLUSIONS

Overall, the LWMIR and SWMIR regions offered the best spectroscopic calibrations for blood on fabrics because those regions contain the characteristic bands of protein absorption. The LWNIR region offers some discrimination due to the appearance of overtones and combination bands, but these calibrations were less good in general. While the SWMIR and LWMIR regions offer the most

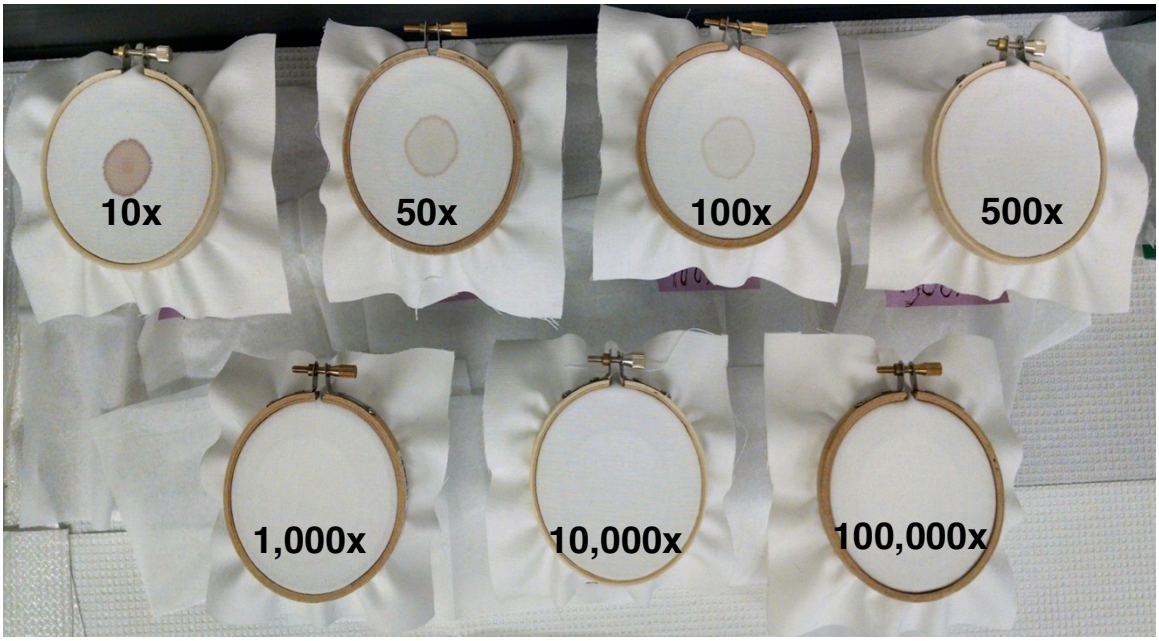

Fig. 5.9: 50 µL of 10x; 50x; 100x; 1,000x; 10,000x; and 100,000x diluted blood deposited on 100% white cotton. Samples were prepared by securing 100% white cotton in an embroidery hoop to keep it level, then placing the fabric across a beaker to prevent the fluid from interacting with the supporting surface as it spreads through the fabric. Each stain was made by adding one 50 µL drop of dilute blood to the fabric from a micropipette. Two things are apparent from the picture: dilutions greater than 500x are not easily visible on the cloth, and the area of blood stains increases with dilution factor. Spot sizes corresponding to these samples are recorded in Table 5.3.

Table 5.3: Blood stain area.

		Area (cm2)		
Dilution Factor	1/Dilution Factor	300 µL Drop	100 µL Drop	50 µL Drop
0	1	17.8	4.8	--
2	0.5	22.5	--	--
10	0.1	29.7	7.4	4.2
50	0.02	--	--	5.0
100	0.01	33.1	9.0	5.3

Fig. 5.9 describes spot size estimation for 50 µL drops. Estimates for the 100 µL drop sizes were obtained similarly for whole blood, 10x dilute blood, and 100x dilute blood. Values for the 300 µL stains are reported by van Dalen.[7] Dashed lines indicate that the value was not obtained. Because stain area increases with dilution factor (consistent with the results reported by van Dalen), we used the area of the 100x stain to give an area estimate for higher dilutions, understanding that this slightly over-estimates the coverage for higher dilutions. These values are used to estimate the coverages reported in manuscript Tables I and II.

Table 5.4: Comparison of literature DLs.

Number	Reference	Substrate	Deposited Volume of Dilute Blood[a]	Reported DL (Dilution Factor)	Estimated DL (μg/cm^2)
Detection by Luminol					
1[b]	Budowle et al.[32]	Denim, leather, and carpet	100 μL	1:100	24
2	Middlestead and Thornton[30]	100% Cotton (Denim)	Two 200 μL aliquots[e]	> 1:1000[d]	3.3
3	Garofano et al.[54]	Cotton	100 μL	1:1,000	2.4
4[c]	Patel and Hopwood[29]	Cotton	50 μL	1:1000	2.0
5[c]	Seashols et al.[28]	100% Cotton	50 μL	1:1000	2.0
		100% Nylon		1:1000	--
6	Finnis et al.[31]	Cotton	50 μL	1:1000	2.0
7	Grispino[55]	Cotton	100 μL	1:10,000	0.24
8	Lytle and Hedgecock[56]	Filter Paper	Soaked in dilute blood	1:10,000	--
9[c]	Tobe et al.[57]	Filter Paper	Soaked 1 cm^2 pieces in dilute	1:100,000	--
10	Castello et al.[58]	Cotton	5 drops (~250 μL)	1:300,000	0.0053
11[f]	Webb et al.[1]	100% Cotton	50 μL dilute hemoglobin	>1:5,000,000[d]	0.00040
			Soaked 16 cm^2 in dilute hemoglobin	>1:5,000,000[d]	0.0017
12[g]	Grodsky et al.[59]	Filter Paper	Soaked in dilute blood	>1:5,000,000[d]	--
Detection by IR					
13[h]	van Dalen[7]	Cotton	300 μL	1:5.3	17,000
14[i]	Lin et al.[11]	100% Cotton	20 μL	1:8	130
15[i]	Finnis et al.[3]	Cotton	50 μL	1:10	250
16	DeJong et al. (from Table I)	Cotton	Dip-Coating	1:610	14
		Acrylic		1:2300	6.0
		Polyester		1:900	4.2

[a]Where a volume is listed, a drop of diluted blood at that volume was deposited on the substrate. For sources except van Dalen[7], the reported DLs are qualitative. The best DL in studies comparing luminol formulations is recorded here. The coverage values (μg/cm^2) in the final column are estimated as described in the text. Readers are referred to the sources for experimental details. [b]Reporting DLs was not the goal of this work. The report says: “stains on

absorbent surfaces were detectable usually at no more than a 1:100 dilution".[c]Studies compare luminol formulations. In Patel and Hopwood, some formulations detected blood at higher dilutions. The DL of 1:1000 reflects a dilution that resulted in a consistent positive response across formulations and replicate samples. [d]The DL reported is the greatest dilution investigated in these studies. [e]Each 200 µL aliquot is deposited in the form of a letter (approx. 2" x 1"), rather than a drop. [f]Webb et al. deposited diluted hemoglobin solutions rather than diluted blood. DLs are given with dilution relative to the concentration of hemoglobin in blood (reported by the authors as 150 g/L). [g]The deposited blood was not allowed to dry. All other stains were allowed to dry for some period of time prior to analysis. [h]This report uses a FTIR-ATR system (650 – 4000 cm^{-1}) to estimate a quantitative DL, reported as %N. This can be used to determine the relative concentration of blood and, by extension, coverage. The DL in terms of dilution factor is estimated from this. [i]The IR system is a visible camera modified to collect NIR light from 760 – 1500 nm (13158 – 6667 cm^{-1}).

discrimination for blood, there are more constraints on the instrumentation. Conversely, the SWNIR offers promise in terms of ease of instrumentation design and construction, but no valid calibrations were found in this region based on the RPD criterion employed. In the camera wavelength region, DLs for acrylic and cotton were 630x dilute (0.070% w/w blood) and 140x dilute (0.23% w/w blood), respectively. Valid DLs for blood on polyester in this region were not found, primarily due to the high absorption of polyester in the same wavelength region.

REFERENCES

(1) J. L. Webb, J. I. Creamer, T. I. Quickenden. “A comparison of the presumptive luminol test for blood with four non-chemiluminescent forensic techniques”. Luminescence. 2006. 21(4): 214-220.

(2) K. Virkler, I. K. Lednev. "Analysis of body fluids for forensic purposes: From laboratory testing to non-destructive rapid confirmatory identification at a crime scene". Forensic Sci. Int. 2009, 188(1): 1-17.

(3) T. I. Quickenden, J. I. Creamer. "A study of common interferences with the forensic luminol test for blood". Luminescence 2001, 16(4): 295-298.

(4) F. Barni, S. W. Lewis, A. Berti, G. M. Miskelly, G. Lago. "Forensic application of the luminol reaction as a presumptive test for latent blood detection". Talanta 2007. 72(3): 896-913.

(5) T. Larkin, C. Gannicliffe. "Illuminating the health and safety of luminol". Sci. Justice 2008, 48(2): 71-75.

(6) J. P. de Almeida, N. Glesse, C. Bonorino. "Effect of presumptive tests reagents on human blood confirmatory tests and DNA analysis using real time polymerase chain reaction". Forensic Sci. Int. 2011, 206(1): 58-61.

(7) G. van Dalen. "Protein on Cloths: Evaluation of Analytical Techniques". Appl. Spectrosc. 2000, 54(9): 1350-1356.

(8) A. Farrar, G. Porter, A. Renshaw. "Detection of Latent Bloodstains Beneath Painted Surfaces Using Reflected Infrared Photography". J. Forensic Sci. 2012, 57(5): 1190-1198.

(9) M. A. Raymond, R. L. Hall. "An Interesting Application of Infrared Reflection Photography to Blood Splash Pattern Interpretation". Forensic Sci. Int. 1986, 31(3): 189-194.

(10) M. Perkins. "The Application of Infrared Photography in Bloodstain Pattern Documentation of Clothing". J. Forensic Ident. 2005, 55(1): 1-9.

(11) A. C. Lin, H. Hsieh, L. Tsai, A. Linacre, J. C. Lee. "Forensic applications of infrared imaging for the detection and recording of latent evidence". J. Forensic Sci. 2007, 52(5): 1148-1150. J. T. Kuenstner, K. Norris, V. F.

Kalasinsky. "Spectrophotometry of Human Hemoglobin in the Midinfrared Region". Biospectroscopy 1997, 3: 225-232.

(12) J. T. Kuenstner, K. H. Norris, W. F. McCarthy. "Measurement of Hemoglobin in Unlysed Blood by Near-Infrared Spectroscopy". Appl. Spectrosc. 1994, 48(4): 484-488.

(13) Y. Liu, R. Cho, K. Sakurai, T. Miura, Y. Ozaki. "Studies on Spectra-Structure Correlations in Near-Infrared Spectra of Proteins and Polypeptides .1. A Marker Band for Hydrogen-Bonds". Appl. Spectrosc. 1994, 48(10): 1249-1254.

(14) E. Botonjic-Sehic, C. W. Brown, M. Lamontagne. M. Tsaparikos. "Forensic Application of Near-Infrared Spectroscopy: Aging of Bloodstains". Spectroscopy 2009, 24(2): 42-48.

(15) G. Edelman, V. Manti, S. M. van Ruth, T. van Leeuwen, M. Aalders. "Identification and age estimation of blood stains on colored backgrounds by near infrared spectroscopy". Forensic Sci. Int. 2012, 220(1): 239-244.

(16) M. R. Pearl, H. Brooke, J. N. McCutcheon, S. L. Morgan, M. L. Myrick. "Coating Effects on Mid-Infrared Reflection Spectra of Fabrics". Appl. Spectrosc. 2011, 65(8): 876-884.

(17) N. M. Morris. "A Comparison of Sampling Techniques for the Characterization of Cotton Textiles by Infrared-Spectroscopy". Text. Chem. Color. 1991, 23(4): 19-22.

(18) S. Ghosh, M. D. Cannon, R. B. Roy. "Quantitative-Analysis of Durable Press Resin on Cotton Fabrics Using near-Infrared Reflectance Spectroscopy". Text. Res. J. 1990, 60(3): 167-172.

(19) C. Gilbert, S. Kokot. "Discrimination of Cellulosic Fabrics by Diffuse-Reflectance Infrared Fourier-Transform Spectroscopy and Chemometrics". Vib Spectrosc. 1995, 9(2): 161-167.

(20) C. Gilbert, S. Kokot, U. Meyer. "Application of Drift Spectroscopy and Chemometrics for the Comparison of Cotton Fabrics". Appl. Spectrosc. 1993, 47(6): 741-748.

(21) S. Kokot, K. Crawford, L. Rintoul, U. Meyer. "A DRIFTS study of reactive dye states on cotton fabric". Vib. Spectrosc. 1997, 15(1): 103-111.

(22) H. M. Heise, R. Kuckuk, A. Bereck, D. Riegel. "Mid-infrared diffuse reflectance spectroscopy of textiles containing finishing auxiliaries". Vib. Spectrosc. 2004, 35(1): 213-218.

(23) H. M. Heise, R. Kuckuk, U. Damm, A. Bereck, D. Riegel. "Quantitative diffuse reflectance infrared spectroscopy of cotton fabrics treated with a cyclodextrin derivative finishing auxiliary". J. Mol. Struct. 2005, 744: 877-880.

(24) H. Brooke, M. R. Baranowski, J. N. McCutcheon, S. L. Morgan, M. L. Myrick. "Multimode Imaging in the Thermal Infrared for Chemical Contrast Enhancement. Part 1: Methodology". Anal. Chem. 2010, 82(20): 8412-8420.

(25) H. Brooke, M. R. Baranowski, J. N. McCutcheon, S. L. Morgan, M. L. Myrick. "Multimode Imaging in the Thermal Infrared for Chemical Contrast Enhancement. Part 2: Simulation Driven Design". Anal. Chem. 2010, 82(20): 8421-8426.

(26) H. Brooke, M. R. Baranowski, J. N. McCutcheon, S. L. Morgan, M. L. Myrick. "Multimode Imaging in the Thermal Infrared for Chemical Contrast Enhancement. Part 3: Visualizing Blood on Fabrics". Anal. Chem. 2010, 82(20): 8427-8431.

(27) S. J. Seashols, H. D. Cross, D. L. Shrader, A. Rief. "A Comparison of Chemical Enhancements for the Detection of Latent Blood". J. Forensic Sci. 2013, 58(1): 130-133.

(28) G. Patel, A. Hopwood. "An evaluation of luminol formulations and their effect on DNA profiling". Int. J. Legal Med. 2013, 127(4): 723-729.

(29) C. Middlestead, J. Thornton. "Sensitivity of the Luminol Test with Blue Denim". J. Forensic Sci. 2010, 55(5): 1340-1342.

(30) J. Finnis, J. Lewis, A. Davidson. "Comparison of methods for visualizing blood on dark surfaces". Sci. Justice. 2013, 53(2): 178-186.

(31) B. Budowle, J. L. Leggitt, D. A. Defenbaugh, K. M. Keys, S. F. Malkiewicz. "The presumptive reagent fluorescein for detection of dilute bloodstains and subsequent STR typing of recovered DNA". J. Forensic Sci. 2000, 45(5): 1090-1092.

(32) S. Boyd, M. F. Bertino, S. J. Seashols. "Raman spectroscopy of blood samples for forensic applications". Forensic Sci. Int. 2011, 208(1): 124-128.

(33) S. Boyd, M. F. Bertino, D. Ye, L. S. White, S. J. Seashols. "Highly Sensitive Detection of Blood by Surface Enhanced Raman Scattering". J. Forensic Sci. 2013, 58(3): 753-756.

(34) T. Peters. "Serum-Albumin". Adv. Protein Chem. 1985, 37: 161-245.

(35) S. A. DeJong, W. L. O'Brien, Z. Lu, B. M. Cassidy, S. L. Morgan, M. L. Myrick. "optimization of Gap Derivatives for Measuring Blood Concentration of Fabric Using Vibrational Spectroscopy". Appl. Spectrosc. 2015, 69(6): 733-748.

(36) P. C. Williams. "Implementation of Near-Infrared Technology". In P. C. Williams, K. H. Norris, editors. Near-Infrared Technology in the Agricultural and Food Industries. St. Paul, MN: American Association of Cereal Chemists, 2001. Ch. 8, Pp 145-170.

(37) L. A. Currie. "Nomenclature in Evaluation of Analytical Methods Including Detection and Quantification Capabilities". Pure Appl. Chem. 1995, 67(10): 1699-1723.

(38) R. Boqué, F. X. Rius. "Multivariate dection limits estimators". Chemom. Intell. Lab. Syst. 1996, 32: 11-23.

(39) J. F. Fuzek. "Absorption and Desorption of Water by Some Common Fibers". Ind. Eng. Chem. Prod. Res. Dev. 1985, 24(1): 140-144.

(40) K. T. Hecht, D. L. Wood. "The near Infra-Red Spectrum of the Petide Group". Proc. R. Soc. A. 1956, 235(1201): 174-188.

(41) H. Sternglanz. "Using Water as an Infrared Solvent". Appl. Spectrosc. 1956, 10(2): 77-82.

(42) D. E. McCarthy. "The Reflection and Transmission of Infrared Materials: III. Spectra from 2-50 Microns". Appl. Opt. 1965, 4(3): 317-320.

(43) D. E. McCarthy. "The Reflection and Transmission of Infrared Materials: IV, Bibliography". Appl. Opt. 1965, 4(4): 507-511.

(44) D. E. McCarthy. " The Reflection and Transmission of Infrared Materials V: Spectra from 2 - 50 microns". Appl. Opt. 1968, 7(10): 1997-2000.

(45) D. E. McCarthy. "The Reflection and Transmission of Infrared Materials. VI: Bibliography". Appl. Opt. 1968, 7(11): 2221-2225.

(46) D. E. Mccarthy. " The Reflection and Transmission of Infrared Materials .1. Spectra from 2-50 Microns". Appl. Opt. 1963, 2(6): 591-595.

(47) D. E. Mccarthy. "The Reflection and Transmission of Infrared Materials .2. Biliography". Appl. Opt. 1963, 2(6): 596-603.

(48) N. K. Dhar, R. Dat, A. K. Sood. "Advances in Infrared Detector Array Technology". In S. L. Pyshkin, J. M. Ballato, editors. Optoelectronics - Advanced Materials and Devices. InTech, 2013.

(49) A. J. Sadler, J. G. Horsch, E. Q. Lawson, D. Harmatz, D. T. Brandau, C. R. Middaugh. "Near-Infrared Photoacoustic-Spectroscopy of Proteins". Anal. Biochem. 1984, 138(1): 44-51.

(50) J. R. Janesick. *Scientific charge-coupled devices.* Beelingham: SPIE - The International Society for Optical Engineering, 2001. Pp. 25-28.

(51) D. D. van Slyke, R. A. Phillips, V. P. Dole, P. B. Hamilton, R. M. Archibald, J. Plazin. J. Biol. Chem. 1950, 183(1): 349-360.

(52) J. M. Dust, C. M. Grieshop, C. M. Parsons, L. K. Karr-Lilienthal, C. S. Schasteen, J. D. Quigley, N. R. Merchen, G. C. Fahey. "Chemical composision, protein quality, palatability, and digestibility of alternative protein sources for dogs". J. Anim. Sci. 2005, 83(10): 2414-2422.

(53) L. Garofano, M. Pizzamiglio, A. Marino, A. Brighenti, F. Romani. " A comparative study of the sensitivity and specifity of luminal and fluorescein on diluted and aged bloodstains and subsequent STRs typing". Int. Congr. Ser. 2006, 1288: 657-659.

(54) R. R. J. Grispino. "The Effect of Luminol on the Serological Analysis of Dried Human Bloodstains". Crime Laboratory Digest 1990, 17(1): 13-22.

(55) L. T. Lytle, D. G. Hedgecock. "Chemiluminescence in Visualization of Forensic Bloodstains". J. Forensic Sci. 1978, 23(3): 550-562.

(56) S. S. Tobe, N. Watson, N. N. Daeid. " Evaluation of six presumptive tests for blood, their specificity, sensitivity, and effect on high molecular-weight DNA". J. Forensic Sci. 2007, 52(1): 102-109.

(57) A. Castello, M. Alvarez, F. Verdu. " Accuracy, Reliability, and Safety of Luminol in Bloodstain Investigation". Can. Soc. Forensic Sci. J. 2002, 35(3): 113-121.

(58) M. Grodsky, K. Wright, P. L. Kirk. "Simplified Preliminary Blood Testing: An Improved Technique and a Comparative Study of Methods". J. Crim. L. Criminology & Police Sci. 1951, 42: 95-104.

CHAPTER 6

INFRARED CAMERA USED TO MEASURE ELECTRODE HEATING DURING CYCLIC VOLTAMMETRY

6.1. INTRODUCTION

Understanding the processes of oxidation and reduction at electrode surfaces is important for the evaluation of new catalysts. In a perfectly reversible (and energetically favorable) reaction, the heat produced at the electrode will be exactly that related to the electrochemical reaction.[1] The heat at the electrodes exceeding the expected chemical enthalpy change can be attributed to a variety of factors, including overpotential (overcoming kinetic limitations), adorption/desorption events, Peltier heating, and non-electrochemical events at the electrode.[2] These other factors can be investigated by coupling electrochemical studies with thermographic studies.

Thermal studies of electrode processes can compliment the information about a system provided by electrochemical analyses such as cyclic voltammetry (CV) and potential step experiments. Thermography can elucidate both the enthalpy of the reaction occurring at the electrodes as well as the compounding processes noted above. Further, independently examining the thermal behavior at the cathode and anode can offer further insight to the half-reactions occurring in an electrochemical cell.[1]

In-situ calorimetry seeks to do this, and a few different methods have been reported in the literature.[2-5] One method suspended a thermocouple near the back side of the working electrode to measure temperature changes at the electrode.[2] Another developed a special electrochemical cell in which the electrodes were thermally separated from one another to measure differential temperatures.[5] These methods involved specially developed electrochemical cells to measure the temperature simultaneously with the electrochemistry, and could only monitor slow potential scan speeds, limited by response times of the thermistors and thermocouples.

This chapter demonstrates a new method to perform thermographic studies using an infrared (IR) camera to measure thermal information about the system. The heating of the back surface of an electrode has been measured as a function of current and voltage using a thermal IR camera while the front surface of the electrode remained in contact with the solution. A portion of the electrode was coated with a thermal emitter to show the influence of electrochemical reactions on the electrode thermometry. As the applied potential at the electrode is systematically varied, the resulting thermogram of the coated electrode relative to the solution or bare metal offers insight into electrode processes occurring during cyclic voltammetry.

This study offers a simpler alternative that can measure subtle temperature changes quickly, allowing deeper exploration of system changes on a time-scale relevant to the processes at the electrode. The performance of the

system was assessed using an exemplary reversible reaction: the reduction of ferricyanide to ferrocyanide, with the half-reaction:

$$Fe^{III}(CN)_6^{3-} + e^- \longrightarrow Fe^{II}(CN)_6^{4-}$$

6.2. METHOD

6.2.1. Cyclic Voltammetry The solution used to evaluate the system described in this chapter is 0.1 M $K_3Fe(CN)_6$ in 1.0 M KNO_3 supporting electrolyte. Background thermograms and voltammograms were collected of the supporting electrolyte alone. The working electrode was a 0.025 cm thick piece of platinum foil with a surface area of 1.2 cm^2. About one-half of the back of this foil (the side facing the infrared camera) was coated with a thermally emissive material (black spray paint). The counter electrode was platinum gauze. The reference electrode was a Ag/AgCl electrode.

For the cyclic voltammograms (CVs), 100 mL of the appropriate solution was added to a beaker. The working electrode was secured to the side of the beaker such that the front (un-modified) surface was in contact with the solution, but the back remained above the solution. The set-up is pictured in Fig. 6.1, with the visible image on the left and the corresponding IR image on the right. The counter electrode was placed directly across from the working, and the reference electrode was secured as near the working electrode as possible.

The CVs were collected at 4 scan rates: 100 (-0.4 – 1.0 V), 500 (-0.4 – 1.0 V), 750 (-0.8 – 1.0 V), and 1000 (-1.0 – 1.0 V) mV/s. The CVs were obtained with a Model 263 A potentiostat/galvanostat operated by PowerSuite® software (Princeton Applied Research, Oak Ridge, TN). The system was equilibrated at the starting potential for sometime before beginning the scan to enable

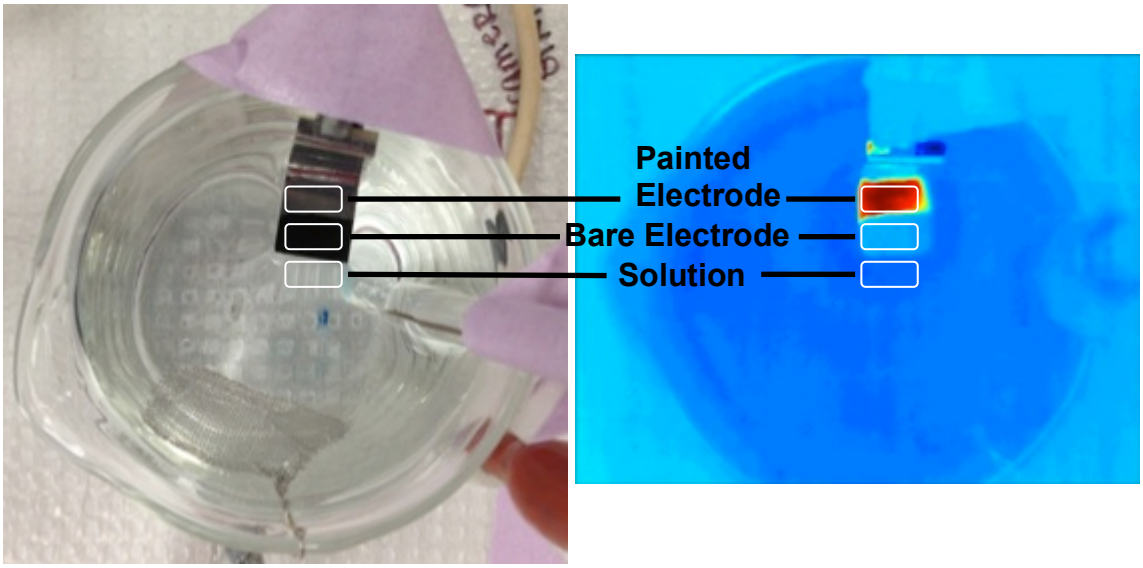

Fig. 6.1a (Left): Visible image of the experiment set-up, viewed from the top as the infrared camera views it. The boxes show the regions of the image from which the bare electrode, painted electrode, and solution data were retrieved.
Fig. 6.1b (Right): Infrared image of the experiment set-up.

synchronization with the voltage data collected through LabVIEW™. The number of cycles executed was determined by the number of frames the IR camera could collect and store consecutively (CVs are shown in Fig. 6.2).

6.2.2. Thermometry In-house LabVIEW™ software (National Instruments, Austin, TX) was used to synchronously record voltage data with images collected by a thermal IR camera (FLIR® Systems, Inc., Wilsonville, OR). The detector of this camera is an uncooled microbolometer array that is sensitive in the 7-14 μm wavelength region. The frame rate of the camera is 60 frames/sec, and 2400 frames were collected during each measurement. The pixels in the microbolometer array do not have uniform response characteristics, and as a result striation-type features can be seen in the IR images (See Fig. 6.1b). To minimize the influence of these striations on the measurement of relatively small temperature differences, the electrochemical cell was arranged so that the portions of the solution, bare electrode, and painted electrode measured fell along one striation. An analog-to-digital converter was used to record a voltage signal received from the potentiostat in LabVIEW™ so that camera frames could be related to the voltage applied to the cell.

6.2.3. Post-Processing Once the data were collected in LabVIEW™, in-house Matlab (The Mathworks, Inc., Natick, MA) routines (recorded in Appendix B). First, both the camera images and voltage data were truncated to include only full voltage cycles. Then, the voltage data output by the potentiostat were corrected to match the voltages applied to the electrochemical cell. Groups of

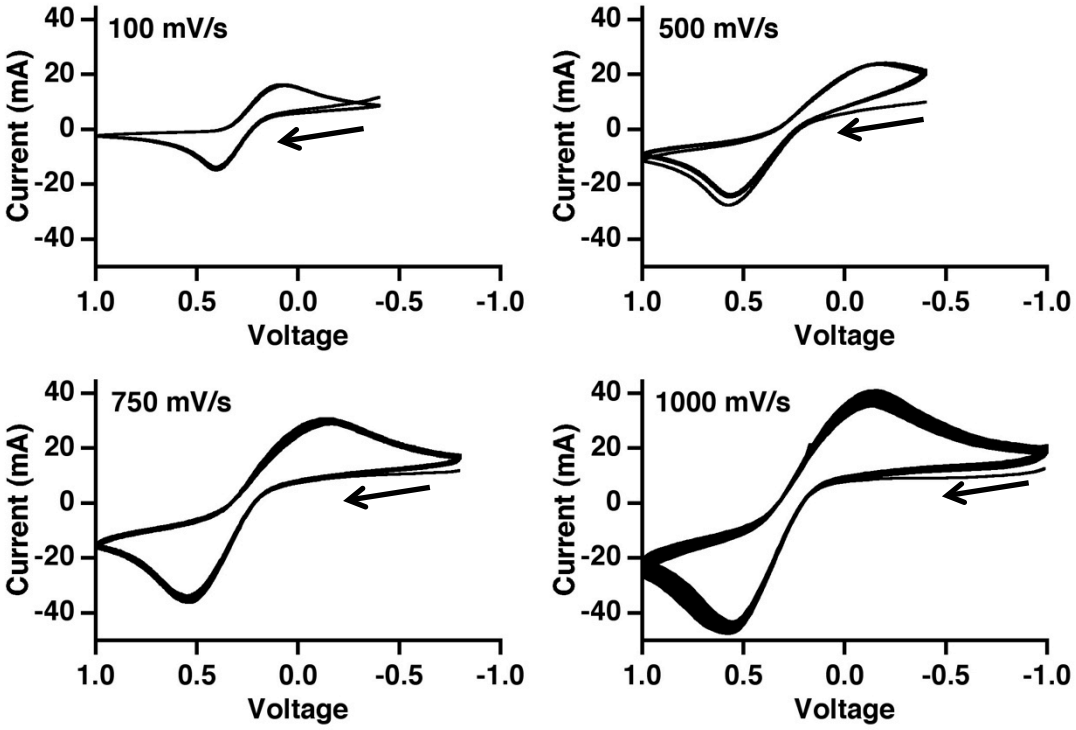

Fig. 6.2: Cyclic voltammogram of 0.1 M $K_3Fe(CN)_6$ in 1.0 M KNO_3 run at scan rates of 100 mV/s, 500 mV/s, 750 mV/s, and 1000 mV/s. Scan direction is noted with an arrow. The CVs were collected with the set-up shown in Fig. 6.1 and described in the text.

pixels of equal size were then selected to represent the painted electrode, bare electrode, and solution. The mean value of these pixel regions was used for further analysis. To show the change in temperature of the painted electrode relative to the environment (bare electrode) and system (solution), the results are shown in Fig. 6.3 – 6.4 as differences.

6.3. RESULTS AND DISCUSSION

The visible and infrared images of the electrochemical cell are shown in Fig. 6.1a and 6.1b, respectively. The three boxed areas show the bare metal electrode, the painted electrode, and the solution. The temperatures of these represent the temperature of the environment, the electrode, and the system respectively. Looking at the differences between the electrode temperature and either the environment (bare electrode, Fig. 6.3) or the system (solution, Fig. 6.4) offers insight to the heat produced at the electrode, particularly when these differences are related to the CV results.

Looking at the CV results in Fig. 6.2, we can see that as the scan rate increases, so does the current amplitude, as expected. We can also see that the separation between the peaks in current in the forward and reverse scans spread apart as the scan rate increases. This is also expected. The increase separation between the peaks suggests that this ideal reversible reaction is becoming irreversible (indicated by a separation between peaks greater than 59 mV^{1}). Consequently, we can expect that the heat generated at the electrode surface will also increase with scan rate.

We can turn our attention to Fig. 6.3 – 6.4 to examine the heat evolution. Figure 6.3 shows the relationship between the heating of the electrode and the

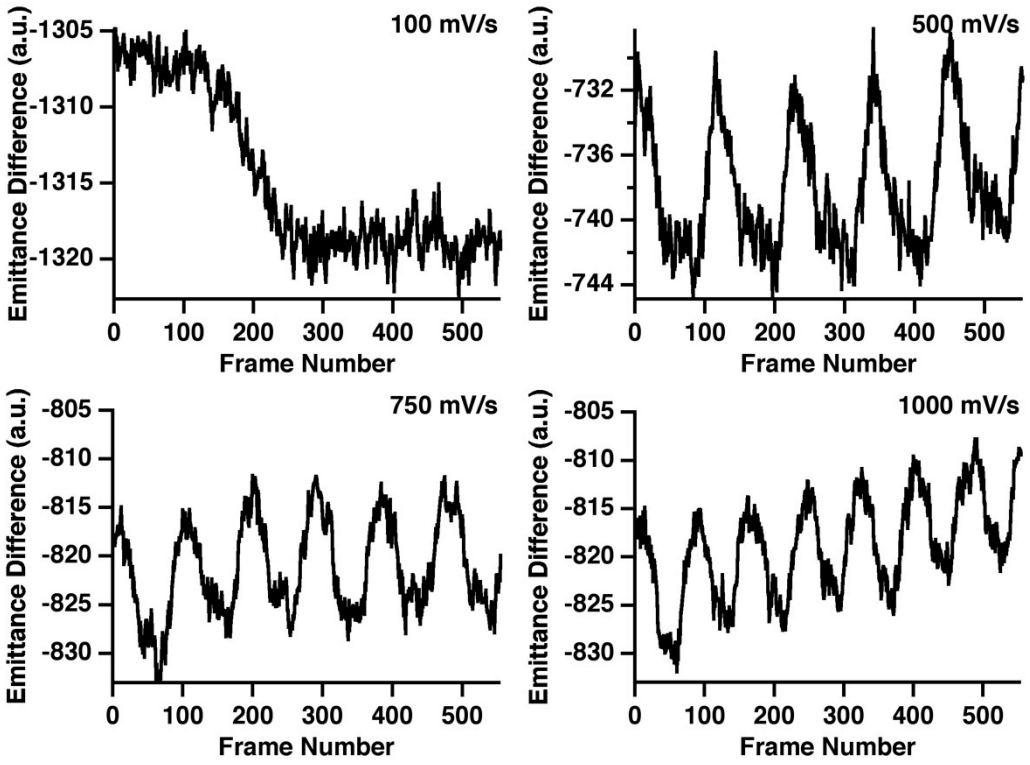

Fig. 6.3: Plot of emittance difference between the mean painted and bare metal electrode areas over the length of data collection (areas shown in Fig. 6.1). The overall upward slope shows the increase of electrode temperature with respect to the surrounding environment while the repeating higher frequency peaks correspond to cycles of voltammetry.

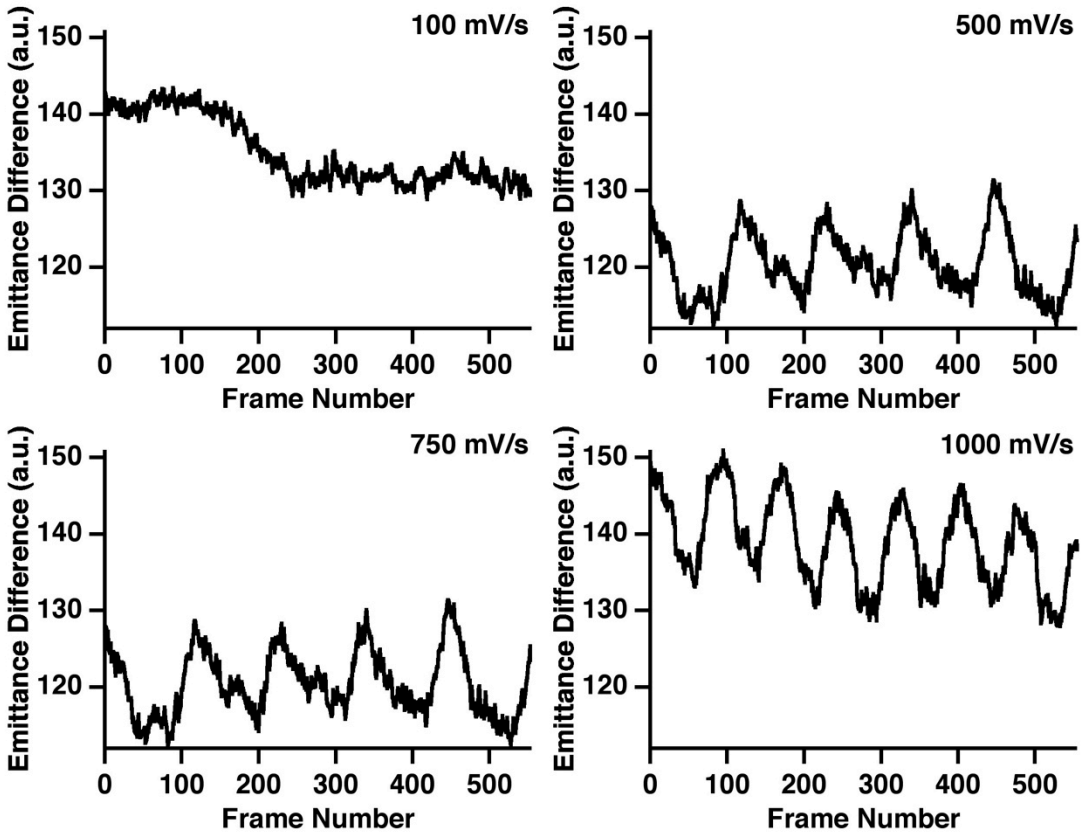

Fig. 6.4: Plot of emittance difference between the mean painted electrode and mean solution over the length of data collection (areas shown in Fig. 6.1). The recurring peaks correspond to cycles of voltammetry.

environment (bare metal electrode) from the first 500 frames collected with the IR camera corresponding to the CV. Due to the slower potential scan rate at 100 mV/s, only about one-half of a cycle is shown. The other three frames of Fig. 6.3 show multiple cycles, which gives rise to a repeatable cycle in the thermogram with a periodicity defined by the potential scan speed. Over the collection of these frames, one can also note a general trend of decreasing difference between the temperature of the electrode and the environment, which can be taken to mean that the CV experiment causes the electrode to heat over time, in addition to the temperature fluctuations related to the potential sweeps.

The difference between the painted portion of the electrode and the solution is shown in Fig. 6.4. This is perhaps a better display of the changes related to potential cycles as both the painted electrode and the solution are representative of the system being investigated. The shapes of the traces are similar to those shown in Fig. 6.3, though the painted electrode is now warmer than the solution, and the differences are more consistent across measurements. In both figures, the emittance difference between the peaks and troughs of 15 units relates to approx. 0.05^{o}C.

To better relate the temperature fluctuations to the potential, the mean thermogram (as given by the difference between the painted electrode and the solution) is shown with the average CV at each scan speed in Fig. 6.5. When the scan speed is 100 mV/s, the data are clearly noisy, however a trend is still clearly visible. As we move to higher scan speeds, the average thermogram becomes smoother, largely due to a higher number of cycles to average. While the

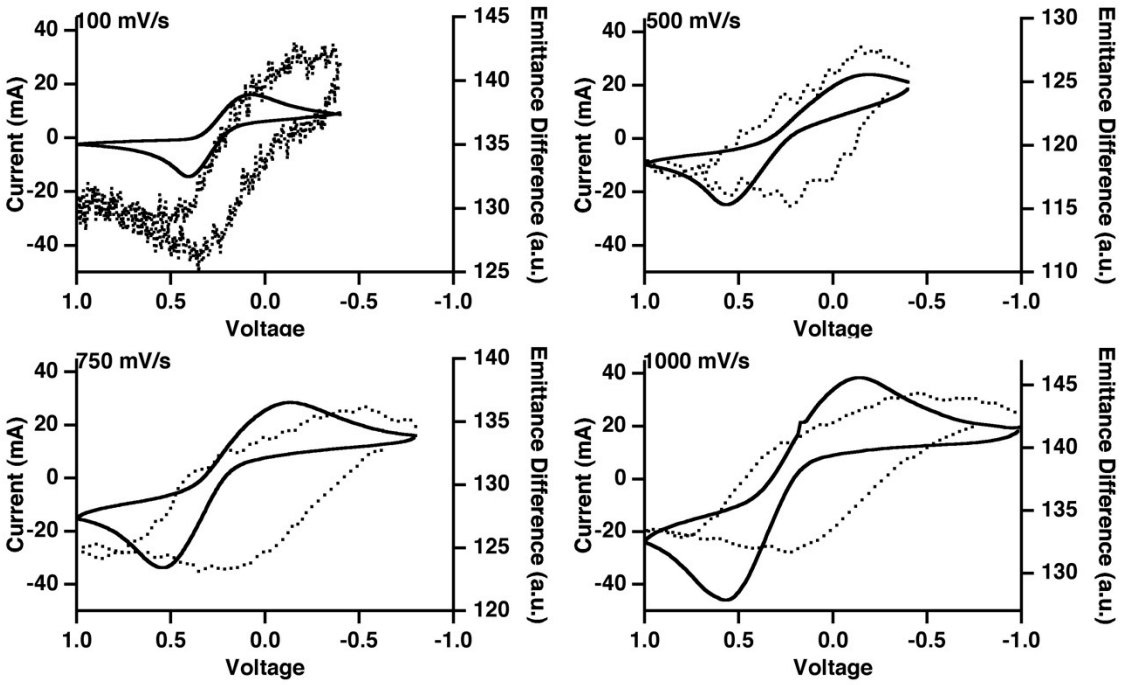

Fig. 6.5: Overlay plot of the average of voltammetry and thermometry results. Scan direction is noted with an arrow. Thermometry values are given by the difference between the painted electrode and the solution.

relationship between the CV and the thermogram is not exact, the trend follows that of the CV and demonstrates the ability of the IR camera to monitor the temperature of the working electrode in an electrochemical system.

This measurement technique allows for rapid determination of the electrode temperature in relation to the electrode heating. The back surface comes to equilibrium with the active front surface of the electrode on the order of 0.7 ms. The infrared camera can collect a frame every 17 ms. At a scan rate of 1000 mV/s, this means that there is about 17 mV blurring in the thermometry data. Thus, the camera is the limiting factor of data collection rather than equilibrium between the front and back surfaces of the electrode. The relationship between electrode thermometry and voltammetry does not appear to be directly related to current, and so may be a function of power applied to the system or the concentration profile at the electrode.

6.4. CONCLUSIONS AND FUTURE WORK

This work has shown that using an IR camera to monitor the heating of an electrode is feasible, and can work at faster scan speeds than other methods currently established in the literature. To further improve this system, the first step will be to improve the voltage reading from the potentiostat through LabVIEW™ to better ensure that the relationship between potential and frame number is correct. The use of an IR camera poses some complications, particularly the inability to image the system through glass or water. A unique cell that includes a window through which to image a closed system, or that has the electrode directly imbedded in the wall of the container could improve confidence in the electrochemical results.

REFERENCES

(1) A. Bard, L. Faulkner. Electrochemical Methods. New York: John Wiley & Sons, 1980.

(2) B. B. Graves. “Differential Voltammetric Scanning Thermometry of Tenth Formal Formaldehyde Solution in Formal Perchloric Acid”. Anal. Chem. 1972. 44(6): 993-1002.

(3) P. Grundler, A. Kirbs, L. Dunsch. “Modern Themoelectrochemistry”. ChemPhysChem. 2009. 10: 1722-1746.

(4) V. S. Donepudi, B. E. Conway. “Electrochemical Calorimetry of the Zinc and Bromine Electrodes in Zinc-Bromine and Zinc-Air Batteries”. J. Eectrochem. Soc. 198. 131(7): 1477-1485.

(5) R. J. H. Clark, Y. Zhu. “A novel isothermal electrochemical microcalorimeter”. Thermochimica Acta. 1995. 262: 55-68.

CHAPTER 7

LOOKING FORWARD

7.1. LOOKING FORWARD: MATCHED FILTERING

Chapter 3 demonstrated how optimized gap derivative (GD) transforms perform as a particular kind of convolution function: the matched filter, a key concept in target recognition.[1-4] When the matched filter is implemented, the target signal is highlighted, while all other signals are minimized. The primary goal in applying matched filters is to maximize the signal-to-noise ratio of a known signal in the presence of white noise. Alternatively, this technique can be used to differentiate overlapping signals.

Here, the concept has been applied to differentiate the target signal of blood from the overlapping signal of the fabric. The optimal combination of gap sizes tended to resemble the target signal within the constraints of the gap derivative convolution function as described in Chapter 3: integer values at each filter channel, absolute value of filter values must sum to 2^n, symmetric function, and no more than 16 filter channels.

If the GD transform performs well under these constraints, it might be possible that a matched filter developed without them might perform even better to selectively enhance the target signal. Matched filtering has been used previously to highlight spectral features, primarily with the aim of improving peak identification and signal area estimates.[5-7] Erickson *et al.*[8] explored the

relationship between matched filtering and multivariate regression techniques such as classical least-squares (CLS), partial least-squares (PLS), and principal component analysis (PCA). In those techniques, the vectors forming the calibration model perform as digital filters, with each calibration model developing the filters under a different set of constraints. Methods such as CLS are perhaps most directly analogous in that the known target signal can be used as the basis of the regression method, while inverse methods like PLS allow estimates of the filter without *a priori* knowledge of the target signal.

In the cases above, matched filtering was not used as a preprocessing technique, but rather as a means of reducing the dimensionality of the spectrum or of modifying the appearance of the spectrum to aid direct quantitation. Implementing matched filtering as a preprocessing technique would take a different form. We can look at PLS regression as an example. The latent variables in PLS show which variables express the greatest covariance with the concentration vector.[9] In the case of blood on fabric, the variables related to amide absorption bands are weighted most heavily in the latent variables. Instead, if we were to filter the spectra with a function designed to highlight those features, we would now have a vector that shows which wavelengths have the greatest correlation with our filter. This correlation would change with concentration of blood. When the filtered spectra are then used to develop a PLS model, the latent variables formed will show which variables have a correlation with the target signal that also co-vary with the concentration. Because sources of variance that are not correlated with the target have been minimized by the

filter, they are less likely to have significant covariance with the concentration, thus they will not be heavily weighted in the PLS model.

7.2. LOOKING FORWARD: SYSTEMATIC IMPROVEMENT OF DETECTION LIMITS

The detection limits (DLs) reported in Chapter 5 for blood on fabric are the best DLs we have estimated to date. However, a variety of factors influence the ability to determine “true” DLs, and so these may not be the best possible DLs. Detection limits are limited by three primary factors: model error of the blank, sensitivity of the calibration, and the presence of noise or other interferents. These factors, then, can be considered targets for the improvement of DLs. Of primary importance in this section is the improvement of the DL by way of correcting the model error of the blank. Due to the nature of our diffuse reflection spectra, we know that our primary source of variance in the spectra can be attributed to variation in the fabric or blank spectrum. If we improve the ability of our model to ignore that extraneous source of variance in the spectra, the model will be better able to detect even small amounts of the analyte.

Previous work in the literature has generally focused on improving model performance in terms of prediction error, rather than improving the DL of the model. Improvements regarding DLs are based on improving the method of estimating the DL, rather than improving the ability to obtain better DLs. In particular, work has developed around the idea of the net analyte signal (NAS), introduced by Lorber.[10] The NAS is the portion of the target signal orthogonal to all contributions to the total signal, such as noise or the spectral contributions of

interfering species. This concept has continued to influence the discussion of analytical figures of merit, including the DL, because of its direct relationship to the sensitivity of the method to the target signal. In this way, the goal of most preprocessing and calibration methods is to maximize the NAS. Work has built on this concept to determine the NAS for both classical and inverse calibration models,[11-13] account for errors in multivariate models,[14-17] and estimate analytical figures of merit for the multivariate case.[18-24]

While this work developed better estimates of the DL, there is not to our knowledge literature related to the improvement of the DL itself. Specifically, literature does not discuss whether the DLs obtained as a figure of merit for a given calibration are truly the limits, and whether that limit is defined by the data themselves or by the ability of the calibration method to properly model that data.

Equation 5.1 shows that the DL estimated in a pseudo-univariate fashion can be improved by either increasing the sensitivity of the model to the target signal or by reducing the variability in the prediction of the blank samples. The latter amounts to making the calibration model more robust to sources of variance in the spectrum that are not related to the target signal. These two different factors do not operate in isolation from one another. Ideally, any step taken to minimize sensitivity to extraneous variability will also lead to an increase in sensitivity the target signal.

One preprocessing technique that focuses on minimizing model sensitivity to extraneous variability is orthogonal signal correction (OSC).[25] This method removes variance in the spectra that is orthogonal to the concentration vector.

Several variations of this technique exist,[26] including direct orthogonalization,[27-28] direct OSC,[29] piecewise OSC,[30] and orthogonal projections to latent structures (O-PLS).[31] A comparison of different OSC methods is presented in Svensson *et al.*[32] While these methods do reduce the number of latent variables used in the final PLS model, the effective number of latent variables remains the same. This is because a number of variables is needed to perform the signal correction. Now the total variance is partitioned between the latent variables used for OSC and the latent variables used in the PLS model, allowing users to identify sources of variance related to either the target or interferences. While this is beneficial for analyzing data, the predictive ability of the model has not been enhanced. A major limitation of these methods is that only variance orthogonal to the target concentration is removed. This means that variance in the spectra uncorrelated to the concentration but not orthogonal to it will not be removed, and that variance can still interfere with calibration performance.[33-35]

To remove the variability not correlated and not orthogonal to the concentration, the model or data might be corrected by removing known sources of variance. Investigators have approached this idea from several perspectives. One method is to explicitly incorporate a factor in the model accounting for variability due to sources such as instrument drift. This is typically done through a variation on CLS regression referred to as augmented CLS.[36-38] Another approach is to modify existing models to remove the influence of drift. Vogt *et al.* modified the principal components (PCs) of PCA by either removing a baseline polynomial or orthogonalizing the PCs to a vector representative of drift.[39]

Instead of modifying the model, the data might be orthogonalized to the principal component space of the extraneous variance, such as the difference between instruments in the case of calibration transfer,[35] or variation related to other external parameters, such as time, temperature, or water.[40-43]

In the diffuse reflection spectra of blood on fabrics presented throughout this dissertation, the primary source of variance is related to the spectrum of the fabric. This suggests that DLs could be improved by minimizing the influence of this variability on the calibration model. One way to do this draws on the techniques described above: correct the regression vector (RV) associated with the best DL models to be orthogonal to the known source of variance. Here, we can create vectors describing the primary variance not related to the target signal by looking at PCs of the mean-centered blank spectra. These vectors describe how the spectrum of the fabric varies, and the extent of overlap between the PCs and the RV gives an approximation of the extent to which that extraneous variance influences the calibration.

Given the RV *b* (*k* x 1, where *k* is the number of variables) and the PC *v* (*k* x 1), the corrected RV *b** is given by:

$$\text{Eq. 7.1} \qquad b^* = \frac{b}{\|b\|} - av$$

where *a* is a scalar. An initial approximation for *a* can be found by taking the dot product between *v* and *b*, but it might be better to optimize the value.

After *b** has been found, it must be adjusted for scale. The correction factor is the slope of the linear fit between the reference calibration values and

those predicted with b^*. After correction, this regression can now be tested with a validation data set, and the predictions can be used to determine a new DL with Eq. 5.1.

To demonstrate briefly, we take the best calibration for blood on polyester fabric (SWMIR region, gaps 2, 10, 16, 50). We can take the RVs from that calibration model based on 1 and 2 latent variables (b_1 and b_2, respectively). We perform PCA on the transformed blank spectra to determine v. Here, v will be the first PC. The dot product between b_1 and v is -0.25 and the dot product between b_2 and v is 0.0353. The much lower value associated with b_2 suggests that the second latent variable has already compensated for some of the variance expressed in v. Now, we can vary the scalar a from -1.0 to 1.0, and correct b to b^*. Each of the b^* values is adjusted for scale as described above and used to predict concentrations of the validation set. The DL estimated from the predictions made with b_1^* and b_2^* as a function of a is shown in Fig. 7.1. The black trace represents b_1^*, while the blue trace represents b_2^*. Where a equals 0, the RV is effectively unchanged. The maximum value for b_2^* falls at that point, showing that correcting the RV by removing the influence of v does not improve the calibration.

The trace for b_1^* demonstrates a different character. This time, the trace reaches a peak near -0.28, close to the dot product between b_1 and v. At this point the DL has increased by a factor of 2.5, from 320x dilute blood to 820x dilute blood. This nearly approaches the DL of 900x dilute blood estimated using

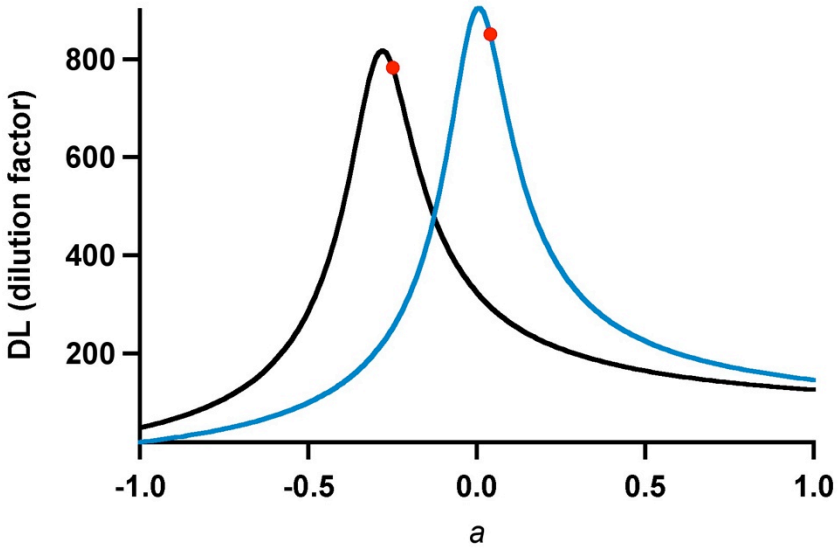

Fig. 7.1: The DL for blood on polyester fabric as a function of *a*, the amount of the first PC of the blank spectra removed from the RV. The black trace corresponds to b_1^* and the blue trace corresponds to b_2^*. The red dots mark *a* equal to the dot product between *b* and *v*. Where *a* = 0, the RV is unchanged.

a 2 latent variable model. Further work on this method might achieve even greater improvements.

This method of correcting the calibration model incorporates known sources of variance, which may create a more robust and sensitive model. Because the blank spectra provide the variance information, no additional data collection is required, making this method easy to implement. This also provides a way to investigation the limitations of the calibration model and data collection to estimate the DL, and a possible means of improving that estimation when the variability of the blank is a limiting factor.

REFERENCES

(1) D. O. North. "An Analysis of Factors Which Determine Signal Noise Discrimination in Pulsed-Carrier Systems". Proc. IEEE. 1963. 51(7): 1016-1027.

(2) G. L. Turin. "An Introduction to Matched-Filters". IEEE Trans. Inf. Theory. 1960. 6(3): 311-329.

(3) B. Sklar. "Baseband Demodulation/Detection". In: B. Sklar, editor. Digital Communications: Fundamentals and Applications. Upper Saddle River: Prentice Hall, 2001. 2nd ed. Pp. 122-136.

(4) B. V. K. V. Kumar, L. Hassebrook. "Performance Measures for Correlation Filters". Appl. Opt. 1990, 29(20): 2997-3006.

(5) R. G. Spencer. “Equivalence of the Time-Domain Matched Filter and the Spectral-Domain Matched Filter in One-dimensional NMR Spectroscopy.” Concepts in Magnetic Resonance Part A.

(6) S. E. Bialkowski. “Optimized Spectroscopic Signal Estimates Using Integration and Matched Filters”. Appl. Spectrosc. 1988, 42(5): 807-811.

(7) S. A. Dyer, D. S. Hardin. “Enhancement of Raman Spectra Obtained at Low Signal-to-Noise Ratios: Matched Filtering and Adaptive Peak Detection.” Appl. Spectrosc. 1985, 39(4): 655-662

(8) C. L. Erickson, M. J. Lysaght, J. B. Callis. “Relationship between digital Filtering and Multivariate Regression in Quantitative Analysis.” Anal. Chem. 1992, 64(24): 1155-1163.

(9) H. Martens, T. Naes. Multivariate calibration. New York: Wiley, 1989.

(10) A. Lorber. “Error Progpagation and Figures of Merit for Quantification by Solving Matrix Equations”. Anal. Chem. 1986, 58(6): 1167-1172.

(11) A. Lorber, K. Faber, B. R. Kowalski. “Net Analyte Signal Calculation in Multivariate Calibration”. Anal. Chem. 1997, 69: 1620-1626.

(12) J. Ferre, S. D. Brown, F. X. Rius. “Improved calculation of the net analyte signal in inverse multivariate calibration”. J. Chemom. 2001, 15: 537-553.

(13) N. K. M. Faber. “Efficient Computation of Net Analyte Signal Vector”. Anal. Chem. 1998, 70: 5108-5110.

(14) A. Lorber, B. R. Kowalski. “Estimation of Prediction Error for Multivariate Calibration”. J. Chemom. 1988, 2: 93-109.

(15) R. Boque, M. S. Larrechi, F. X. Rius. “Multivariate detection limits with fixed probabilities of error”. Chemom. Intell. Lab. Syst. 1999, 45: 397-408.

(16) A. C. Olivieri. “A simple approach to uncertainty propagation in preprocessed multivariate calibration”. J. Chemom. 2002, 16: 207-217.

(17) F. J. del Rio Bocio, J. Riu, R. Boque, F. X. Rius. “Limits of detection in linear regression with errors in the concentration”. J. Chemom. 2003, 17: 413-421.

(18) R. Boque, F. X. Rius. “Multivariate detection limits estimators”. Chemom. Intell. Lab. Syst. 1996, 32: 11-23.

(19) R. Boque, F. X. Rius. “Computing detection limits in multicomponent spectroscopic analysis”. TrAC, Trends Anal. Chem. 1997, 16(8): 432-436.

(20) K. Faber, A. Lorber, B. R. Kowalski. “Analytical Figures of Merit for Tensorial Calibration”. J. Chemom. 1997, 11: 419-461.

(21) K. Faber, B. R. Kowalski. “Improved estimation of the limit of detection in multivariate calibration”. Fresenius J. Anal. Chem. 1997, 357: 789-795.

(22) A. C. Olivieri, N. K. M. Faber, J. Ferre, R. Boque, J. H. Kalivas, H. Mark. “Uncertainty Estimation and Figures of Merit for Multivariate Calibration”. Pure Appl. Chem. 2006, 78(3): 633-661.

(23) F. Allegrini, A. C. Olivieri. “IUPAC-Consistent Approach to the Limit of Detection in Partial Least-Squares Calibration”. Anal. Chem. 2014. 2014, 86: 7858-7866.

(24) A. C. Olivieri. “Analytical Figures of Merit: From Univariate to Multiwary Calibration”. Chem. Rev. 2014, 114: 5358-5378.

(25) S. Wold, H. Antti, F. Lindgren, J. Ohman. “Orthogonal signal correction of near-infrared spectra”. Chemom. Intell. Lab. Syst. 1998, 44: 175-185.

(26) T. Fearn. “On orthogonal signal correction”. Chemom. Intell. Lab. Syst. 2000, 50:47-52.

(27) C. A. Andersson. “Direct orthogonalization”. Chemom. Intell. Lab. Syst. 1999, 47: 51-63.

(28) J. A. Fernandez Pierna, D. L. Massart, O. E. de Noord, Ph. Ricoux. “Direct Orthogonalization: some case studies”. Chemom. Intell. Lab. Syst. 2001, 55: 101-108.

(29) J. A. Westerhuis, S. de Jong, A. K. Smilde. “Direct orthogonal signal correction”. Chemom. Intell. Lab. Syst. 2001, 56: 13-25.

(30) R. N. Feudale, H. Tan, S. D. Brown. “Piecewise orthogonal signal correction”. Chemom. Intell. Lab. Syst. 2002, 63: 129-138.

(31) J. Trygg, S. Wold. “Orthogonal projections to latent structures (O-PLS).” J. Chemom. 2002, 16: 119-128.

(32) O. Svensson, T. Kourti, J. F. MacGregor. “An investigation of orthogonal signal correction algorithms and their characteristics”. J. Chemom. 2002, 16: 176-188.

(33) J. Gabrielsson, H. Jonsson, C. Airiau, B. Schmidt, R. Escott, J. Trygg. “OPLS methodology for analysis of pre-processing effects on spectroscopic data”. Chemom. Intell. Lab. Syst. 2006, 84: 153-158.

(34) E. Bertran, H. Iturriaga, S. Maspoch, I. Montoliu. “Effect of orthogonal signal correction on the determination of compounds with very similar near infrared spectra”. Anal. Chim. Acta. 2001, 431: 308-311.

(35) A. Andrew, T. Fearn. “Transfer by orthogonal projection: making near-infrared calibrations robust to between-instrument variation”. Chemom. Intell. Lab. Syst. 2004, 72: 51-56.

(36) D. M. Haaland, L. Han, T. M. Niemczyk. “Use of CLS to Understand PLS IR Calibration for Trace Detection of Organic Molecules in Water”. Appl. Spectrosc. 1999, 53(4): 390-395.

(37) D. M. Haaland, D. K. Melgaard. “New augmented classical least squares methods for improved quantitative spectral analyses”. Vib. Spectrosc. 2002, 29: 171-175.

(38) S. D. Brown. “Rapid Parameter estimation with incomplete chemical calibration models.” Chem. And Intel. Lab. Syst. 1991, 10: 87-105.

(39) F. Vogt, H. Steiner, K. Booksh, B. Mizaikoff. “Chemometric Correction of Drift Effects in Optical Spectra”. Appl. Spectrosc. 2004, 58(6): 683-692.

(40) J. M. Roger, F. Chauchard, V. Bellon-Maurel. “EPO-PLS external parameter orthogonalisation of PLS application to temperature-independent measurement of sugar content of intact fruits”. Chemom. Intell. Lab. Syst. 2003, 66” 191-204.

(41) K. E. Kramer, G. W. Small. “Digital Filtering and Model Updating Methods for Improving the Robustness of Near-Infrared Multivariate Calibrations”. Appl. Spectrosc. 2009, 63(2): 246-255.

(42) K. E. Kramer, G. W. Small. “Blank Augmentation Proocol for Improving the Robustness of Multivariate Calibrations”. Appl. Spectrosc. 2007, 61(5): 497-506.

(43) K. E. Kramer, G. W. Small. “Robust absorbance computations in the analysis of glucose by near-infrared spectroscopy”. Vib. Spectrosc. 2007, 43: 440-446.

APPENDIX A

REVERSIBLE GAP DERIVATIVE MATLAB CODE

Appendix A records the Matlab code needed to evaluate the reversible gap derivative and its integral as described in chapter 4.

A.1. MODIFY SPECTRUM FOR RGD

```
function [ wx, weights ] = RGDmodspec( x,gaps)
% [xmod, weights] = RGDmodspec( x,gaps ). This function pads the spectra in
% the rows of x to the length needed for integration based on the initial length of
% x and the gap combination in gaps, and computes a weighting vector that
% sinusoidally increases from 0 to 1 over the padded segment, with a  number of
% initial zeros such that RGDn(1)=0 for all derivative orders n. This weighting
% vector is then used to modify the spectra in x in preparation for differentiation
% by RGD.m.
% Written M. M. Edited by SDJ. 2015.08.06

[nsamp,npts]=size(x);
n=length(gaps);

p=2^(n-1)+1;
npoints=npts+sum(gaps)+p;
if round(npoints/2)~=npoints/2
   npoints=npoints+1;
end

%form the weighting vector
weights=ones(1,npoints);
weights(1:p)=0;%set the first p points to zero, then transition from 0 to 1
weights(p+1:npoints-npts)=(1-cos(pi*(1:npoints-npts-p)/(npoints-npts-p)))/2;
%now pad the original spectra to npoints and multiply with the weighting vector
wx=horzcat(x(:,1)*ones(1,npoints-npts),x);
wx=wx.*weights(ones(nsamp,1),:);
```

A.2. CALCULATING THE REVERSIBLE GAP DERIVATIVE

```
function [ dx, xmod ] = RGD( x,order,gaps,s )
%[ dx ] = RGD ( x, order, gaps, s). This function takes a matrix, x, and modifies
```

```
% each spectrum (row) to the proper length, 'k', to calculate a reversible gap
% derivative (RGD) as discussed in DeJong, et al. (2015, in progress). It does
% this by stepping down the difference between points at either end of the
% spectrum while maintaining the gap size, pushing the derivative toward zero at
% either end. The middle points of the derivative are determined by a
% conventional gap derivative. In the inputs: x is a row-wise matrix of spectra;
% order specifies the number of RGD iterations required; gaps contains the gap
% sizes for each derivative step (must be even); and s is the spacing in
% experimental units (e.g., nanometers or wavenumbers, etc) between points in
% the data. If you don't know that, the program assumes the separation is 1 unit.
% This function calls RGDmodspec.m to modify x to the appropriate length.
%Written by M.M.; Edited by SDJ 2015.04.30

if nargin==3
   s=1;
end
if length(gaps)~=order;
   error('Wrong Number of Gap Sizes Entered')
end
if gaps/2~=round(gaps/2);
   error('Gaps must be even')
end

gaps=sort(gaps(:),1,'ascend');%Apply gaps in ascending order

xmod=RGDmodspec(x,gaps); %modify x to the appropriate length

x=xmod;
[r,n]=size(x);
dx=zeros(r,n);

for i=1:order;
   h=gaps(i);
   a=h/2;
   % start with the first h/2 points
   dx(:,1)=(x(:,2)-x(:,1))./(h*s);
   dx(:,2:a)=(x(:,2*(2:a)-1)-repmat(x(:,1),1,a-1))./(s*h);
   % now the middle part of the derivatives
   dx(:,a+1:n-a)=(x(:,h+1:n)-x(:,1:n-h))./(s*h);
   % finally the end of the derivatives
   dx(:,n-a+1:n-1)=(repmat(x(:,n),1,a-1)-x(:,2*(n-a+1:n-1)-n))./(s*h);
   dx(:,n)=(x(:,n)-x(:,n-1))./(s*h);
   x=dx;
end
end
```

A.3. INTEGRATING THE REVERSIBLE GAP DERIVATIVE

```
function [x] = integrateRGD( dx,order,gaps,s )
% [x] = integrateRGD( dx,order,gaps,s ). This function takes a matrix dx of
% derivatives (spectra in rows) and regenerates the original matrix x of spectra
% from which they came. In the inputs, order is the number of integration
% iterations needed, gaps is the combination of gaps used to generate dx, and s
% is the spacing in units (e.g., wavenumbers or nanometers) between channels
% in the spectrum or plot. If that isn't known, it's assumed to be 1. This program
% assumes derivatives generated by RGD.m.
% Written by M.M. Edited by SDJ 2015.04.30

if nargin==3
    s=1;
end
if length(gaps)~=order;
    error('Wrong Number of Gap Sizes Entered')
end
if gaps/2~=round(gaps/2);
    error('Gaps must be even')
end
 gaps=sort(gaps(:),1,'descend');%Apply gaps in descending order
 [r,n]=size(dx);
x=zeros(r,n);

for i=1:order;
    h=gaps(i);
    a=h/2;
    %  Now we take the first two values to be 0 and h*s*dx(1)
    x(:,1)=0;
    x(:,2)=h*s*dx(:,1);
    %  we'll do the leftmost terms that depend directly on x(1);
    x(:,2*(2:a)-1)=s*h*dx(:,2:a);
    for j=a+1:n-a
        x(:,j+a)=s*h*dx(:,j)+x(:,j-a);
    end
    x(:,n)=h*s*dx(:,n)+x(:,n-1);
    % now we'll work backwards, starting with the first set
    x(:,2*(n-a:n-1)-n)=repmat(x(:,n),1,size(x(:,2*(n-a:n-1)-n),2))-s*h*dx(:,n-a:n-1);
    % now we go to the beginning, working backwards;
    for j=n-h-2:-2:4
        x(:,j)=x(:,j+h)-s*h*dx(:,j+a);
    end
    dx=x;
end
end
```

A.4. DEFINING MATRIX FORMULATION OF RGD

```
function [ matrix, factor ] = RGDmat ( x, gaps, format )
%[ matrix, factor ] = RGDmat (x, gaps, format). This function defines the matrix
% used to form a reversible gap derivative of order n (the length of gaps) and the
% factor by which the derivative must be divided. A matrix is found for each gap
% size. These are multiplied together or stored separately as defined by input
% format ('indiv' = separately, 'final' = together). The matrix will be of rank k-1 x k-
% 1, where k is the length of the modified vector/matrix x. Input x are the spectra
% from which the derivative will be taken, modified to the appropriate length by
% RGDmodspec.m. The function assumes x has samples in rows and
% wavelengths in columns.
%Written by SDJ 2015.05.06

%pad spectra to a length that ensures a reversible derivative.
wx=RGDmodspec(x,gaps);

[~,k]=size(wx);
n=length(gaps);
gaps=sort(gaps(:),1,'ascend');%Apply gaps in ascending order

for i=1:n;
   g=gaps(i); a=g/2;
   %building matrix for gap g
   M=spalloc(k,k,a+1);
   %define the first values of the RGD, stepping away from 0
   if a==1;
      ul=[-1 1];
   else
      B=diag(ones(a,1),-1);
      B=B(:,1:a);B(1)=1;
      ul=horzcat(-1*ones(a,1),spdiags(B,0:a-2,a,g-1));
   end

   M=spdiags([ones(k,1) -1*ones(k,1)],[a -a],k,k); %define the region of the typical
GD

   M(1:a,1:g)=ul; %replace upper left corner with the initial values

   M(k-a+1:k,k-g+1:k)=rot90(-ul,2); %replace lower left corner with the final
   values (a reflection of the upper left values)

   if i==1;
      matrix=M(2:k,2:k);
      factor=g;%factor to account for division by the gap size
   else
      switch format
```

```
        case 'indiv'%keep each matrix in separate cell
            if i==2;
                M2{1}=matrix;
                clear matrix
            end
            M2{i}=M(2:k,2:k);
            if i==n;
                matrix=M2;
                clear M2
            end
            factor(i)=g;
        case 'final'
            matrix=M(2:k,2:k)*matrix;%multiply steps into one step
            factor=factor*g;
    end
  end

  clear M

end

end
```

A.5. CALCULATING REVERSIBLE GAP DERIVATIVE BY THE MATRIX FORMULATION

```
function [ dx, matrix, factor, x ] = RGDmatder ( x, varargin );
%[ dx, varargout ] = RGDmatder ( x, varargin ); This function uses the matrix
% formulation to determine the reversible gap derivative of spectra x (spectra in
% rows, wavelengths in columns). For 2 inputs (matrix and factor), dx is found
% using the input matrix and factor applied to x, and only dx should be returned.
% For 1 input (gaps), dx is found after first calling RGDmat.m to define the matrix
% and RGDmodspec.m to modify the spectra to ensure the derivative is
% reversible.
%Written by SDJ 2015.05.06

if nargin==3;
  matrix=varargin{1};
  factor=varargin{2};
else
  [matrix,factor]=RGDmat(x,varargin{1},'final');
  x=RGDmodspec(x,varargin{1});
end

[r,k]=size(x);
dx=(matrix*x(:,2:k)')/factor;%find the derivative
```

```
dx=horzcat(zeros(r,1),dx');%add the first point = 0 to each spectrum
```

A.6. INTEGRATING THE REVERSIBLE GAP DERIVATIVE BY THE MATRIX FORMULATION

```
function [x] = RGDmatintegrate(dx,matrix,factor);
%[x] = RGDmatintegrate ( dx, matrix, factor ). This function finds the integrated
% vector from the reversible gap derivative, matrix, and factor given from
% RGDmatder. The output x is the array of zero-order spectra (assuming rows of
% dx are samples, columns are wavelengths).
% Written by SDJ 2015.05.06

[r,k]=size(dx);

x=matrix\dx(:,2:k)';%inverse(matrix)*derivative
%appending those zeros to the beginning of the spectra and adjusting for the
% division by the gap that occurs in the derivative.
x=factor*horzcat(zeros(r,1),x');
```

APPENDIX B

ELECTROCHEMISTRY / THERMOGRAPHY MATLAB CODE

Appendix B reports the code used to process the voltage data, infrared images, and potentiostat data collected for each measurement. This code corrects the voltage data and determines whether the camera frames relate to forward or reverse potential sweeps.

B.1. READ IN POTENTIOSTAT DATA

```
function [a]=empower
% function [a] = empower. Purpose: Imports text files from PowerSuite and plots
% current v. voltage.
% Last edited: 2012.06.27 SDJ

[filename,pathname] = uigetfile('*.*','Choose files','Multiselect','off');
fullname=strcat(pathname,filename);
a=dlmread(fullname,'\t',1,0);
% now plot the results
figure; plot(a(:,1)*10^3,a(:,2)*10^6);
xlabel 'E vs Ag/AgCl (mV)'
ylabel 'Current (uC)'
title(mat2str(filename));
end
```

B.2. SEPARATE CYCLES OF THE POTENTIATIOSTAT DATA.

```
function [x2,xm,pot]=cvsep(x);
% function [x2,xm,pot]=cvsep(x); Separates the cycles of the cyclic
% voltammogram data read in by empower.m
% Last edited: 2014.11.24 SDJ

ind=find(x(:,3)==0);
ind(length(ind)+1)=length(x)+1;

pot=x(ind(1):ind(2),1);

for i=1:length(ind)-1;
```

```
    x2(:,i)=x(ind(i):ind(i+1)-1,2);
end

xm=mean(x2,2);
```

B.3. READ IN VOLTAGE DATA FROM LABVIEW FILE

```
function [data]=voltage
% function [data]=voltage. Reads in the voltage file collected in LabVIEW.
% Last edited: 2013.09.19 SDJ

%Select voltage file
[filename,pathname] = uigetfile('*.bin');
fullname = strcat(pathname,filename);
fid=fopen(fullname,'r','b');

fseek(fid,200,'bof'); % There are 200 bits of "junk" data that we skip.

data(:,:)=(fread(fid,[2400,1],'double'))';

fclose('all');
```

B.4. READ IN IR CAMERA IMAGES

```
function [data_final,introdat]=binarymovie
% function [data_final,introdat]=binarymovie. This function reads binary data into
% matlab.
% Copied from HB's function / Updated by OBrien (1/20/13)

[filename,pathname] = uigetfile('*.bin');
fullname = strcat(pathname,filename);
fid=fopen(fullname,'r','b');

introdat=(fread(fid,[200,1],'uint16'));

fseek(fid,0,'eof');
n=(ftell(fid)-200)/(2*320*240);%n= the total number of frames.

% This code builds the 3D data array of images.
fseek(fid,200,'bof'); % There are 200 bits of "junk" data that we skip.
data=zeros(320, 240, n,'uint16'); % Preallocate for speed
for i=1:n
data(:,:,i)=(fread(fid,[240,320],'uint16'))';
end
fclose('all');
data_final = flipdim(double(data),2);%conversion to Double type of data
```

B.5. IDENTIFY FORWARD AND REVERSE CYCLES OF THE CAMERA FRAMES

```
function [f,r]=cycleidv2(x,cycles,cyclel);
% function [f,r]=cycleidv2(x,cycles,cyclel). Marks the frames associated with
% forward and reverse cycles of a voltammogram where x is the output from
% voltage.m truncated to only include full cycles, cycles is the number of full
% scans, and cyclel is the approximate spacing between minima.
% Last edited: 2014.11.24 SDJ

f(1,1)=1;
[~,f(1,2)]=max(x(1:cyclel));
r(1,1)=f(1,2)+1;
[~,r(1,2)]=min(x(r(1,1):r(1,1)+cyclel));
r(1,2)=f(1,2)+r(1,2);

for i=2:cycles;
    f(i,1)=r(i-1,2)+1;
    [~,f(i,2)]=max(x(f(i,1):f(i,1)+cyclel));
    f(i,2)=r(i-1,2)+f(i,2);
    r(i,1)=f(i,2)+1;
    if r(i,1)+cyclel>length(x);
        cyclel=length(x)-r(i,1);
    end
    [~,r(i,2)]=min(x(r(i,1):r(i,1)+cyclel));
    r(i,2)=r(i,2)+f(i,2);
end
```

B.6. ADJUST CAMERA VOLTAGES TO POTENTIOSTAT VALUES

```
function y2=voltfitv2(x,f,r);
% function y2=voltfitv2(x,f,r). This will adjust the potential values read in by
% voltage to cover the same range as the potential values recorded by the
% potentiostat. f and r are forward and reverse outputs of cycleid.m and x is the
% associated potential vector (from the camera), truncated to only include full
% scans.
% Last edited: 2014.11.24 SDJ

for i=1:size(f,1);
    b=polyfit((f(i,1):f(i,2))',x(f(i,1):f(i,2)),1);
    y2(f(i,1):f(i,2))=polyval(b,f(i,1):f(i,2));
    b=polyfit((r(i,1):r(i,2))',x(r(i,1):r(i,2)),1);
    y2(r(i,1):r(i,2))=polyval(b,r(i,1):r(i,2));
end
```

B.7. ADJUST THE OUTPUT OF VOLTFITV2.M TO MATCH THE POTENTIAL VALUES FROM THE POTENTIOSTAT

```
function x2=camvoltshiftv2(nv,f,cyclepot);
% function x2=camvoltshift2(nv,f,cyclepot). nv is output from voltfit.m. f is an
% output from cycleid, marking the frames associated with each half cycle.
% cyclepot is the output of cvsep associated with the "true potential". x2 is the
% "actual" voltage, or at least closer.
% Last edited: 2013.09.23 SDJ

%Define what the limits should be
ulim=max(cyclepot);
llim=min(cyclepot);
span=ulim-llim;
m=size(f,1);
%Determine frame length of each half cyle
for i=1:m;
   f2(i)=f(i,2)-f(i,1);
end
for i=1:m-1;
   r(i)=f(i+1,1)-f(i,2);
end;
r(m)=length(nv)-f(m,2);
%Create adjusted voltage vector
for i=1:m;
   x2(f(i,1):f(i,2))=[llim:span/f2(i):ulim];
end
for i=1:m-1;
   x2(f(i,2):f(i+1))=[ulim:-span/r(i):llim];
end;
x2(f(m,2):length(nv))=[ulim:-span/r(m):llim];
end
```

B.8. DETERMINE MEAN FORWARD AND REVERSE FOR CAMERA

```
function [f,r]=frmeanv2(x,forward,reverse);
% function [f,r]=frmeanv2(x,forward,reverse). Creates the mean for all forward
% and all reverse portions of scans using output from cycleid.m. x is the image
% data of interest that will be plotted agains the output of camvoltshift.m.
% Last edited: 2013.09.23 SDJ

m=size(forward,1);

sub1=min(forward(:,2)-forward(:,1));
sub2=min(reverse(:,2)-reverse(:,1));

for i=1:m;
```

```
    t=x(forward(i,1):forward(i,2));
    f(i,:)=t(1:sub1);
    t=x(reverse(i,1):reverse(i,2));
    r(i,:)=t(1:sub2);
end

f=mean(f,1);
r=mean(r,1);

end
```